Water mass exchange, pathways and the mesoscale eddy field in the Lofoten Basin of the Norwegian Sea

Johannes Sandanger Dugstad

Thesis for the degree of Philosophiae Doctor (PhD)
University of Bergen, Norway
2020

UNIVERSITY OF BERGEN

Water mass exchange, pathways and the mesoscale eddy field in the Lofoten Basin of the Norwegian Sea

Johannes Sandanger Dugstad

Thesis for the degree of Philosophiae Doctor (PhD)
at the University of Bergen

Date of defence: 05.11.2020

Year: 2020

Title: Water mass exchange, pathways and the mesoscale eddy field in the Lofoten Basin of the Norwegian Sea

Name: Johannes Sandanger Dugstad

Print: Skipnes Kommunikasjon / University of Bergen

Scientific environment

This study is carried out at the Geophysical Institute, University of Bergen. I have also been affiliated with the Bjerknes Centre for Climate Research (BCCR). The work is connected to the project *Watermass transformation processes and vortex dynamics in the Lofoten Basin of the Norwegian Sea* (ProVoLo, 250784) funded by the Norwegian Research Council of Norway. The PhD is an in-kind contribution to ProVoLo from UiB. I have been enrolled in the Research school on changing climates in the coupled earth system (CHESS). I had research visits in Oslo, Stockholm and Kiel, hosted by my external supervisors, allowing me to interact with the local environments there.

Acknowledgements

I would like to thank all my supervisors (Ilker, Pål Erik and Inga). You are all very inspiring and hard working scientists, and you have all been very helpful and kind during the different stages of my PhD. Thank you Ilker for having your door always open for questions. You have always provided me with good feedback and with many good ideas. I really appreciate your efficiency and your ability to give high-quality feedback on results/drafts only a day after I provide them to you. This PhD would not be possible without your help. Thanks Pål Erik for all discussions and feedbacks, especially for the last paper. My shorter visits to you in Oslo have been efficient and productive. Even though Covid-19 avoided me to visit you this last semester, we managed to keep the good discussions and progress over skype. Inga, thank you for letting me visit you both in Kiel and in Stockholm, and for introducing me to many relevant colleagues at the LAPCOD meeting. My two stays at your place have been great and you gave me a lot of hands-on help while I was there. I truly want to thank you for your enthusiasm around my work. I mean, during my last stay in Stockholm, we basically wrote a whole paper.

Thanks to all the good colleagues here at GFI. I think we are a great PhD team having lots in common, also outside work. Thanks to the football and volleyball-people for all funny and intense training sessions. Our 5th place (out of 27) in the Hordaland volleyball tournament in 2018 is certainly a very good memory. I have had many office mates during these 4 years. I want to thank Kjersti, Anthony, Nadine, Kristin, Kjersti and Vår for good company.

My family and friends also deserves a big thank you. I want to thank all my friends here in Bergen for 4 good years. Lastly, thanks to my family that have always been there for me in good and hard times. Thank you for all your support during these 4 years!

Johannes Sandanger Dugstad
Bergen, 27.08.2020

Abstract

The Lofoten Basin situated in the Norwegian Sea, plays a central role in redistributing and modifying the warm Atlantic Water carried poleward with the Norwegian Atlantic Current. Increased residence time of the warm Atlantic Water in this region, leads to a large cooling and the largest surface heat losses in the Nordic Seas.

This thesis studies the exchange of Atlantic Water with the Lofoten Basin using observations and numerical models, and Lagrangian and Eulerian approaches. A key focus is the study of the mass and heat exchange with the basin outlined by the 3000-m isobath. Surface drifters are analyzed to study the surface circulation in the Nordic Seas and to estimate the water mass exchange with the Lofoten Basin. Fields from Eulerian models and trajectories from Lagrangian simulations at multiple levels are further used to study the processes leading to the exchange, by delineating the mean and eddy component of the flows. Analyses aimed to quantify the mesoscale eddy properties, their interaction with the ambient, heat and vorticity budgets, and to assess the importance of eddies relative to the ambient flow and other submesoscale processes in the mass and heat exchange with the Lofoten Basin. The geographical origins of the water masses having largest interaction with the basin are identified, and these sites are studied in detail to investigate the processes behind the exchange. The thesis also investigates the fate of water masses in the basin to study how their properties evolve with time, and compare this with other regions.

The first main finding, obtained from surface drifter observations, indicates an increased exchange of Atlantic Water across the southern sector of the Lofoten Basin. The drifters show a meandering motion between the eastern and western branches of the Norwegian Atlantic Current towards the basin, and Eulerian simulations suggest that the inflow is primarily related to a mean component of the flow. The warm waters experience long residence times and large temperature losses in the basin. In contrast with earlier literature, there is less evidence of near-surface exchange with the waters carried by the slope current along the continental slope off Norway. However, the net heat transport into the basin is dominated by eddy fluxes. Furthermore, the divergence of eddy heat fluxes obtained from Eulerian calculations on the continental slope is large, and particularly enhanced at depths of about 400 m. It is therefore suggested that the flow from the south dominates the near-surface exchange of Atlantic Water with the basin, but eddy fluxes from the slope region are important at deeper levels.

Lagrangian simulations of particles deployed at several depths reveal variations in the vertical structure of the inflows to the Lofoten Basin. Of the water parcels that are cooled most (more than 1^oC) while in the basin, those at the surface mainly enter from the south, and those at deeper levels (about 500 m) come from the slope. The inflows also have a seasonal variability. In winter, cooling and vertical mixing result in

weak stratification and distribute the particles vertically, while strong stratification in summer limits their vertical excursions from their deployment depths. During winter, water masses close to the surface therefore tend to sink and give weaker inflows (less particles) close to the surface and stronger inflows (more particles) at deeper levels (100-300 m).

The eddy activity in the basin and on the continental slope is quantified. Eddy signals extracted from Lagrangian trajectories, using multivariate wavelet ridge analysis, show that water masses in coherent vortices experience larger changes in their water properties (such as temperature and density) than water masses in the ambient flow, with enhanced warming in cyclones and enhanced cooling in anticyclones. There is also evidence of upwelling in the cyclones and downwelling in the anticyclones. The change of water properties and net vertical displacement is most pronounced in the Lofoten Basin. The anticyclones have a longer lifetime, more circular shape and larger radius than the cyclones. However, the eddies only cover a small portion of the Nordic Seas (about 6%) and the ambient flow and filaments around eddies therefore play an important role in balancing the Lofoten Basin heat and vorticity budgets. Ridge analysis confirms the role of eddy activity at deeper levels on the slope, and further reveals that the anticyclonic eddies generated on the slope bring warm water into the basin. Energetics and energy-conversion rates calculated from mooring observations from the upper slope, supported by volume-averaged calculations from an Eulerian model, are consistent with the Lagrangian and Eulerian analyses. Estimated baroclinic conversion rates imply that potential energy is extracted from the mean flow to eddies. The role of filaments in the upper layers, the link between the generation of eddies on the slope and their exchange with the LB at deeper layers, and contribution of these eddies and filaments to the Lofoten Basin heat and vorticity budgets merit further studies.

Outline

This thesis consists of an introductory part (Chapter 1 to 4) and four scientific papers. Chapter 1 gives an introduction to the circulation patterns associated with the Lofoten Basin of the Norwegian Sea and the regions around. Objectives, data and methods, as well as a detailed description of numerical models used are provided in Chapter 2. A brief summary of the papers is given in Chapter 3, and conclusions, outlook and future perspectives are given in Chapter 4. The manuscripts included in this thesis (Chapter 5) are:

1. Dugstad, J.S, Fer, I., LaCasce, J., de La Lama, M.S., Trodahl, M. (2019) *Lateral Heat Transport in the Lofoten Basin: Near-Surface Pathways and Subsurface Exchange*, **Journal of Geophysical Research: Oceans**, 124

2. Dugstad, J.S., Koszalka, I.M., Isachsen, P.E., Dagestad, K.F., Fer, I. (2019) *Vertical Structure and Seasonal Variability of the Inflow to the Lofoten Basin Inferred From High-Resolution Lagrangian Simulations*, **Journal of Geophysical Research: Oceans**, 124, 9384-9403

3. Dugstad, J.S., Isachsen, P.E., Fer, I. (2020) *The mesoscale eddy field in the Lofoten Basin from high-resolution Lagrangian simulations*, **Prepared for submission to Ocean Science**

4. Fer, I., Bosse, A., Dugstad, J.S. (2020) *Norwegian Atlantic Slope Current along the Lofoten Escarpment*, **Ocean Science**, 16, 685-701

Contents

Chapter 1

Introduction

The Nordic Seas (a joint name for the Greenland, Iceland and Norwegian Seas) in the northern North-Atlantic Ocean, situated north of Iceland and between the coast of Norway in the east and the coast of Greenland in the west, is a region where Atlantic Water (AW) flowing northwards with the North Atlantic Current accumulates and exhibits large transformation. The transformation of AW is an important component of the Atlantic Meridional Overturning Circulation which regulates the global climate system and its variability (*Broecker*, 1991). Warm and salty AW entering the Nordic Seas from the south, experiences large amount of cooling, which impacts the characteristics of the water masses before they enter the Arctic Ocean. As the AW enters the Nordic Seas, warm and nutrient-rich waters which are important for the regional climate (*Rhines et al.*, 2008; *Seager et al.*, 2002) as well as for supporting the food chain there (*Sundby*, 2000) spread into its various basins.

The circulation in the Nordic Seas is mainly cyclonic (*Mauritzen*, 1996; *Voet et al.*, 2010) with a northward flow of AW in the east (*Isachsen*, 2015; *Koszalka et al.*, 2011; *Orvik and Niiler*, 2002; *Raj et al.*, 2016). A large part of this water either enters the Barents Sea or flows through Fram Strait west of Svalbard into the Arctic. However, a part of the AW also recirculates and connects with the southward-flowing East Greenland Current carrying colder and fresher water southwards along the east coast of Greenland (*Eldevik et al.*, 2009; *Mauritzen*, 1996). This results in large temperature gradients between the warm eastern and the cold western side of the Nordic Seas.

The bathymetry of the Nordic Seas (Figure 1.1 a) mainly consists of basins that are separated from each other by ridges. The Lofoten Basin (LB), situated on the eastern side, is separated from the Norwegian Basin in the south/southwest by the Helgeland Ridge and the Vøring Plateau, from the Iceland Sea in the west by the Jan Mayen Ridge, and the Greenland Basin in the northwest by the Mohn Ridge. The basins have depths of 3000-4000 m while the ridges reach shallower depths of about 1000 m. The flow in the Nordic Seas is shown to strongly follow the topography (*Nøst and Isachsen*, 2003), and little exchange of water occurs between the basins. A warm eastern and a cold western Nordic Seas is therefore maintained through the whole year (Figure 1.1 b), with the LB being on average the warmest basin (*Koszalka et al.*, 2013; *Richards and Straneo*, 2015; *Segtnan et al.*, 2011).

1.1 The Norwegian Atlantic Current

The AW is carried northwards with the Norwegian Atlantic Current (NwAC) (Figure 1.1). As the NwAC reaches the Norwegian Seas, it splits into two branches (*Orvik and Niiler*, 2002; *Poulain et al.*, 1996). These are the Norwegian Atlantic Slope Current (Slope Current hereinafter) which flows along the continental slope of Norway, and the Norwegian Atlantic Front Current (Front Current hereinafter) flowing on the western side of the LB and along the Mohn Ridge close to the Polar Front (the transition zone between the AW in the east and colder Arctic Water in the west of the Nordic Seas) (*Orvik and Niiler*, 2002). The Slope Current flows along the steep topography off the Norwegian coast while the Front Current is an approximately 400 m deep, baroclinic, topographically-steered jet (*Bosse and Fer*, 2019a; *Orvik et al.*, 2001).

While not much is known about the Front Current, a lot of attention has been given to the Slope Current. Steep topography along its path can cause instabilities related to both horizontal or vertical shear in the flow (*Isachsen*, 2015; *Köhl*, 2007; *Volkov et al.*, 2015), that can lead to large variability in the velocity fields, enhanced eddy kinetic energy (EKE) and stirring in the region. The instabilities are especially large close to the Lofoten Escarpment where the continental slope is at its steepest and where the currents are strongest with speeds of about $1\mathrm{ms}^{-1}$ (*Andersson et al.*, 2011). *Isachsen* (2015) showed that in these areas the baroclinic growth rates are enhanced and the velocity variability is large, suggesting high lateral diffusion rates. The slope is therefore suggested to be an important region for generation of eddies (e.g., coherent vortices with mesoscale length and time scales) that can travel laterally away from the slope into the ocean interior (*Isachsen*, 2015; *Köhl*, 2007; *Raj et al.*, 2016, 2015; *Volkov et al.*, 2013, 2015).

The prevailing notion is that the Slope Current and the Front Current form two boundaries on the eastern and western side of the LB, before they reconnect towards Fram Strait. However, some studies also indicate a connection between the two branches further south at the LB latitudes. For instance, some of the water masses in the Front Current can be topographically steered over the northern part of the Vøring Plateau and connect with the Slope Current just south of the LB (*Orvik and Niiler*, 2002; *Raj et al.*, 2016). Furthermore, the wind pattern, which is on average cyclonic in the Nordic Seas, can have an effect on the surface flow. A cyclonic wind pattern would lead to Ekman transport towards the coast for the Slope Current, and the variable wind field can lead to a more diffusive flow at the surface that does not strictly follow the idealized branches of the Slope Current and the Front Current (*Poulain et al.*, 1996). This is different from deeper levels where the flow is approximately guided by topography (*Isachsen et al.*, 2003).

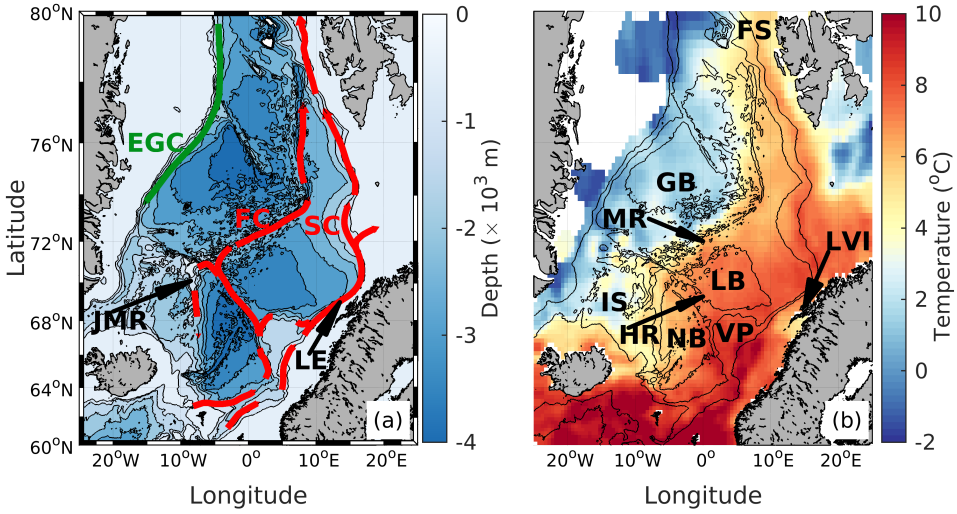

Figure 1.1: (a) Bathymetry map (from ETOPO2) of the Nordic Seas showing the northward-flowing Slope Current and Front Current, and the southward flowing East Greenland Current. Black contours are given with 500 m intervals; (b) Averaged temperature field at 15 m depth between 2000-2019 mainly obtained from the Unified Database for Arctic and Subarctic Hydrography (UDASH, Huang et al. (2020)). Abbreviations which are distributed over both panels for clarity are: SC=Slope Current, FC=Front Current, EGC=East Greenland Current, JMR=Jan Mayen Ridge, LE=Lofoten Escarpment, NB=Norwegian Basin, LB=Lofoten Basin, GB=Greenland Basin, IS=Iceland Sea, VP=Vøring Plateau, HR=Helgeland Ridge, MR=Mohn Ridge, LVI=Lofoten-Vesterålen Islands, FS=Fram Strait.

1.2 The eddy field in the Lofoten Basin

The LB is characterized by an active eddy field (*Chafik et al.*, 2015; *Fer et al.*, 2018; *Isachsen*, 2015; *Köhl*, 2007; *Raj et al.*, 2016, 2015; *Volkov et al.*, 2015), which for instance is seen in EKE maps of the region (Figure 1.2). Large EKE values towards and along the Slope Current by the Lofoten Escarpment off the Lofoten-Vesterålen Islands (LVI), are likely associated with eddy generation on the slope (*Isachsen*, 2015; *Köhl*, 2007; *Raj et al.*, 2016). These eddies can be both cyclonic and anticyclonic, but it has been shown that the anticyclones are more frequent and stronger than the cyclones (*Volkov et al.*, 2015). The anticyclones also have a longer lifetime than the cyclones (*Raj et al.*, 2016), which could be explained by their lateral motion towards the deeper ocean interior. Due to bottom depression off the slope, the anticyclones may be stabilized while the cyclones may be destabilized (*Benilov*, 2005). The anticyclonic eddy shedding from the slope is believed to be important for the LB heat budget (*Isachsen et al.*, 2012; *Köhl*, 2007; *Raj et al.*, 2016).

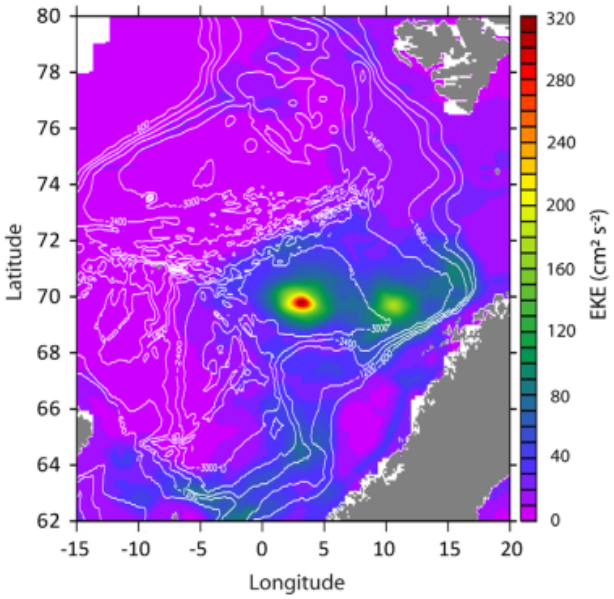

Figure 1.2: Eddy-kinetic energy (EKE) at the surface obtained from satellite altimetry data. The figure is a reprint of Figure 4b in Raj et al. (2015).

The EKE maps inferred from surface geostrophic current anomalies from satellite altimetry, reveal a local maximum in the interior of the LB (Figure 1.2). This is associated with the semi-permanent anticyclonic Lofoten Basin Eddy (LBE, also referred as the Lofoten Vortex). This eddy is situated near $[3^oE, 70^oN]$ (*Ivanov and Korablev*, 1995) and has a radius between 18 and 22 km (the radius of maximum orbital velocity) and an anticyclonic vorticity of about -$(0.7-1) \times f$ (*Fer et al.*, 2018; *Søiland and Rossby*, 2013) where f is the Coriolis frequency. The permanent characteristic of the LBE is attributed to the merging with other anticyclonic eddies, typically from the slope, and merging events have been seen both in model studies (*Köhl*, 2007) and in satellite altimetry (*Raj et al.*, 2016). The merging events feed energy to the LBE to make it a permanent feature. Another secondary EKE maximum is found near $[9^oE, 68.5^oN]$, close to the southeast corner of the 3000 m isobath defining the LB. This is not a permanent eddy, but eddies often occur in this region, likely caused by the topographic contours that could trap eddies there.

1.3 Surface heat loss and distribution of the Atlantic Water in the Lofoten Basin

Due to its warm temperatures, the LB forms a major heat reservoir (*Bosse et al.*, 2018; *Nilsen and Falck*, 2006). *Broomé et al.* (2020) showed from satellite observations that there has been a general positive trend and decadal changes in the LB heat content during the last three decades (1993-2017). In their study of the AW in the Nordic Seas, the main reason for the variation and increase of heat content was suggested to

be dominated by the variability in remote, upstream regions, advected with the Atlantic source waters entering the Nordic Seas over the Greenland-Scotland Ridge. The trends were particularly amplified in the LB. The heat content in the LB is therefore the largest in the Nordic Seas (Figure 1.3).

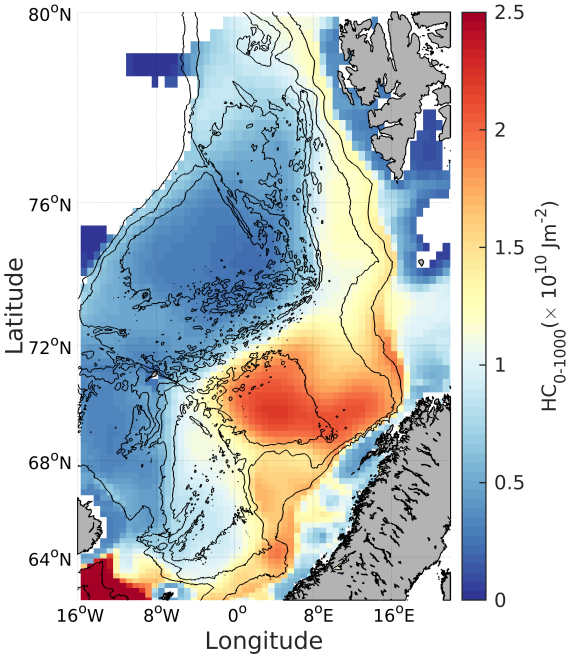

Figure 1.3: Heat content of the upper 1000 m in the Nordic Seas (or to bottom in shallower areas). Black contours show the 1000, 2000 and 3000 m isobaths. The Figure is a modified version of Figure 4 a in Bosse et al. (2018), obtained from a hydrographical Atlas of the Nordic Seas (Bosse et al., 2018).

Because of strong atmospheric cooling in the Nordic Seas, the heat reservoir in the LB leads to net surface heat losses year around, and especially pronounced in winter. In fact, even though the LB covers about 1/3 of the Nordic Seas, it accounts for about 3/5 of the heat loss in the region (*Richards and Straneo*, 2015). The annual average heat loss has earlier been estimated to about 60 Wm^{-2} (*Isachsen et al.*, 2007), a quantity which is also large compared to most regions in other latitudes (*Huang*, 2015). The large heat loss is, in addition to being important for the regional climate in Norway, important for the modification of AW as it flows northwards. Due to a cyclonic circulation inside the LB (*Volkov et al.*, 2013), water parcels experience long residence times in the region, leading to stronger cooling and densification, and subduction of the water masses (*Bosse et al.*, 2018; *Mauritzen*, 1996; *Rossby et al.*, 2009a). The strong atmospheric cooling, especially in winter, leads to weak stratification in the upper part of the water column, depression of isopycnals, deep mixed layers, and pooling of the AW in the basin. This creates an Atlantic layer that can reach depths of 500 m on average in the basin (*Mauritzen*, 1996), (Figure 1.4). The deep-reaching winter convection is especially pronounced in the western part of the basin close to the LBE (*Bosse et al.*, 2018), implying a substantial modification of the AW there. In general, the cooling is

suggested to be enhanced in the eddies. Studies of the hydrography in the Nordic Seas indicate vertical mixing in the eddies, for instance illustrated by deep isopycnals in the anticyclones that imply warm surface water which is mixed down to 600 m (*Bosse et al.*, 2018; *Rossby et al.*, 2009b). In the LBE, this warm water has been shown to mix down to about 1200 m (*Bosse et al.*, 2018).

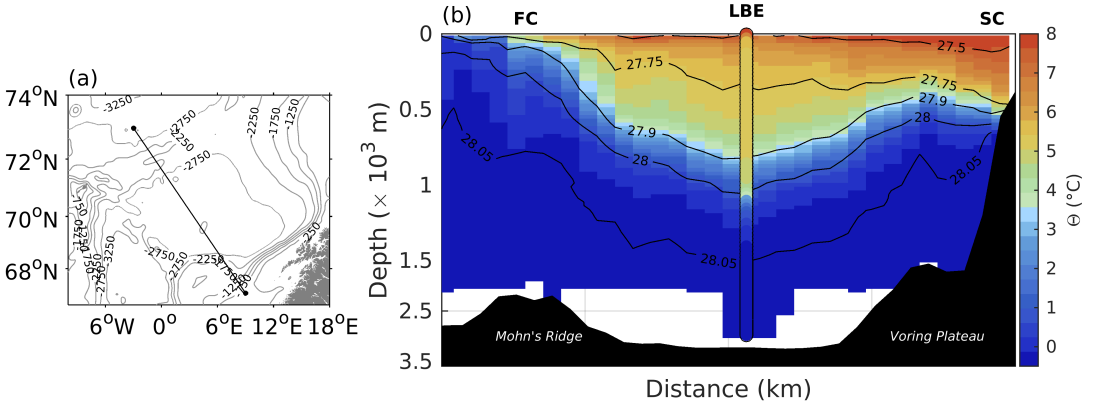

Figure 1.4: (a) Bathymetry map of the LB including a section given by the black line. Binned temperature along this section is shown in (b) with potential density anomaly contours given in black. The column separately shows the temperature signal in the LBE. Abbreviations are: FC=Front Current, SC=Slope Current, LBE=Lofoten Basin Eddy. The Figure is a modified version of Figure 2 a,b in Bosse et al. (2018), obtained from a hydrographical Atlas of the Nordic Seas (Bosse et al., 2018).

1.4 The exchange of Atlantic Water with the Lofoten Basin

As the warm water and large surface heat losses in the LB are maintained throughout a year as well as over multiyear time scales, there must be an exchange of Atlantic Water with the Lofoten Basin (AW-LB exchange) such that there is an inflow-outflow balance to the basin where the inflow is warmer than the outflow. The AW-LB exchange has been studied extensively over the last three decades to understand why the LB plays such an important role for the surface heat loss and hence the modification of the northward-flowing water masses in the Nordic Seas.

A large part of the AW-LB exchange has been attributed to the mesoscale eddy field (Section 1.2). *Isachsen et al.* (2012) estimated a divergence of eddy heat fluxes from the slope implying a divergence of warm water from the slope, possibly to the basin interior, that is caused by large variability in the flow that can be related to eddies. Furthermore, *Volkov et al.* (2013) estimated a cyclonic drift of eddies away from the slope towards the basin. These eddies can be important for the heat budget of the LB (*Isachsen et al.*, 2012; *Köhl*, 2007; *Raj et al.*, 2016; *Volkov et al.*, 2015), but whether this is the main mechanism for feeding the LB with heat is not known. In fact, Lagrangian studies suggest that surface drifters often tend to enter the LB from the south between the Slope Current and the Front Current (*Koszalka et al.*, 2013), implying an exchange that is not related to the eddy activity on the slope. The associated water masses are likely warm, and due to the surface cooling, they might release heat before they are advected

out of the basin in the northeast. In addition, little is known about the exchange between the Front Current and the basin. Although the path of the Front Current is colder (it flows close to the Polar Front), the Front Current can bring warm AW northwards and affect the heat budget of the basin.

Therefore, there are several opinions in the community about the processes of AW-LB exchange. Whether the inflows and outflows have a seasonal dependence or a vertical variability is also not known. Surface drifters are affected by the Ekman transport towards the Norwegian coast and it is therefore argued that they are rarely captured in eddies generated off the Lofoten Escarpment, but instead follow the path of the Slope Current (*Poulain et al.*, 1996; *Rossby et al.*, 2009a). This implies little AW-LB exchange at surface. But at deeper levels, acoustically-tracked subsurface floats were observed to enter the LB from the slope (*Rossby et al.*, 2009a), perhaps suggesting a variable vertical structure in the AW-LB exchange.

Chapter 2

This study

2.1 Objectives and approach

An understanding of key processes for the AW-LB exchange will help to understand the important role of the LB in redistributing and transforming warm AW, leading to increased surface heat losses. The main objective of this study is therefore to understand the underlying mechanisms of the AW-LB exchange and how the exchanges lead to transfer of heat between the poleward-flowing branches of the NwAC and the basin. An important part of the study is to investigate how this impacts the LB heat budget. Guiding research questions can be listed as:
What is the role of the LB in heat loss and modification of water masses in the Nordic Seas?
What are the main mechanisms driving the AW-LB exchange and how are these related to the net heat transport into the basin?
How does the AW-LB exchange vary during different seasons and with depth?
What is the role of eddies compared to the mean flow and submesoscale processes in transporting heat and modifying the AW?

We first study the near-surface AW-LB exchange (Paper I). Then we move deeper in the water column to compare surface and subsurface exchanges, and to compare 2D and 3D effects (Paper II). A more specialized study to quantify the eddy properties and the contribution of eddies to the AW-LB exchange compared to the other parts of the flow (ambient flow hereinafter) is performed in Paper III. The studies are based on observational surface drifter data (Paper I-II), numerical ocean models (Paper I-IV), and numerical Lagrangian simulations (Paper I, II and III). The thesis discusses the ocean circulation in the eastern Nordic Seas from a Lagrangian perspective both at the surface (Paper I) and at deeper levels (Paper II, III), with a main focus on the AW-LB exchange (Paper I, II, III). Eulerian ocean models supplement the Lagrangian studies when investigating the heat budgets of the LB (Paper I and II) and the relative contribution of eddy fluxes and the mean flow to the net heat transport into the LB (Paper I). In addition, the activity on the slope, i.e the convergence/divergence of warm AW to/from the Slope Current due to eddy fluxes or the mean flow (Paper I), as well as the energy conversion rates between the mean flow and eddies on the slope (Paper IV), are computed. The energy conversion rates and the heat flux convergences are important to understand where eddy shedding occurs along the slope and whether they advect anomalously warm or cold waters.

We perform 2D (only horizontal movement) and 3D (including vertical motion) Lagrangian simulations to address the seasonal variability and the vertical structure of the AW-LB exchange (Paper II). By performing the two types of simulations, we are able to compare the results from 2D and 3D particles and further evaluate the liability of observations from surface drifters, which are forced to move horizontally. Lastly, to delineate the importance of eddies and ambient flow for the AW-LB exchange, a wavelet-based ridge analysis is performed on the Lagrangian model trajectories to identify coherent vortices and hence associate the corresponding particles with eddies (Paper III). The remaining part of the trajectories are assumed to represent a combination of the mean flow, other non-coherent variability and narrow submesoscale filaments. The analysis is extended further to quantify and describe the cyclonic and anticyclonic eddies, quantify the evolution of AW properties in eddies and the ambient flow, and to quantify the contribution of eddies and the ambient flow for the heat and vorticity budgets in the basin.

2.2 Data and methods

2.2.1 Observational data

Surface drifters

The observational data used in this thesis are the surface drifter data in the Nordic Seas (Paper I and II), obtained from the Global Array Drifter Program (*Lumpkin and Pazos*, 2007; *Lumpkin et al.*, 2013) via https://www.aoml.noaa.gov/phod/gdp/. The surface drifters are GPS-tracked and drogued at 15 m depth, with a near surface temperature sensor at approximately 0.3 m with 0.1 K resolution (Figure 2.1). Each drifter also has a tether strain sensor that monitors the prescence of the drogue. As the real-time drifter data can be unevenly sampled (sampling frequencies can change from 1 hr to in some occasions 1 day), the drifter positions are quality-controlled and interpolated via a kriging method to 6 hour intervals by the Atlantic Oceanographic and Meteorological Laboratory (AOML) and the National Oceanographic and Atmospheric Administration (NOAA) Drifter Data Assembly Center (*Lumpkin and Pazos*, 2007), transmitting data of longitude/latitude, zonal/meridional velocities and temperature.

A large number of the surface drifters in the Nordic Seas (about 120) was deployed as a part of the POLEWARD experiment (*Koszalka et al.*, 2009) during the International Polar Year (2007-2009), and a smaller subset (10 drifters) was deployed as part of the ProVoLo project. Other drifters found in the Nordic Seas are results of smaller experiments or that they entered the Nordic Seas after being deployed elsewhere. In total, about 570 surface drifters were either deployed in or entered the Nordic Seas between 1991 and 2019 spanning about 30 years and giving approximately 140,000 days of data (Paper I). Note, however, that data selection criteria resulted in a smaller number of drifters that were actually studied (149 in Paper I, 370 in Paper II).

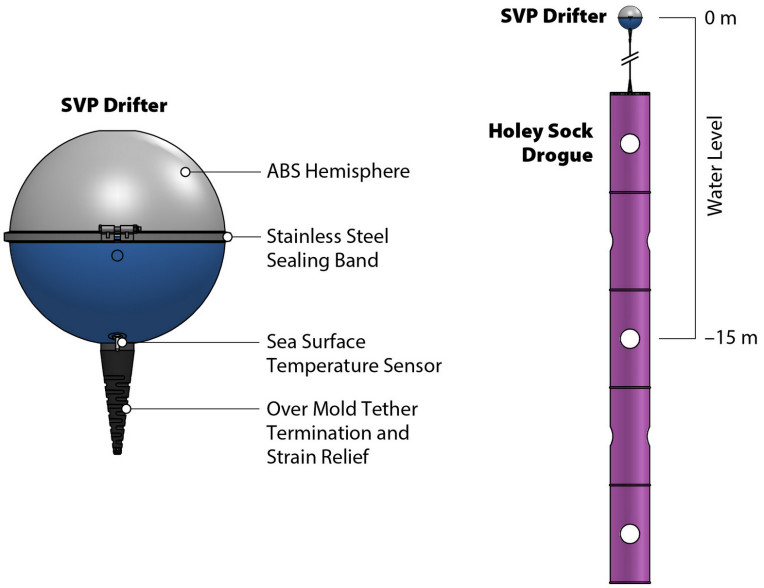

Figure 2.1: Drifter used in Paper I and II, showing the "body" of the drifter (left) and the full drifter with its drogue on the right. The body has a diameter of 35 cm. The location of the Sea Surface Temperature Sensor and the tether strain sensor are also shown. The drogue is given on the right and is centered at 15 m depth.

Mooring data and hydrography

In Paper IV, data collected from moorings and a hydrographic data set were analysed and are briefly described here for completeness. However, note that the analyses were not performed by the author of this thesis and details will therefore be omitted.

Data from 3 moorings deployed on the continental slope, were analysed. These were named Mooring South (MS), west (MW) and north (MN) (Figure 2.2). The deployments were designed to cover the core of the Slope Current (one deployment on 650 m isobath and one at 1500 m isobath) and to cover the variability along the slope (two deployments on the 650 m isobath). The moorings were densely instrumented and sampled data at a rate of an hour or less. To measure the currents, Acoustic Doppler Current Profilers (ADCP) were used and these were placed to cover the dynamic core of the Slope Current (about 10 m above sea level at the 650 m isobath and 740 m depth at 1500 m isobath, each pointing upward with a range of 550 m). Furthermore, pressure, temperature and salinity were measured using temperature loggers and CTD recorders.

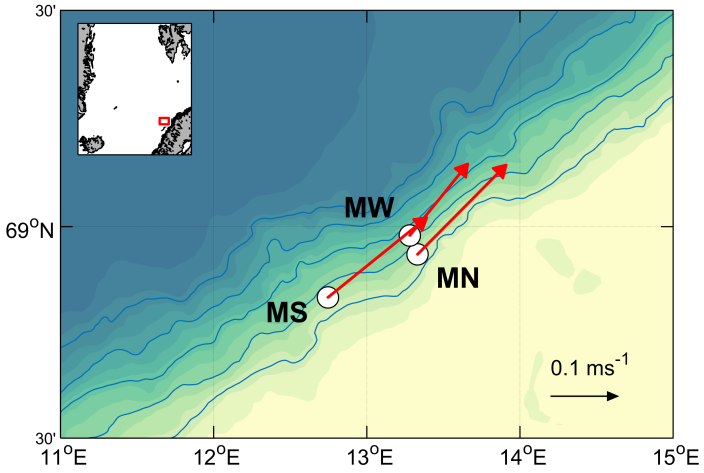

Figure 2.2: Deployment of the moorings used in Paper IV. Red box in the upper left indicate the domain. Red arrows show 200-600 m depth averaged currents at the mooring locations with scale given in lower right. Isobaths are drawn every 500 m in blue. Abbreviations are MW=Mooring West, MS=Mooring South, MN=Mooring North.

In addition, a hydrography data set of the Nordic Seas (*Bosse et al.*, 2018) was used to obtain climatological transects across the slope. This is a merged data set obtained from CTDs, ARGO floats (floats that follow the currents at depth and profile between the surface and mid-water level) and underwater gliders between 2000 and 2017. All profiles that were found within a distance of 25 km from the transect were projected horizontally onto the transect and used to compute seasonal averages of temperature and salinity.

2.2.2 Model data

Eulerian models

In this thesis, three ocean model simulations, all generated by the Regional Ocean Modelling System (ROMS), were used. ROMS is a hydrostatic primitive equation model defined on a staggered C-grid and terrain-following vertical coordinates (*Haidvogel et al.*, 2008; *Shchepetkin and McWilliams*, 2005, 2009). The models used in this thesis are:

(M1) A ROMS simulation with 4 km grid resolution, 35 vertical layers and a temporal resolution of 1 day. Model period is from 1 January 1997 to 1 January 2005 (Paper I)

(M2) A ROMS simulation with 800 m grid resolution, 35 vertical layers and a temporal resolution of 1 day. Model period is from 1 January 1996 to 1 January 2004 (Paper I)

(M3) A ROMS simulation with 800 m grid resolution, 60 vertical layers and a temporal resolution of 6 hours. Model period is from 1 January 1996 to 1 January 2000 (Papers II, III, IV)

Note that all models actually started from 1993, but to avoid the spin-up period, we removed the first years of the simulations. All models are forced identically. A fourth-order-centered scheme is used for the vertical advection of the flow while a third-order upwind scheme is used for horizontal tracer and momentum advection. No explicit horizontal eddy viscosity or diffusion is applied, but the upwind advection scheme implicitly exhibits some numerical diffusion. Vertical mixing processes that are not resolved because of grid size, are parameterized using the $k-\varepsilon$ version of the General Length Scale scheme (*Umlauf and Burchard*, 2003; *Warner et al.*, 2005). The skill of this scheme has been shown to compare favorably with laboratory experiments (*Warner et al.*, 2005). Open lateral boundaries of the model domain are relaxed toward monthly fields from the Global Forecast Ocean Assimilation Model (*MacLachlan et al.*, 2015), and the atmospheric forcing is provided with 6-hourly fields from the ERA-Interim atmospheric reanalysis (*Dee et al.*, 2011).

Given the spatial and temporal resolutions, all models are able to resolve mesoscale and some sub-mesoscale processes (*Isachsen*, 2015; *Trodahl and Isachsen*, 2018). But differences between the models are expected due to the different resolutions. For instance, regions with strong gradients in temperature/salinity leading to strong gradients in density and hence steep isopycnals are resolved differently. Due to coarser resolution, these gradients are smoothed to a larger extent in the M1 run than the M2 and M3 runs. This results in less baroclinicity in the M1 run which could therefore lead to a difference in eddy activity in the three models. The issue is relevant in our studied domain, especially along the Front Current that flows close to the Polar Front with large temperature gradients between the warm AW and the colder Polar Waters, but also closer to the continental slope, with warmer water flowing with the Slope Current than in the interior basins. A difference is indeed seen by the two estimates of EKE at surface (64 vs 330 cm^2s^{-2}) computed within the LB (Paper I) from model M1 and M2 after averaging between 1997-2005 (M1) and 1996-2004 (M2). The M2 and M3 runs therefore resolve eddies better than the M1 run. As the M3 run has a better vertical (more layers) and temporal resolution than the M2 run, this also improves its ability to resolve eddies.

The vertical resolution of the models are based on vertical layers of ROMS that follow the terrain of the bathymetry. The layer thickness is less than 10 m close to the surface and 60-100 m near the bottom, to better resolve the vertical flow in the upper ocean at a cost of worse representation of the flow towards the bottom. While the horizontal motion of the flow often is affected by large scale features such as differences in density gradients or large-scale wind patterns, the vertical motion is often affected by mixing processes associated with smaller scales. It is therefore important to have a good vertical resolution in studies involving vertical motion; hence, we use M3 in simulating 3D Lagrangian trajectories.

Lagrangian simulations

The Eulerian models presented above are helpful to provide insight about the dynamics of the flow in different locations/regions. But when it is of interest to study the

fate of water parcels as they follow the flow, the Eulerian models are not sufficient and one must consider Lagrangian particles that are advected with the flow and investigate their properties as they move. Each Lagrangian particle has an identity and can therefore be tracked through time to make it possible to compute typical pathways, as well as changes of its characteristics (such as temperature and density) along the particle trajectories. The Lagrangian simulations allow us to deploy particles several orders of magnitude more numerous than the available surface drifters in the Nordic Seas, and therefore improve the statistics in the analysis of the flow. When performing Lagrangian analysis, such as sub-sampling of data into geographical bins, the large number of deployments assures enough independent data points in each bin. This improves the statistical significance of the results (e.g., *Chinn and Gille*, 2007). In addition, since the surface drifters are deployed only in key sections and locations, the statistics of these Lagrangian observations can be limited and biased (*Davis*, 1991). In order to get the best possible representation of the flow, we perform uniform deployments (i.e., evenly distributed deployments in the model domain) in our Lagrangian simulations.

The Lagrangian simulations used/performed in this study are:

(L1) A Lagrangian 2D simulation generated from M1[1] (Paper I)

(L2) A Lagrangian 2D simulation generated from M3 (Papers II and III)

(L3) A Lagrangian 3D simulation generated from M3 (Papers II and III)

The L1 simulation is applied in Paper I to supplement the surface drifter data to improve the statistics. The daily ROMS velocity fields are used to advect Lagrangian particles to new positions after interpolating to 1-hourly time steps, by using a fourth-order Runge Kutta routine. Then the trajectories are stored at 6-hourly intervals. The particles are deployed uniformly in sets of 40×40=1,600 particles inside the box given by 64-78^oN and 15^oW-15^oE (see gray dots in Figure 2.3 a). These sets are then deployed every 8th day for about 1.5 years, giving about 115,000 particles. The particles are assigned a lifetime of one year.

The Lagrangian simulations (L2) and (L3) are computed identically with the difference that in L2 only horizontal motion (2D) is allowed whereas in L3 vertical movement is permitted (3D). These simulations are performed using OpenDrift (*Dagestad et al.*, 2018), an open source Python-based framework for Lagrangian modelling which operates offline, i.e by using a stored model velocity output. OpenDrift has been used to simulate the drift of various substances in the ocean, such as oil, search and rescue and plankton (*Dagestad and Röhrs*, 2019; *Jones et al.*, 2016; *Kvile et al.*, 2018). In this thesis, the most basic OpenDrift module for passive tracers, which advects particles solely with ocean currents, is used. The Lagrangian particle positions are updated with the 6-hourly velocity fields from M3 by applying a fourth-order Runge Kutta integration routine, either using only the horizontal velocity (2D) or the full three-dimensional velocity field (3D). Potential temperature, salinity and velocity outputs are then linearly interpolated onto the particle trajectories. The particle deployments are based on the same idea as the L1 simulation, but over a different domain and a different time period.

[1]The simulation was actually computed from another ROMS model with the same resolution and model setup. The difference from M1 was that this model did not start from rest and that it started on 01.01.1993, while M1 started on 01.07.1993

We perform uniform seeding of 40×40=1,600 particles. These sets are deployed every week between 1 January 1996 to 1 January 1999 leading to the deployment of in total 1,600×156=249,600 particles. Furthermore, the particles are deployed at three depths, 15 m, 200 m and 500 m, giving in total about 750,000 particles for both the 2D and the 3D simulation. The particles are given a lifetime of one year.

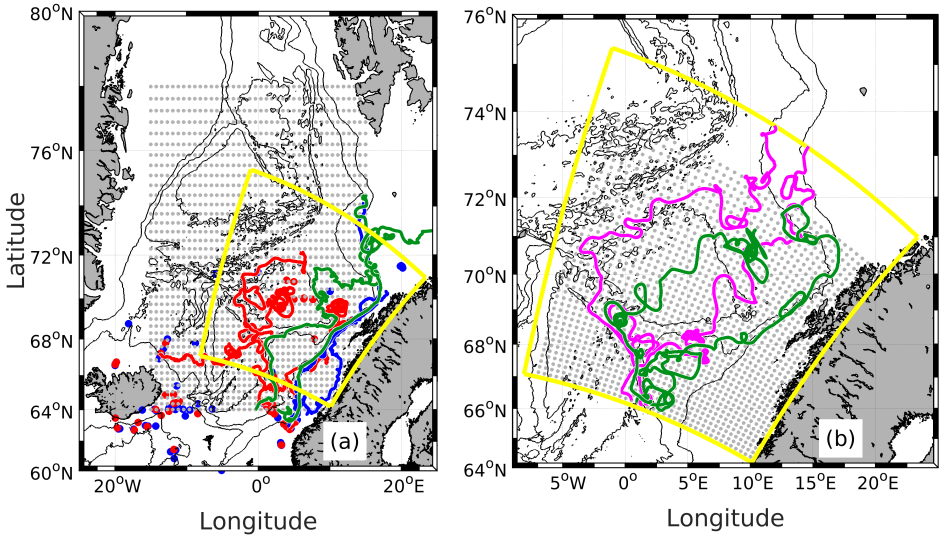

Figure 2.3: (a) Map of the deployments of surface drifters used in Paper I (red/blue dots) and the deployments of Lagrangian particles that are forced with the M1 model (gray dots). Red/blue dots indicate whether the surface drifters at some point interacted with the LB (red) or not (blue), where the LB is given by the 3000 m isobath. Red/blue trajectories are shown for the surface drifters with red/blue colors again indicating the drifters that interacted with the LB. Two example trajectories of the Lagrangian particles from the L1 simulation are shown in green. In addition we show the domain of the M2 and M3 model runs (yellow). A zoom-in to this is given in (b) with gray dots showing the deployments in the L2 and L3 simulations. Selected trajectories, 2 each from 2D particles at 15 m (magenta) and 500 m (green) in the L2 simulation are shown as examples.

All three Lagrangian simulations apply absorbing boundary conditions, i.e., a particle that runs aground or exits the model domain is terminated there. Note however, that the size of the model domains is different (Figure 2.3) such that the latter constraint will have an effect on the particles in the L2 and L3 simulations, but not in the L1 simulation. All Lagrangian simulations are performed without adding additional diffusion (random walk) to the particles. This is done to avoid making the trajectories too diffusive with respect to the transport properties of the ROMS model used to force them. Additional diffusivity is a debated topic in the Lagrangian community and discussed in Paper II. For high resolution model outputs with high frequency, which is the case here especially in the L2 and L3 simulations with the M3 model, additional diffusivity is usually avoided (see e.g., *Bower et al.*, 2011; *Gelderloos et al.*, 2017; *Rühs et al.*, 2018; *van Sebille et al.*, 2018; *Wagner et al.*, 2019).

Chapter 3

Introduction to the papers

Paper I: **Lateral Heat Transport in the Lofoten Basin: Near-Surface Pathways and Subsurface Exchange**

Dugstad, J.S., Fer, I., LaCasce, J., de La Lama, M.S., and Trodahl, M. (2019), Journal of Geophysical Research: Oceans, 124, DOI: 10.1029/2018JC014774

Paper I investigates processes related to the AW-LB exchange from surface drifter observations, Lagrangian particles deployed at surface (simulation L1) as well as from Eulerian model results (model runs M1 and M2). The Lagrangian results suggest that water from the Slope Current and the Front Current join over the Vøring Plateau to form a broad slab of water entering the LB from the south. The residence times and temperature changes computed along the drifter trajectories reveal that the associated water masses experience long residence times and large temperature losses inside the LB, implying that the slab from the south gives an important contribution to the LB heat budget. The result is consistent with Lagrangian results by *Koszalka et al.* (2013), but challenges other studies suggesting that the main AW-LB exchange appears due to eddies generated on the continental slope off Norway (*Isachsen*, 2015; *Isachsen et al.*, 2012; *Köhl*, 2007; *Raj et al.*, 2016). Therefore, the ROMS model fields are applied to compute Eulerian heat transports around a closed volume defined by the 3000 m isobath of the LB. The heat transports are computed after separating the mean flow and eddy component through Reynolds averaging. The results show that the eddy fluxes mainly dominate the net heat transport into the LB, and contradicts the results obtained from the drifters. Since the drifter results are only at surface, we therefore investigate the vertical structure of the heat transport and find that eddy fluxes dominate at deeper levels (around 600-800 m) while the mean flow is more important at surface. The temperature flux convergence (TFC) along the Lofoten Escarpment is studied by estimating $-\nabla \cdot \langle \mathbf{u}' T' \rangle$ (i.e., the eddy TFC) and $-\langle \mathbf{u} \rangle \cdot \nabla \langle T \rangle$ (i.e., the mean TFC). After averaging these quantities along the slope and obtaining vertical profiles, we observe that the divergence of eddy temperature fluxes dominates at about 400 m depth, implying that warm water is brought away from the Slope Current by eddies at these depths. Average TFC in the basin shows a convergence of eddy temperature fluxes at these levels, therefore suggesting that there can be a link between a divergence at the slope and a convergence in the basin. We suggest that the surface flow has a different pattern than subsurface levels. In the LB heat budget, the flow from the south observed from drifters is most important at the surface and the eddy fluxes are most important at depth.

Paper II: **Vertical Structure and Seasonal Variability of the Inflow to the Lofoten Basin Inferred From High-Resolution Lagrangian Simulations**

Dugstad, J.S., Koszalka, I.M., Isachsen, P.E., Dagestad, K.F., and Fer, I. (2019), Journal of Geophysical Research: Oceans, 124, 9384-9403, DOI:10.1029/2019JC015474

Paper II builds on the results from Paper I, but expands using both 2D and 3D Lagrangian trajectories at several levels (simulations L2 and L3), forced by the improved ROMS model with better temporal and vertical resolution (M3). The 2D and 3D particles which are deployed at 15 m, 200 m and 500 m are used to study the AW-LB exchange, the seasonal variability of the inflows to the basin and to compare the 2D and 3D results with each other. A relative dispersion comparison between the 2D particles deployed at 15 m and the surface drifters (which are drogued at 15 m), shows that particles reproduce the relative dispersion of the surface drifters very well.

In Paper II we identify two distinct inflows that bring AW into the LB: The Lofoten Slope Inflow from the southeast and the Helgeland Inflow from the southwest. These are pronounced at all levels in both 2D and 3D simulations. However, due to strong atmospheric cooling in winter and deep mixed layers, the 3D particles deployed at 15 m spread vertically on their way to the basin, and more 3D drifters enter the basin at deeper levels whereas the 2D drifters remain at their deployment depth. During summer, however, the strong stratification constrains the 3D drifters close to their deployment depth, resulting in a similar inflow pattern as the 2D drifters. At deeper levels (200 m and 500 m), the atmospheric cooling/warming has a smaller impact and 3D particles are less spread in the vertical.

Consistent with a deepening of isopycnals in the LB (*Bosse et al.*, 2018; *Mauritzen*, 1996), we observe a net sinking of the particles both inside the basin and as they travel towards the basin. This has an impact on the temperature changes experienced by 3D particles compared to 2D particles. Close to the surface, the 2D and 3D particles experience similar temperature changes since they are both affected by atmospheric cooling, but at deeper levels (500 m) there is a larger discrepancy. Here, the majority of the 3D particles sink and enter the basin at depths of about 550 m, and this leads to smaller temperature changes in 3D particles compared to 2D particles. But while the majority of the 3D particles sink, a smaller subset of particles that experience large cooling ($>1^o$ C), enters at about 500 m, similar to the 2D case. At deep levels we therefore speculate that the majority of the 3D particles sink below the Atlantic layer at about 500 m depth (*Bosse et al.*, 2018; *Mauritzen*, 1996), leading to less cooling as the water masses below the Atlantic layer are fairly uniform. In order to experience cooling the particles should enter the basin at the same depth as the 2D particles (500 m).

Supporting the results of Paper I, water parcels experiencing the largest cooling in the LB ($>1^o$ C) are found to enter from the south with the Lofoten Slope Inflow and the Helgeland Inflow, as well as between them. However, at deeper levels (370-600 m) the warmest water masses enter with the Lofoten Slope Inflow or other regions on the slope. This Lagrangian connection from the slope to the basin is consistent with the Eulerian studies of Paper I. We therefore suggest a vertical structure in warm inflows with a larger contribution from the eddy activity on the slope at deeper levels than at the surface.

An important finding is the differences we observe between 2D and 3D drifters. The results imply caution when interpreting results from surface drifter observations which cannot move vertically.

Paper III: **The mesoscale eddy field in the Lofoten Basin from high-resolution Lagrangian simulations**

Dugstad, J.S., Isachsen, P.E., and Fer, I. (2020), prepared for submission to Ocean Science

There is enhanced eddy activity in the LB region (*Isachsen*, 2015; *Isachsen et al.*, 2012; *Ivanov and Korablev*, 1995; *Köhl*, 2007; *Koszalka et al.*, 2011; *Raj et al.*, 2016, 2015; *Volkov et al.*, 2015). In order to improve on the studies investigating the eddy activity using Eulerian results, we study trajectories obtained from Lagrangian simulations. The simulations are the same as in Paper II (simulation L2 and L3) which are forced with the M3 ROMS model fields. The study applies the multivariate wavelet ridge analysis (MWRA) routine (*Lilly and Olhede*, 2009; *Lilly and Olhede*, 2012; *Lilly et al.*, 2011) to identify loops in trajectories and thereby identify whether a given particle is inside an eddy or not. The aim of the study is to identify, quantify and compare the cyclonic and anticyclonic eddies. These are then compared with the ambient flow (i.e., the remaining parts of the trajectory excluding eddies). We also study the vertical displacements, and temperature and density changes along trajectories for particles that are inside cyclonic and anticyclonic eddies as well outside eddies. The results also include a study of a Lagrangian net temperature and vorticity flux into the LB by looking at crossings of Lagrangian particles with the LB boundary and compute the temperature/vorticity fluxes these particles are carrying in/out to/from the basin.

Anticyclones are found to have a longer lifetime, larger radius and a more circular shape than the cyclones, suggesting a more stable character for the anticyclones. Temperature anomalies show that anticyclones are warm and cyclones are cold compared to a background state. We find that water parcels inside eddies experience larger temperature and density changes than water parcels in the ambient flow with particularly enhanced cooling in anticyclones. The cooling rates of particles are largest in the LB compared to the full domain (Figure 2.3). On average, particles downwell in anticyclones and upwell in cyclones, often associated with an increase of density. However, we hypothesize that it sometimes can also be related to along isopycnal flows or a secondary circulation within the eddies (*Bashmachnikov et al.*, 2018).

While the properties of water parcels in eddies change substantially compared to the ambient flow (i.e., larger changes in temperature and density), only about 6% of the ocean in our studied domain (see Figure 2.3) is covered by eddies. We compute temperature and vorticity fluxes into the LB by finding all entries and exits of particles with the basin and compute the temperature and vorticity fluxes brought in or out of the basin associated with these entries and exits. Since there are more particles in the ambient flow, the sum of these fluxes over all particles shows that the ambient flow gives a larger contribution to the LB heat and vorticity budgets than the eddies.

The detection and sampling of eddies using MWRA lead to under-sampling of eddies and a slightly over-sampling of the ambient flow. However, we argue that the ambient flow is so dominant that in any case it would be of large importance for the LB heat budget. As the ambient flow can include submesoscale features around eddies (i.e., filaments) that can carry strong vorticity (*Spall*, 2010), we study the importance of these filaments. We show that filaments around eddies can carry strong cyclonic vorticity and be advected to the basin. Particles in the ambient flow can therefore in some occasions bring positive vorticity and temperature fluxes into the LB and this feature is most observed at surface levels. We quantify that a small subset of about 2% of the entries/exits to/from the basin at surface (15 m) account for about 19% and 13% of the total net vorticity and temperature flux to the basin respectively. The filaments

therefore play a significant role to the heat and vorticity budgets of the basin, consistent with *Spall* (2010) that found from idealized model studies that filaments having strong cyclonic vorticity can be advected to basins offshore from an eastern boundary current (similar to the Slope Current).

Paper IV: **Norwegian Atlantic Slope Current along the Lofoten Escarpment**

Fer, I., Bosse, A., and Dugstad, J.S. (2020), Ocean Science, 16, 685-701, DOI:10.5194/os-2020-15

In Paper IV we describe the Slope Current at the Gimsøy section off the Lofoten Escarpment (13^oE,69^oN) after analyzing observations from moorings deployed as a part of the ProVoLo project. We investigate the along-isobath current between 200 and 600 m depth and find an average speed of 0.15 ms^{-1} and a volume transport of 2.0$\pm$0.8 Sv (1 Sv=$10^6 m^3 s^{-1}$). The largest volume transport is also found for the highest temperature classes (water masses with temperature $>7^oC$). In contrast with earlier observations obtained from Svinøy (*Orvik et al.*, 2001; *Orvik and Øystein Skagseth*, 2003) showing a barotropic Slope Current, we identify a baroclinic component in the Gimsøy section. The climatological structure identifies that the geostrophic shear computed from thermal wind balance is positive and larger in the Slope Current at Gimsøy than at Svinøy. At Gimsøy we observe that the temperature contribution to the shear dominates the contribution from salinity, but at Svinøy the temperature and haline contributions have different signs leading to a cancelling effect. At Gimsøy we also observe a positive shear driven by salinity at the shelf, likely caused by interaction with the Norwegian Coastal Current.

Barotropic and baroclinic conversion rates are computed both from moorings (MN and MW in Figure 2.2) and from model estimates. We find that while the barotropic conversion rates (i.e conversion from mean to eddy kinetic energy) are likely negligible over the Lofoten Escarpment, the baroclinic conversion rates (conversion from available potential energy to eddy kinetic energy) can be substantial with volume-averaged values of (1-2)$\times 10^{-4}$ Wm^{-3}.

My contribution to this paper was to compute barotropic and baroclinic conversion rates over the Lofoten Escarpment from the ROMS model run M3. This was done both as a volume-averaged estimate, and at the same locations as the mooring instruments at the slope (MN and MW) to make a direct comparison. A segment between the MN and MW mooring locations was also made to compute the conversion rates along this segment. This gave a better statistical evaluation as the computation was obtained from about 40 grid points instead of only two virtual moorings (two grid points). The model-based calculations were useful to conclude on the reliability of the calculations based on limited observations from the two moorings.

Additional contribution

Ypma, S.L., Georgiou, S., **Dugstad, J.S.**, Pietrzak, J.D., Katsman, C.A. *Pathways and water mass transformation along and across the Mohn-Knipovich Ridge in the Nordic Seas*. Journal of Geophysical Research: Oceans. Accepted for publication August 2020.

Chapter 4

Conclusions and outlook

4.1 Main conclusions

This thesis addresses the important role the LB plays in the modification of AW flowing northwards towards the Arctic. Strong atmospheric cooling leads to large surface heat losses and a substantial modification of the water masses there. The thesis discusses eddy exchange on the slope as well as inflows and outflows to the basin from both Lagrangian and Eulerian estimates. The importance of the inflows to the LB heat and vorticity budgets are studied. Furthermore, the vertical structure and seasonal difference of the inflows are investigated. A quantification of eddies using wavelet analysis is performed to estimate the relative importance of eddies and the ambient flow for transporting heat and vorticity into the LB.

The LB is the basin giving the largest surface heat loss in the Nordic Seas, and the net heat transport into the LB is larger than for any other basin (Paper I). Due to atmospheric cooling and deep mixed layers, a deep signature of warm waters in the LB is maintained. Heat transports computed from Eulerian models indicate a dominance of eddy fluxes averaged over the whole water column, consistent with earlier literature suggesting eddy exchange from the continental slope to the LB. However, surface drifter observations and model surface particles show a large AW-LB exchange in the southern part of the basin and this is associated with a mean flow into the basin in the south (Paper I). Eddy heat transport into the basin shows a peak at about 600-800 m, consistent with large divergence of eddy temperature fluxes close to the Lofoten Escarpment at about 400 m. The eddy fluxes are important at deeper levels (Papers I and II). The findings are consistent with large baroclinic conversion rates at 400 m depth (computed from moorings) and between 100-1000 m (volume-averaged, computed from the M3 run) at the Lofoten Escarpment (Paper IV), implying that potential energy is extracted from the Slope Current to feed eddies generated there. The transport along the Slope Current is dominated by high temperature classes ($> 7^{o}$C). Large baroclinic conversion rates from the moorings, supported by the model results, therefore indicate that eddies created on the slope can carry large amount of heat to the ocean interior (Paper IV).

The exchange of AW from the slope to the basin is largest for particles at deeper levels (Paper II). The Lagrangian trajectories show that surface waters that are cooled in the basin enter from the south, while at deeper levels (about 500 m), the warm waters come from the slope, implying a bigger impact of eddies at depth. Surface inflow to the basin is weaker in winter (less particles because of vertical spreading of particles in the deep mixed layers by vertical mixing) than during summer (more particles, strong stratification makes the particles stay on their deployment depth). Based on a wavelet ridge analysis of Lagrangian trajectories (Paper III), we conclude that anticyclones are larger, more circular, more stable and have longer life-

times than cyclones. Temperature anomalies show that anticyclones are warm while cyclones are cold compared to a background state. On average, the water parcels in anticyclones lose heat and downwell while the opposite is true for water parcels in cyclones. The vertical motion is partly related to changes in water properties (changes in temperature and density), but also to flow along steepening isopycnals or secondary circulation within the eddies. Stronger cooling and warming rates in eddies imply that they are important for the LB heat budget. However, the integrated, Lagrangian net temperature and vorticity fluxes into the basin are dominated by the ambient flow since a relatively small number of Lagrangian particles are trapped in eddies (about 30%), and an even smaller fraction of all drifter data points are ridge (coherent vortex) points (6%). While this dominance is distinct close to the surface, the difference is smaller for the particles deployed at 500 m. At these levels, anticyclones generated at the slope are important for carrying heat into the LB. Large vorticity and temperature fluxes into the basin from the ambient flow (especially at 15 and 200 m) can be related to both the mean flow component or the variability due to submesoscale features. About 2% of the 2D particles at 15 m contribute with 19% and 13% of the net vorticity and temperature fluxes into the LB, respectively. Narrow filaments around coherent vortices and eddies can give significant contributions to the LB vorticity and heat budgets in the upper layers.

4.2 Outlook

The transformation of AW in the Norwegian Sea plays an important role in the Atlantic Meridional Overturning Circulation which can impact features such as sea ice cover and production of deep waters in the Arctic. Currently, the Arctic Ocean is losing sea ice in all regions during all seasons (*Onarheim et al.*, 2018; *Serreze et al.*, 2007) and there is an anti-correlation between heat transport into the Arctic Ocean and the sea ice extent (*Årthun et al.*, 2019), i.e., increased ocean heat transport leads to reduction in sea ice. As the AW is modified in the LB, and the water mass properties are changed due to cooling and densification, the AW-LB exchange can have an impact on the sea ice extent as these water masses later enter the Arctic. 30-50% of the surface drifters in the Nordic Seas deployed south of the LB interact with the basin (Paper I,II). Due to the increased residence time and cooling, these water masses are likely colder when they enter the Arctic Ocean compared to water masses following the Slope Current that have a shorter transit time northwards. The cooling of the associated water masses in the LB therefore likely reduces the Arctic sea ice melt compared to water masses from the Slope Current. The understanding and quantification of how the Slope Current interacts with the LB (such as given in Paper I,II) can therefore be of importance to understand the sea ice cover in the Arctic in a global warming world.

The temperature gradient between the cold atmosphere and the warm inflow of AW to the Nordic Seas, creates large surface heat losses to the atmosphere that are about the strongest in the world (*Huang*, 2015). The inflows to the Nordic Seas are therefore important for the regional climate of western Europe (*Rhines et al.*, 2008; *Seager et al.*, 2002). In this thesis, the surface heat loss in the LB was found to be 2-4 times larger than for the Greenland Basin and Norwegian Basin (Paper I) in agreement to earlier literature (*Richards and Straneo*, 2015). The proximity of the LB as well as the warm Slope Current to the Norwegian Coast, therefore implies a warm regional climate in Norway relative to its latitude.

In addition to the export of heat, the off-shelf transport of AW from the slope due to eddies or other variability in the flow (Paper I,II,III,IV) can also bring nutrient waters that can affect the fish habitat in the region. Pelagic juvenile are found to be exported laterally with the off-shelf transport, and during one year about 27.4% of the pelagic juvenile from spawning

grounds on the slope can be brought to the ocean interior (*Strand et al.*, 2017). The off-shelf transport is considered harmful for the cod stock in the region, which has a natural habitat on the slope. Pelagic eggs, larvae etc. that drift to the ocean interior are often considered as lost for recruitment for the cod stock (*Werner et al.*, 1997). An increased off-shelf transport to the ocean interior could therefore reduce the available food close to the slope and impact the cod stock. An understanding an forecasting of these events could be helpful for the large fish industry in these regions.

4.3 Future perspectives

This thesis improves the understanding of the ocean circulation in the Norwegian Sea with a main focus on the AW-LB exchange, pathways, the modification of water masses in the LB and how the AW is modified in eddies compared to the ambient flow. Focus is on the subsurface processes, thereby dividing the surface and subsurface circulation into separate studies. While it is possible to compare our upper ocean Lagrangian results with surface drifter observations and satellite altimetry, such comparisons are not possible at depth. The few existing trajectories from acoustically-tracked subsurface floats (≈ 20) are not enough to make a statistical comparison with particles obtained from a Lagrangian model. Therefore, when interpreting the subsurface particles studied in Paper II and III, we rely on the good comparison between the observed and modelled surface drifters, and assume that the subsurface trajectories are representative of the nature. A direct comparison with subsurface floats is therefore needed and more deployments of subsurface floats and ARGO floats should therefore be a priority. Such observations are important to understand the processes leading to the AW-LB exchange at depth and could possibly verify some of the results in this thesis, for instance the vertical structure of inflow of warm waters to the basin. The different results obtained from the studies of 2D and 3D particles (Paper II and III) also emphasize the need for change in design of subsurface floats. Subsurface floats today are mainly designed to be isobaric, i.e., approximately follow a constant depth. But the actual flow is not isobaric; the water masses can move vertically due to vertical changes in isopycnals. Isopycnal floats exist but they are few, and in this case one would also lack information about the diabatic transformations experienced by the water parcels. The design of appropriate floats to describe the vertical motion of the flow, as well as numerous deployments of these floats should therefore be prioritized to obtain a better statistical representation of the 3D subsurface flow in the Nordic Seas.

The Slope Current is well studied, but measurements along the Front Current are scarce. This is a relatively colder current that serves the LB with less heat, but the hydrography along the current is not studied in detail. More observations over the Helgeland Ridge and the Mohn Ridge would provide more insight. Gliders have provided useful data in the Lofoten Basin and at the Mohn Ridge (*Bosse and Fer*, 2019b; *Yu et al.*, 2017), and *Bosse and Fer* (2019b) estimated a northward volume transport of about 4.6 Sv in the Front Current over the Mohn Ridge. However, little is known about the interaction between the Front Current and the colder Polar Waters from the Greenland Sea. The exchanges between these different water masses are expected to be small due to the topography, but they are not known. The extent of the Front Current is also uncertain. *Orvik et al.* (2001) and *Orvik and Niiler* (2002) suggested that this is a baroclinic current flowing on the west of the LB, over the Mohn Ridge and further the Knipovich Ridge before it again merges with the Slope Current closer to Fram Strait. But, recent Lagrangian studies suggest that the Front Current is not necessarily a coherent current in the Lagrangian sense. *Ypma et al.* (2020) (see additional work) observed from both observations and models that very few Lagrangian drifters/particles follow the Front Current

from south of LB to Fram Strait, which is different from the Slope Current where this is observed frequently. Instead a large amount of the drifters/particles move eastward and follow the topography north of the LB to join the Slope Current at lower latitudes. More observations using drifters, subsurface floats, gliders and moorings over the Mohn Ridge and north of the LB could provide further insight in the exchange between the Front Current and the Polar Water, and the lateral and poleward extent of the Front Current. This would help to understand the characteristics of waters carried in the Front Current in the gateway to the Arctic Ocean.

The ROMS runs M2 and M3 provide an improved spatial and temporal resolution that can extend the knowledge obtained from earlier numerical model studies of the Lofoten Basin (*Bashmachnikov et al.*, 2018; *Trodahl and Isachsen*, 2018; *Volkov et al.*, 2015). In this thesis, the models are used to perform Lagrangian simulations that are used to detect eddies using the MWRA routine (Paper III). We speculate that the eddies are slightly under-sampled. Some of this could be related to the MWRA routine, but we also found that it could be related to the nature of eddies; due to strong gradients in potential vorticity between eddies and the ambient flow, the water masses in the ambient flow cannot penetrate the eddies easily (shown for the LBE, *Bosse et al.* (2019)). It would therefore be of interest to compare results from Paper III with results from eddies detected using an Eulerian approach with similar resolution as M2 and M3.

Whether large scale climate models in the Atlantic Ocean should be able to resolve eddies and model the northward heat transport correctly is an open question. Our study indicates that 6% of the model domain is covered by eddies (coherent vortices), and could suggest a smaller importance of resolving these. But the ocean is chaotic with large variability that is not necessarily eddies. Eulerian studies of eddies and other variability in the flow, and their relative importance to heat budgets in various regions in the Nordic Seas would therefore supplement our study. The choice of the Eulerian model needs care. The terrain-following layers of ROMS have steep slopes from the deeper basins towards the Norwegian coast. The pressure gradients on the slope could therefore be estimated in error due to interpolation errors when performing the differentiation. Using a model with z-coordinates on fixed levels (for instance MITgcm) this would be avoided. On the other hand, the terrain-following layers of ROMS provide a better vertical resolution on the slope compared to MITgcm. Eulerian studies using both models could therefore be performed and compared to each other, to provide better answers to whether climate models of the North Atlantic and the Arctic Ocean should be required at high resolution.

Lastly, results obtained in this thesis can provide insight into other regions with similar bathymetry. The bathymetry with a continental slope to the east with an eastern boundary current flowing along it together with a deeper basin to the west, can also be seen in the Labrador Sea, where large EKE values adjacent to steep topography are found (*Prater*, 2002), implying similar dynamics to the Lofoten Basin. Results in this thesis could therefore be a good motivation for further studies in the Labrador Sea as well as other regions with similar bathymetry.

Chapter 5

Scientific results

Paper I

Lateral Heat Transport in the Lofoten Basin: Near-Surface Pathways and Subsurface Exchange

J.S. Dugstad, I. Fer, J. LaCasce, M.S. de La Lama, M. Trodahl
Journal of Geophysical Research - Oceans, **124** (2019)

JGR Oceans

RESEARCH ARTICLE
10.1029/2018JC014774

Lateral Heat Transport in the Lofoten Basin: Near-Surface Pathways and Subsurface Exchange

Johannes Dugstad[1], Ilker Fer[1], Joe LaCasce[2], Martha Sanchez de La Lama[2], and Marta Trodahl[2]

[1]Geophysical Institute and Bjerknes Centre for Climate Research, University of Bergen, Bergen, Norway, [2]Department of Geosciences, University of Oslo, Oslo, Norway

Key Points:
- Surface drifters with long residence time in the Lofoten Basin are advected over the Vøring Plateau
- Surface drifters do not capture eddies shed from the slope current off the Lofoten Islands
- Heat advection from south dominates near surface; eddy fluxes from slope dominate subsurface

Correspondence to:
J. S. Dugstad,
johannes.dugstad@uib.no

Citation:
Dugstad J., Fer, I., LaCasce, J., Sanchez de La Lama, M., & Trodahl, M. (2019). Lateral heat transport in the Lofoten Basin: Near-surface pathways and subsurface exchange. *Journal of Geophysical Research: Oceans*, *124*. https://doi.org/10.1029/2018JC014774

Received 16 NOV 2018
Accepted 14 APR 2019
Accepted article online 22 APR 2019

Abstract The Lofoten Basin in the Nordic Seas plays a central role in the Atlantic overturning circulation by acting as a reservoir for the warm and saline Atlantic Water flow toward the Arctic Ocean. The mass and heat exchange between Atlantic Water and the Lofoten Basin impacts the water mass transformations and the surface heat loss, but the processes governing this exchange are not well understood or quantified. Here we study the circulation in the Nordic Seas and the heat transport in the Lofoten Basin using a combination of Lagrangian and Eulerian methods. We analyze the trajectories of about 150 surface drifters, augmented with a set of about 47,000 surface trajectories calculated using the output from a regional numerical simulation, to investigate the drifter pathways and their exchange with the Lofoten Basin. The drifters reveal that water parcels with long residence time inside the basin contribute substantially to the heat loss and typically enter from south across the outer rim of the Vøring Plateau and, to some extent from east, from the eastern branch of the Norwegian Atlantic Current. The main contributors to the lateral heat transport to the Lofoten Basin are the near-surface heat transport by the mean flow in the southern sector of the basin and the subsurface eddy fluxes from the Lofoten Escarpment in the east.

1. Introduction

The Nordic Seas (the Norwegian, Iceland, and Greenland Seas) are a key region for the northward-flowing warm water masses from the North Atlantic Ocean toward the Arctic Ocean (Rossby et al., 2009; Segtnan et al., 2011). In this study, we focus on the Lofoten Basin (LB) of the Norwegian Sea, an area of importance for the heat transport of the northward-flowing Norwegian Atlantic Current (NwAC) (Bosse et al., 2018; Isachsen, 2015; Köhl, 2007; Raj et al., 2015; Volkov et al., 2015). At the Vøring Plateau, the NwAC splits into an eastern and western branch (Figure 1), each transporting warm water toward higher latitudes. These branches, later referred to as the "Slope Current" and the "Front Current," respectively (Orvik & Niiler, 2002), bound the LB and affect the exchange of water masses between the currents and the basin. The LB is a major heat reservoir in the Nordic Seas (Nilsen & Falck, 2006), manifested in the satellite sea surface temperature imagery (Koszalka et al., 2012), showing a warm wedge of water between the NwAC branches. Pooling of the warm Atlantic Water (AW) creates large buoyancy losses (Richards & Straneo, 2015), giving rise to convection and deep mixed layers (Bosse et al., 2018; Raj et al., 2015). Deep-reaching winter convection and vertical mixing in the western part of the LB substantially modifies the AW (Bosse et al., 2018).

The prevailing notion is that the mesoscale eddy field plays an important role in mediating the mass and heat exchange between the AW and LB. This in turn produces a substantial heat loss in the area, permitting the water masses to become denser and possibly sink as they later approach the Arctic. Even though the heat loss and convection are spread throughout the basin, the mean downwelling in the LB is localized to small segments of its eastern boundary current (the Slope Current) along steep slopes where eddies are shed (Spall, 2010). Earlier studies suggested that a significant portion of the exchange between the NwAC and the LB is a result of this eddy shedding from the Slope Current (Isachsen, 2015; Isachsen et al., 2012; Köhl, 2007; Rossby et al., 2009; Volkov et al., 2013). The Slope Current flows along steep topography off the Lofoten Escarpment, where it can reach velocities of 1 m/s (Andersson et al., 2011) and become unstable. Isachsen (2015) showed that the steep continental slope off the Lofoten-Vesterålen Islands exhibits enhanced unstable baroclinic growth rates and large velocity variability, suggesting high lateral diffusion rates. Investigating heat flux convergence, Isachsen et al. (2012) suggested that warm core eddies from the Slope

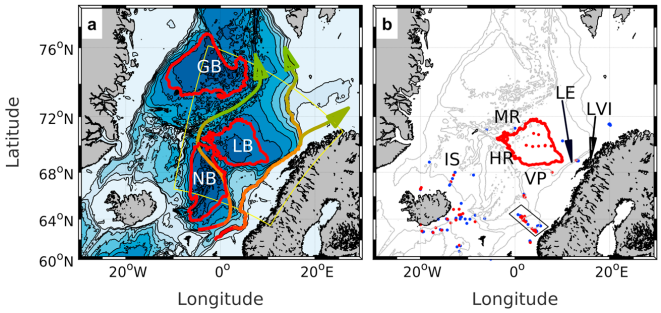

Figure 1. (a) Bathymetry of the Nordic Seas showing the typical pathways of the Norwegian Atlantic Current, indicated by arrows. Depth contours are given every 400 m. Red contours outline the three basins used in the analysis, defined by their 3,000-m isobaths. The yellow border is the domain of the ROMS 800-m model; (b) the deployment/starting positions of all 149 observed drifters analyzed in this study. Dots mark the drifters that interacted (red) or did not interact (blue) with the LB. The LB (red) and the 1,000-, 2,000-, and 3,000-m isobaths (gray) are shown. The black box encloses the Svinøy section drifters. The abbreviations which are distributed over both panels for better visibility are GB = Greenland Basin; NB = Norwegian Basin; LB = Lofoten Basin; IS = Iceland Sea; HR = Helgeland Ridge; MR = Mohn Ridge; VP = Vøring Plateau; LE = Lofoten Escarpment; LVI = Lofoten-Vesterålen Islands.

Current could transport warm water offshore. These eddies are typically anticyclonic and drift westward where the topographic depression attracts them toward the center of the LB (Köhl, 2007; Volkov et al., 2013). Based on eddy-resolving numerical models, Volkov et al. (2015) reported that the eddies are shed where the shelf topography is steepest and that they move along a cyclonic path toward the center of the basin.

In addition to the slope exchange with the basin, a feature that has gained attention is the Lofoten Basin Eddy (LBE). This quasi-permanent anticyclonic eddy in the western part of the LB (Ivanov & Korablev, 1995; Søiland & Rossby, 2013) is associated with a local maximum of sea surface height variability and eddy kinetic energy (EKE) (Köhl, 2007; Volkov et al., 2015). Evolution of the LBE core using Seaglider observations (Yu et al., 2017) showed a mean eddy radius of 18 km and an anticyclonic azimuthal peak velocity between 0.5 and 0.7 m/s at depths between 700 and 900 m. Fer et al. (2018) reported increased turbulent dissipation rates associated with large shear beneath the azimuthal velocity maximum and from subinertial energy trapped by the negative vorticity of the eddy. The LBE kinetic energy is suggested to be maintained by merging with anticyclonic eddies shed from the Slope Current (Köhl, 2007; Raj et al., 2015; Volkov et al., 2015). The heightened eddy variability is also illustrated by surface drifter data (Koszalka et al., 2011; Laurindo et al., 2017), which showed local enhancements in the horizontal distribution of lateral diffusivity in the LBE region and along the Slope Current off the Lofoten Escarpment.

The previously cited studies suggest mechanisms and pathways for the lateral heat transport into the LB; however, these are not fully understood or quantified. Here we seek to understand how the high sea surface temperatures and the large surface heat fluxes in the LB are maintained, by investigating pathways and circulation of AW and the role of advection and eddy fluxes. We analyze observations from in situ surface drifters, augmented by a set of surface trajectories computed from a 4-km horizontal grid resolution regional model of the Nordic Seas. The 4-km domain spans a large area, allowing us to estimate near-surface pathways into the LB. We assume that the surface drifters are representative of the near-surface water mass paths and exchanges. Volume-integrated heat transports for the major basins of the Nordic Seas, computed using this model, highlight the importance of the LB. We study the LB in detail, by increasing the grid resolution to 800 m, in a smaller model domain which focuses on the Lofoten region (yellow border in Figure 1a). The 800-m resolution resolves the mesoscale eddies, allowing us to estimate the relative contribution of heat transport associated with the mean flow and with the eddy fluxes.

The warm core eddies that merge with the LBE make a substantial contribution to the surface heat loss since the associated water parcels will experience long residence times in a colder environment. The typical pathways of surface drifters reaching the LB, however, suggest a broad entry of AW along the southern part of the basin instead of from the east, which would be expected from eddies shed from the Lofoten Escarpment. Our findings also emphasize the role of subsurface processes, consistent with Rossby, Ozhigin, et al. (2009)

and Rossby, Prater, and Søiland (2009), who reported a higher percentage of subsurface RAFOS floats that entered the LB from the Slope Current than for surface drifters. Thus, the eddy shedding from this region may have a stronger signature in deeper layers than near the surface.

The paper is organized as follows. The observed drifter data, the trajectories from numerical calculations, and the description of the numerical models used are presented in section 2. In section 3.1, we present integrated properties from all major basins of the Nordic Seas, using the 4-km model, to set the context and emphasize the role of the LB in the Nordic Seas. Pathways and statistics from the Lagrangian analysis are presented and discussed in section 3.2 using observed drifters and trajectories obtained from the 4-km model fields. Using the eddy-resolving 800-m model, we then concentrate on the LB and quantify the contribution of mean and eddy fluxes and of surface and subsurface signatures dominating the heat budget of the LB (section 3.3). Concluding remarks are summarized in section 4.

2. Data and Methods

2.1. Surface Drifter Data

We study the trajectories of all available surface drifters, 571 in total, that were deployed in or entered the Nordic Seas between 1991 and 31 December 2017. These data were obtained from the Global Array Drifter Program (Lumpkin et al., 2013). The GPS-tracked surface drifters are drogued at 15-m depth, with a near-surface temperature sensor at approximately 0.3 m with 0.1-K resolution. Real-time drifter data can be unevenly sampled, with a sampling frequency changing from 1 hr to, in some occasions, 1 day. Therefore, drifter positions are quality-controlled and interpolated by a kriging method to 6-hr intervals by the Atlantic Oceanographic and Meteorological Laboratory (AOML) and the National Oceanic and Atmospheric Administration (NOAA) Drifter Data Assembly Center (Lumpkin & Pazos, 2007), transmitting data of longitude/latitude, zonal/meridional velocities, and temperature. In total, the set of drifters gives approximately 140,000 days of data, spanning 30 years. We determine pathways, entry/exit positions into and out of the LB, and link the residence times inside the basin with the entry/exit positions and to each drifter's deployment location. The LB is defined as the region lying within the 3,000-m isobath (Figure 1), a contour that is approximately closed, with one exception being a 28-km-long segment in the southwest toward the Norwegian Sea between the coordinates [0.78°W, 69.3°N] and [0.84°W, 69.5°N]. We manually closed this segment. Since our main interest is to investigate the pathways of warm AW, we exclude the drifters that were deployed north of the LB or which never reached the latitudes of the LB.

Out of a total of 571 drifters, we selected 149 drifters for analysis. Of the rejected drifters, 128 lost their drogue upon deployment, 21 lacked drogue information, 66 were deployed north of the LB, and 207 did not reach the LB latitudes. Of the latter 207, 81 drifters ran aground near Iceland or along the western coast of Norway, and 126 stopped transmitting good-quality data (three from poor battery performance and the remaining 123 because of rough seas).

Drifter mortality is a problem in the Nordic Seas. The drifter population experiences a nearly exponential decay in time after deployment (Koszalka et al., 2012). The subset of drifters selected in this study has an e-folding time scale of 190 days, less than half the value given in Lumpkin et al. (2012). A typical drifter propagating northward from areas around Iceland travels a distance of approximately 900 km to reach the center of the LB, in more than 100 days with an average speed of 10 cm/s. Drifter mortality therefore complicates the estimation of drifter interaction with the LB.

2.2. Trajectories From a Numerical Model

The observed drifters are deployed geographically nonuniform, in selected key sections and locations, and our data selection further reduces the number of drifters studied. In such a scarce and nonuniform data set, the statistics of the Lagrangian observations are limited and biased (Davis, 1991). Therefore, we generate a set of surface trajectories of water parcels forced by a numerical model of the Nordic Seas with 4-km grid resolution (the model is described in section 2.3). In the following, we refer to these trajectories as "synthetic drifters." The synthetic drifters disperse in a quantifiable manner and therefore permit the investigation of a number of trajectories several orders of magnitude larger than for observed drifters. This improves the statistical significance. Furthermore, we can conduct controlled and uniformly distributed releases to reduce the bias.

The synthetic drifter data set consists of approximately 115,000 particles deployed in the Nordic Seas. The seeding is in uniform groups, inside the box given by 64–78°N and 15°W–15°E, with $40 \times 40 = 1,600$

drifters. The groups of 1,600 drifters are deployed at the same location, every eighth day over a period of 1.5 years. The daily velocity fields from the 4-km model (see section 2.3 for details) are used to advect the drifters to new positions after interpolating to 1-hourly time steps, by using a fourth-order Runge Kutta routine. The trajectories are then stored at 6-hr intervals. Assuming that all information about the flow is contained in the model velocity fields, we do not add explicit diffusion in the simulations. The simulations for each group are run for 1 year; hence, drifter lifetimes are limited to 1 year. The model applies absorbing boundary conditions, that is, a drifter which runs aground is terminated. The model domain is large, and the synthetic drifters do not reach the model's open ocean boundary during their lifetime. The calculations are 2-D; hence, no vertical exchange is allowed. To be consistent with observations, we exclude all drifters deployed north of the LB or those that do not reach the latitudes of the LB, giving approximately 47,000 trajectories for analysis.

2.3. Eulerian Calculations

The Eulerian calculations are based on the Regional Ocean Modeling System (ROMS) simulations. ROMS is a primitive equation model with free surface and terrain-following vertical coordinates and is horizontally gridded as a staggered C-grid (Haidvogel et al., 2008; Shchepetkin & McWilliams, 2005, 2009). Results from two model domains are analyzed. Our relatively coarse horizontal resolution (4 km) model covers all the Nordic Seas (see Figure 2 in Trodahl & Isachsen, 2018, for the full domain) and allows us to compare different basins. A smaller domain with 800-m resolution was constructed to provide eddy-resolving output focused on the LB. Both models consist of 35 vertical layers and are stored as daily averages. This temporal resolution is sufficient to resolve the mesoscale and submesoscale processes (Isachsen, 2015; Trodahl & Isachsen, 2018). The models also span similar time periods. The 4-km model covers from 1993 to 2005, while the 800-m model duration is 1 year shorter, from 1993 to 2004, because of limited computational resources.

The two simulations are forced identically and share the same model setup. A fourth-order-centered scheme is used for vertical advection and a third-order upwind scheme for horizontal tracer and momentum advection. The upwind advection scheme implicitly includes some biharmonic diffusion. No explicit horizontal eddy viscosity or diffusion is applied. Small-scale vertical mixing is parameterized by the k-ϵ version of the General Length Scale scheme (Umlauf & Burchard, 2003; Warner et al., 2005). The open lateral boundaries are relaxed toward monthly fields from the Global Forecast Ocean Assimilation Model (MacLachlan et al., 2015), and the atmospheric forcing is provided by 6-hourly fields from the ERA-interim atmospheric reanalysis (Uppala et al., 2005). Runoff from primary rivers are supplied by monthly climatologies. The 4-km model was validated and analyzed in Trodahl and Isachsen (2018).

Due to the larger model domain, the 4-km simulation requires a longer spin-up time than the 800-m simulation. Taking this into account and requiring the same time span for consistency, we analyze the 8-year period from 1 January 1997 to 1 January 2005 for the 4-km model and from 1 January 1996 to 1 January 2004 for the 800-m model.

Using the 4-km model, we compute the mixed layer depth (MLD) in the LB, the Norwegian Basin, and the Greenland Basin (see Figure 1a for their locations). The MLD is obtained as the depth at which the density increases from its surface value by 0.01 kg/m^3 (Peralta-Ferriz & Woodgate, 2015; Toole et al., 2010). The maximum MLD in each grid point is the maximum value over the simulation time span. In addition, we integrate the net surface heat flux over each basin, using the annual averaged fluxes in the corresponding 8-year analysis period. We compare this to the net heat transport into each basin computed around the closed basin contours using

$$\mathrm{HT} = \rho C_p \int_H \int_S \langle \mathbf{U}T \rangle \cdot \mathbf{n} \, ds \, dh. \tag{1}$$

Here ρ is the density of seawater, C_p is the specific heat capacity, $\mathbf{U} = (u, v)$ is the horizontal velocity vector, T is the temperature, ds and dh are length elements around the basin contour of integration and in the vertical, respectively, and $\mathbf{n}$ is the unit normal vector pointing into the basin. Thus, positive values indicate heat transport into the basin. The vector $\langle \mathbf{U}T \rangle$ is time averaged in the same way as the surface heat flux, indicated by the angle brackets. Normally, the heat transport should be computed relative to some reference temperature T_{ref}. However, note that we integrate over the entire water column and that the basin contours are closed. Thus, we operate with closed volumes, and because of mass conservation, the term associated with T_{ref} will not contribute to the integral. Since the currents in the Nordic Seas are, to a large extent,

Table 1
Surface Area, Integrated VB, Integrated HT, SHL (Temporal Mean ± Standard Deviation), Average Maximum MLD, and Surface EKE for the LB, the NB, and the GB for the 4-km Model

Basin	Area (10^5 km^2)	VB (Sv)	HT (TW)	SHL (TW)	Max. MLD (m)	EKE (cm^2/s^2)
LB	1.1	0.0	7.3 ± 2.7	5.2 ± 1.2	480	64.2 (330.0)
GB	1.2	0.3	0.6 ± 0.8	2.0 ± 0.8	580	44.3
NB	1.7	−0.3	2.6 ± 2.1	1.4 ± 1.0	190	38.7

Note. The EKE in the LB from the 800-m model is also given in brackets. Averaging is over the full 8-year period (1 January 1997 to 1 January 2005). Standard deviations are computed from the year-to-year variability over the analyzed period. 1 TW = 10^{12} W; 1 Sv = 10^6 m^3/s. VB = Volume transport Balance; HT = Heat Transport; SHL = Surface Heat Loss; MLD = mixed layer depth; EKE = eddy kinetic energy; LB = Lofoten Basin; GB = Greenland Basin; NB = Norwegian Basin.

topographically steered (Isachsen et al., 2003; Nøst & Isachsen, 2003), the basin contours are defined by the 3,000-m isobaths on the ROMS model grid, similar to the LB definition applied for the drifter analysis. Since the velocity variables are located on the borders of the staggered grid cells, we define the points on the basin contours to be located in the corners of these grid cells, the so-called psi points. We further define the vectors between the psi points on the basin contours to be purely horizontal or vertical, thus avoiding interpolation of velocity when integrating the heat transport around the contour.

For a more detailed analysis with focus in the LB, we take advantage of the eddy-resolving 800-m resolution model results. Calculations of surface heat flux and the heat transport in the LB are done identically to the 4-km model. Additionally, to quantify the relative contribution of the mean and eddy components, we apply Reynolds averaging of the daily-mean fields

$$\langle uT \rangle = \langle u \rangle \langle T \rangle + \langle u'T' \rangle . \tag{2}$$

A similar equation is applied on the v velocities. Here $u = \langle u \rangle + u'$ and $T = \langle T \rangle + T'$, where $\langle u \rangle$ and $\langle T \rangle$ are time averages and u' and T' are the corresponding perturbation fields. EKE density is computed as $\frac{1}{2}\left(\langle u'^2 \rangle + \langle v'^2 \rangle\right)$. To exclude the seasonal variability in the computation of the eddy fluxes, the averages are calculated over four periods during a year, that is January–March, April–June, July–September, and October–December. Annual averages are then obtained by averaging over the four values each year between 1 January 1996 and 1 January 2004 or for some scenarios over the entire 8-year period. We refer to these averages as annual averages or 8-year averages, respectively, when discussing the 800-m model in the text.

3. Results and Discussion

3.1. The Importance of the LB

The surface area of LB covers approximately one fifth of the Nordic Seas but is responsible for approximately one third of the total buoyancy loss in the region (Richards & Straneo, 2015). In the western part of the LB, Bosse et al. (2018) estimated a temperature decrease in AW by about 2.6 °C on its way northward, a more rapid cooling than any other region in the Nordic Seas. Using hydrographic measurements, Raj et al. (2015) obtained winter MLDs of 560 m in the LB, one of the largest values in the Nordic Seas. This deep thermal convection together with large buoyancy losses to the atmosphere implies pooling of warm water in the LB.

In Table 1, we contrast the integrated properties in the three main basins, the LB, the Norwegian Basin, and the Greenland Basin, using the 4-km model outputs. The heat transports integrated over the closed basin volume is largest into the LB (Figure 2), verifying that the LB is the most important area for the northward-flowing AW. The surface heat loss averaged over the period 1997–2005 reveals that among the major basins in the Nordic Seas, the LB accounts for approximately two thirds of the surface heat loss. More heat is transported into the LB and the Norwegian Basin than lost at surface, while it is the opposite for the Greenland Basin. Similar imbalances were inferred from observations in Segtnan et al. (2011). The heat imbalances imply warming of the LB and the Norwegian Basin, whereas the imbalance in the Greenland Basin is not significantly different than zero. Annual averages of temperature, volume averaged in each basin, show a small increase in the LB and the Norwegian Basin associated with these imbalances, while the Greenland Basin stays at approximately the same temperature. Maximum MLD in the LB is large and

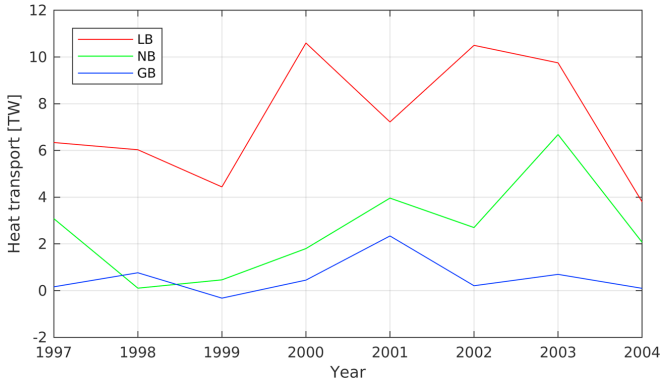

Figure 2. Integrated net heat transport for the Lofoten Basin (LB), Norwegian Basin (NB), and Greenland Basin (GB) for each year during the period 1 January 1997 to 1 January 2005. Time average values and standard deviations are given in Table 1.

comparable with the Greenland Basin (Table 1). While the Greenland Basin is recognized as a high-latitude deep and intermediate convection region (Rudels & Quadfasel, 1991), where brine rejection from sea ice formation can be important, the deep MLD in the LB is from thermal convection and cooling of the warm AW (Søiland & Rossby, 2013). In summary, the LB stands out in the Nordic Seas with large net heat transport and surface heat fluxes, giving deep MLDs.

3.2. Pathways

3.2.1. Observed Drifters

Drifter density maps are computed as the number of drifters entering defined rectangular bins in longitude and latitude. The so-called "density maps" show the distribution of drifters in the domain. In the density maps extracted from the observed drifter trajectories, the Slope Current stands out (Figure 3a) and dominates over the Front Current. Among the 149 drifters studied, 82 followed the pathway with the Slope Current, not interacting with the LB at all or passing by the southeastern rim of the LB. The observational data are biased, as a large number of drifters were deployed in the Svinøy section (black box in Figure 1b) and on the slope off the Lofoten-Vesterålen islands. However, we identified approximately 50 drifters deployed north or south of Iceland, 30 of which ended up to the east of the LB while 10 drifters propagated toward the western boundary of the LB. The remaining drifters stayed over the Helgeland Ridge (the topographic feature between the NB and LB) or entered the LB from south. Drifters deployed close to Iceland thus have a main route eastward toward the Svinøy section before turning north, in agreement with Orvik and Niiler (2002). In fact, we observed only four drifters that followed the Front Current along the Mohn Ridge northward toward Fram Strait.

The pathways of the drifters entering the LB are analyzed separately. The density of the trajectories of 46 drifters that entered the LB shows a broad entry region in the southern sector (Figure 3b).

In order to relate the residence time in the basin to the drifter entry and exit locations, we unwrap the LB contour and calculate the histograms binned in residence time and distance around the basin (Figure 4), that is, the percentage of drifters with a range of residence time entering (or exiting) at different segments around the LB contour is shown. The unwrapped LB contour starts from the northeastern corner (black cross in Figure 3c), progressing counterclockwise. The colored segments at the bottom of Figure 4 correspond to the same colored segments around the basin contour in Figure 3, starting with the red segment at 0 and following the basin counterclockwise to the end of the green segment at approximately 2,000 km.

A drifter can cross the LB boundary multiple times, giving more crossings for residence time analysis than the number of drifters we investigate. The drifters enter and exit the basin mainly in the south and east (Figures 4a and 4b). However, the majority of drifters experience short residence time inside the basin. We measure the residence time as the length of each stretch of record when a drifter was in the basin. The mean residence time inside the basin averaged over all drifter entries is 10 days. If we use the longest retention

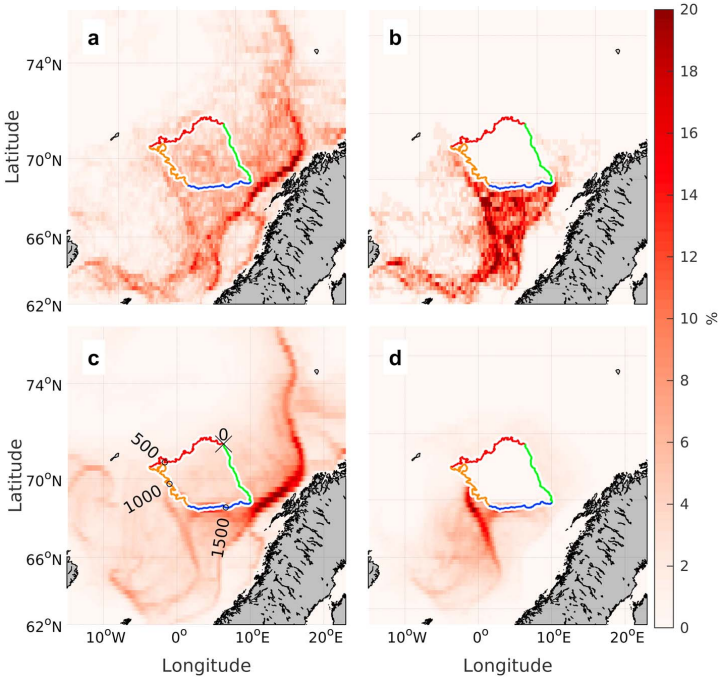

Figure 3. Density maps obtained from (a,b) the observed drifters and from (c,d) the synthetic drifters. Left panels show density maps of all drifters studied, 149 for (a) and 47,226 for (c). Right panels show density maps of drifters that interacted with the Lofoten Basin, 46 for (b) and 12,064 for (d). These are shown from deployment location until the first entry to the basin for each drifter. Color bar shows the percentage of drifters that was observed inside each bin relative to the number of drifters analyzed (listed above). Bin sizes are 0.25° × 0.25°. The white-bordered contour marks the Lofoten Basin with colors indicating the northern (red), western (orange), southern (blue), and the eastern (green) segments. For later reference, the basin contour in (c) is marked at 500-km intervals starting from the northeastern corner (black cross).

period for each drifter with multiple crossings of the basin perimeter, we obtain a mean residence time of 20 days. The hot spot for entering/exiting drifters in the southeast between 1,450 and 1,750 km accounts for approximately 40% of the drifter entries, but given their short residence time, the drifters exit before the associated water parcels are able to transfer heat to the basin. We observed seven drifters with at least one crossing into the LB with a residence time longer than 50 days (15% of the drifters that entered the LB). Their trajectories are shown in Figure 5b, together with the analogous trajectories for the drifters staying inside the basin between 15 and 50 days (12 drifters; Figure 5a).

The observed trajectories with longer residence time in the basin are not clearly linked with eddy shedding from the Slope Current. Figure 5a shows trajectories with orbital motion near and north of the steep slope between the Slope Current and the basin. These may be indicative of the eddy shedding from the unstable boundary current. Based on their relatively short residence times and the observation that they do not propagate far into the basin, their contribution to the large LB heat loss must be limited. The drifters with residence time longer than 50 days (Figure 5b) advect from south and enter the basin mainly across the southern and western segments of the LB. Observational evidence of contribution from the Slope Current into the basin is scarce. We observe one occurrence of a trajectory from slope to basin, but mainly the drifters either follow the Front Current to enter the basin in the southwest or enter the basin from south after crossing the Vøring Plateau. The drifters mainly propagate toward the basin with a meandering motion. Although the drifter observations are limited and inconclusive, they are indicative of the preferred locations of entry and exit

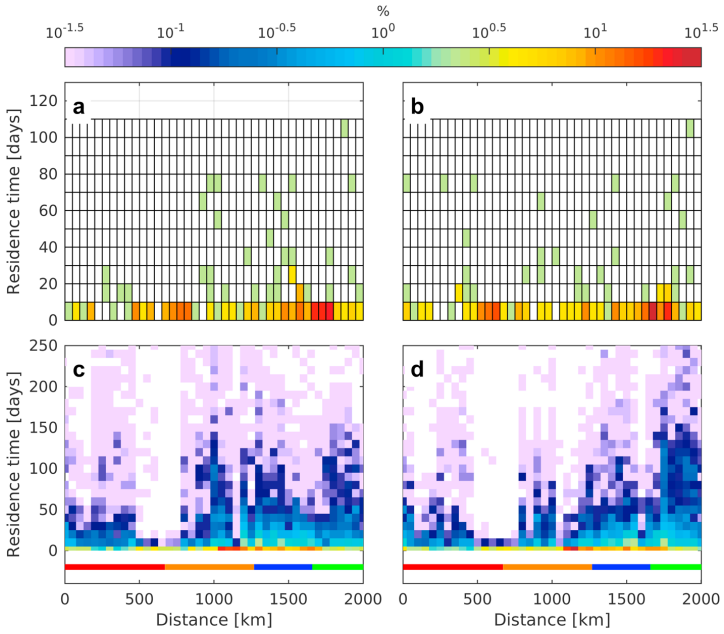

Figure 4. Histogram linking the drifter residence times inside the basin to (a,c) entry and (b,d) exit locations on the unwrapped LB contour for (a,b) observed and (c,d) synthetic drifters. Colored line at the bottom of (c) and (d) shows the unwrapped LB contour with the corresponding colors in Figure 3 for the north, west, south, and east segments. The percentage of entries/exits relative to the number of drifters interacting with the basin (46 for a and b and 12,064 for c and d) are color coded on logarithmic scale. Bins are 50 km × 10 days. Note that a drifter may cross the LB boundary several times. LB = Lofoten Basin.

into the LB and highlight the striking difference in pathways taken by the two subsets with short and long residence times in the LB. We turn to synthetic drifters to increase the statistical confidence in this finding.

3.2.2. Synthetic Drifters

The synthetic drifters obtained from the 4-km model fields were subjected to a data selection similar to that applied to the observed drifters (section 2.2), resulting in 59,112 synthetic surface drifter trajectories that were deployed south of the LB. We further removed 5,118 trajectories from drifters which ran aground before they reached the LB. Of the remaining drifters, 6,768 were deployed within the LB contour, while 12,064 were deployed outside but entered the LB at a later time. Thus, $12,064/(59,112 - 5,118 - 6,768) = 26\%$ of the drifters deployed outside the LB interacted with the basin. This is comparable to $46/149 = 31\%$ obtained for the observed drifters and suggests some confidence in the synthetic drifters. The smaller value may be because of the setup of the experiments: The synthetic drifters are deployed on a uniform grid (section 2.2) to obtain homogeneous statistics and to avoid spurious and biased representation of the flow because of geographical sampling variations (Davis, 1991), whereas the in situ drifters are deployed in key sections and locations.

The density plots of synthetic drifters (Figures 3c and 3d), subsampled similar to observations, show similarities with the observed drifter densities (Figures 3a and 3b). The Slope Current is pronounced, the drifters mainly approach from the south toward the southern LB boundary, and the Front Current densities are the strongest along the outer rim of the Vøring Plateau. The continuation toward the Mohn Ridge, however, is weak. Instead, the connection toward the Slope Current along the Vøring Plateau is stronger than previously thought.

Residence time analysis of these synthetic drifters can be compared to the observed drifters (Figure 4). In agreement with the observations, most synthetic drifters experience short periods inside the basin, and the

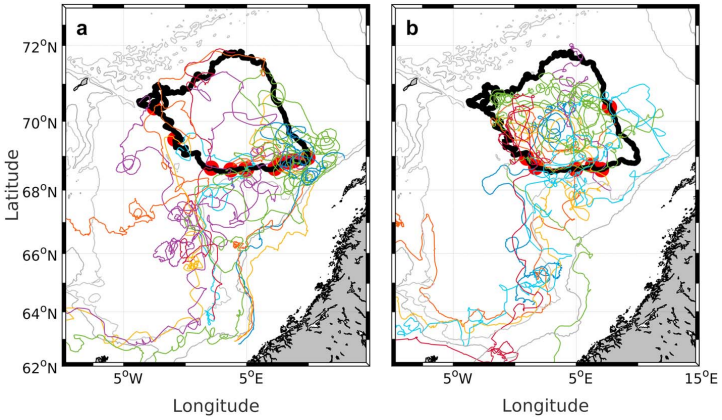

Figure 5. Drifter trajectories for (a) the 12 drifters staying inside the basin between 15 and 50 days and (b) for the seven drifters staying inside the basin for more than 50 days. The red dots mark the first entry position for each drifter into the basin. Only trajectories from deployment location until the last exit from the Lofoten Basin are shown. The 1,000- and 2,000-m isobaths are shown in gray.

associated heat loss must therefore be limited. The mean residence time for all entries into the basin is about 15 days, 5 days more than the observed drifters. The mean residence time for the longest consecutive period inside the basin for all drifters is 45 days, that is, a factor of two more than the observed drifters. The distribution of the retention periods for the synthetic drifters is highly skewed (not shown), relative to the observations (skewness of 2.2 vs. 1.6) with a longest residence time in the basin for the synthetic drifters of 363 days, 260 days longer than the observed drifters. Such long retention periods will not be captured by the observed drifters with much shorter lifetime because of mortality (from batteries and storms, section 2.1). The majority of the synthetic drifters (85%) has a longest residence time shorter than 103 days. The mean residence time of this set of synthetic drifters is 22 days, which is similar to the observations. Thus, the long residence time of synthetic drifters is mainly skewed by a small subset of drifters trapped in the LB. The synthetic drifters with a residence time longer than 50 days enter the basin mainly in the south/southwest or east (537 in north, 1,008 in west, 713 in south, and 739 in east). In the west, the entries are dominant along the southernmost part of the segment. The exit positions are mainly oriented toward the eastern part of the basin.

The large surface heat loss in the basin is expected to reduce the temperature of the synthetic drifters with prolonged periods in the basin. Using the temperature fields of the synthetic drifters, the temperature change between the entry and exit is analyzed. However, due to the seasonal cycle, the drifters can experience both warming (during summer, not shown) and cooling (during winter). Since the cooling is enhanced during winter, we focus on drifters entering the basin during these months and investigate how the temperature loss is related to residence time in the basin. We restrict the analysis to one single winter month (to reduce temporal variations due to seasonal changes). For the same reason, we do not study residence times longer than 100 days. The temperature loss is computed by calculating the difference $-(T_{\text{exit}} - T_{\text{entry}})$, between temperatures at the exit and entry times. November (3,386 crossings), December (2,742 crossings), and January (2,459 crossings) months are analyzed to test the sensitivity. Each subset shows a similar pattern and variability (not shown). We focus on November, because it has the most number of trajectories and it is followed by a long winter season (a residence time of 90 days experiences the entire winter). The cooling in winter is positively correlated ($r^2 = 0.34$) with the residence time (Figure 6a), likely facilitated by the retention induced by eddies, and shows approximately a linear increase with increasing residence time. Generally, strong winter surface heat losses in the basin can thereby impact transformation of water parcels with long residence time in the basin.

The temperature loss experienced by water parcels shows geographical variations related to the entry segments (Figure 6a). Synthetic drifters which entered the basin in November are subsampled into those with

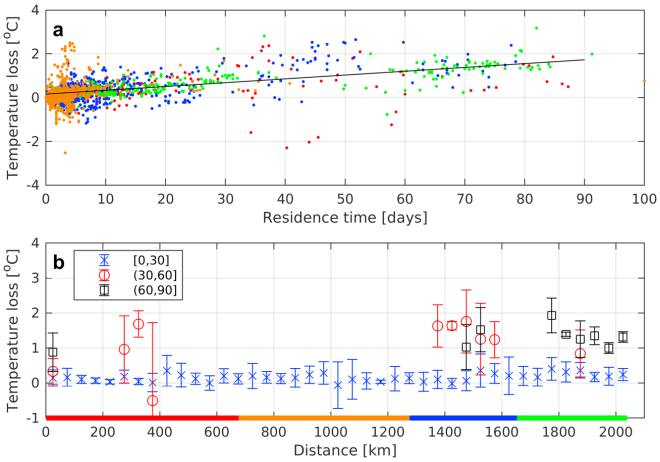

Figure 6. (a) Temperature loss variability with residence time for synthetic drifters entering the basin in November. The temperature loss is that experienced by a water parcel from entry to exit. Colored dots identify the segment of entry. A linear fit is also shown (squared linear correlation coefficient is $r^2 = 0.34$); (b) temperature loss versus entry position into the basin averaged in bin sizes of 50 km along the unwrapped basin contour. All temperature loss data of crossings from drifters going into the Lofoten Basin in the specified bin is averaged, and error bars are one standard deviation. Results are shown for drifters with a residence time between 0 and 30 days, between 30 and 60 days, and between 60 and 90 days. A bin with less than 3 data points is excluded. The colored line in the bottom marks the northern (red), western (orange), southern (blue), and the eastern (green) segments of the Lofoten Basin boundary.

residence time between 0 and 30 days, between 30 and 60 days, and between 60 and 90 days. We obtain 3,200, 96, and 88 crossings into the basin associated with these groups, respectively. The largest temperature losses, which are mainly experienced for water parcels with a residence time between 30 and 90 days, most frequently enter the basin in the south and east, indicating a large contribution to the LB heat loss from these regions (Figure 6b). Each data point is an average over all temperature data measured in horizontal bins of 50 km. An average is excluded if the number of data points inside a bin is less than 3. The averaged temperature loss taken over the southern and eastern segments were 1.4 and 0.9 °C, respectively, for drifters with residence time between 30 and 60 days and 1.3 and 1.4 ° C between 60 and 90 days. Even though the temperature losses are larger for drifters entering the basin in the south compared to east, both quantities are significant, and the synthetic drifters suggest that the heat transport across both the southern and the eastern boundaries of the LB is the largest contributors to the heat budget of the LB at surface.

3.3. Eulerian Analysis—The Role of Subsurface Processes

Using near-surface Lagrangian trajectory analysis of observed drifters, we showed that the AW enters the LB across a broad sector in the south. The water parcels associated with this flow experience the longest residence times in the basin, hence the largest heat loss in winter. Synthetic surface drifters additionally show a contribution from the east, which is supported by the earlier literature (Isachsen et al., 2012; Köhl, 2007; Raj et al., 2016). Overall, the percentage of drifters that interact with the LB (31% for the observed and 26% for the synthetic drifters) is significant but implies that a larger percentage of drifters propagates along the slope and around the rim of the basin and does not enter the LB. Furthermore, the drifters entering the LB typically have short residence times, hence experience a limited heat loss. The Slope Current carries the majority of drifters. This suggests that eddies from the Slope Current may be subsurface lenses instead of surface intensified eddies (Rossby, Prater, & Søiland, 2009), facilitating a substantial deeper interaction between AW and the LB (Rossby, Ozhigin, et al., 2009). Vertical motion might occur in certain regions due to deep MLDs. The (2-D) surface drifters will remain at surface and cannot sink, hence cannot capture the subsurface exchange. With the Eulerian fields, however, we can investigate the vertical distribution of heat fluxes and quantify the different contributions to the LB heat budget along the basin contour and in the water column.

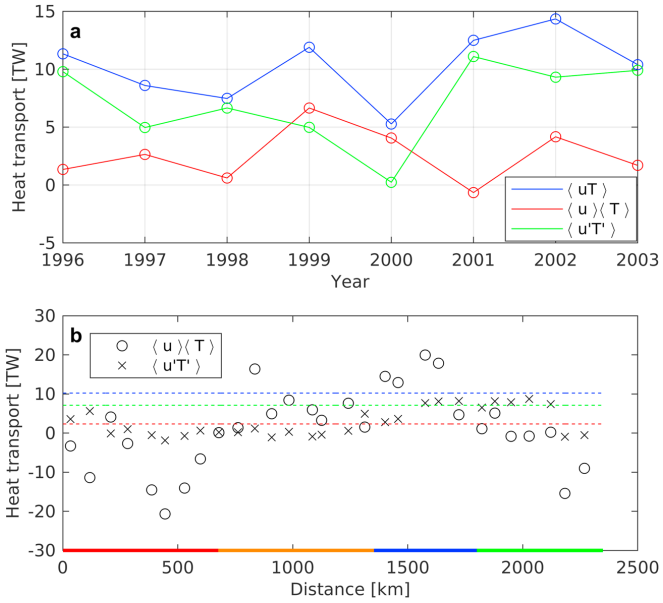

Figure 7. (a) Annual-averaged integrated heat transport around the LB for each year during the period 1 January 1996 to 1 January 2004. Total heat transport is shown in blue, while the mean heat transport and the eddy transport are shown in red/green, respectively; (b) time-averaged heat transport over 8 years from 1 January 1996 to 1 January 2004 along the unwrapped LB contour. Dashed lines are the 8-year averaged net heat transports into the basin. The colors correspond to the total, the mean, and the eddy contribution and are the same as in (a). Red, orange, blue, and green lines at the bottom identify segments of the unwrapped LB contour. LB = Lofoten Basin.

We use the eddy-resolving 800-m resolution ROMS model to investigate the net heat transport into the LB and quantify the mean and eddy contributions. As a comparison, the surface EKE averaged over the basin and over time between 1 January 1996 and 1 January 2004 is 330 cm^2/s^2, about 5 times larger than the corresponding number from the 4-km model (Table 1). The volume transport into the LB is balanced as in the 4-km model. Heat transport is computed by integrating around the closed LB contour over the entire water column, as in the 4-km model (equation (1)). Applying Reynolds averaging (equation (2)), we split the integral into a mean and an eddy component. In practice, we obtain the eddy flux, $\langle u' T' \rangle$, as the residual of the total heat transport (equation (1)) and the mean heat flux $\langle u \rangle \langle T \rangle$ (here only expressed for u), where averaging is over 1 year, after following the procedure described in the end of section 2.3. Annual total heat transports from the 800-m model (Figure 7a) are 1 to 5 TW (1 TW = 10^{12} W) larger than the LB heat transport calculations from the 4-km model (Figure 2). The 8-year average of approximately 10 TW can be compared to the ocean heat convergence of 119 TW computed by Segtnan et al. (2011) but over an area about 10 times larger than our LB area. Integrated around this closed volume, the net heat transport is mainly dominated by eddy fluxes.

We wish to describe the variability of the mean and eddy fluxes in the vertical, in the curtain of water column around the basin contour. This, however, needs to ensure the net volume transport over the averaging length is zero. In order to identify the locations along the basin contour where the eddy fluxes and the mean flow make the largest contributions to the increase of heat content inside the LB, we estimate the net heat transport through defined segment lengths of the basin contour by the following procedure. Starting from the northeast edge of the LB contour, as earlier, we integrate the volume transport first over the entire depth and then counterclockwise along the LB contour over a segment length, until the net volume transport becomes smaller than a set threshold. Below this threshold, set to 0.02 Sv, we consider the volume transport to be balanced. We integrate the heat transport over depth and along this segment and assign the result to the midpoint of the defined segment along the basin contour. This procedure is repeated by moving 2 km

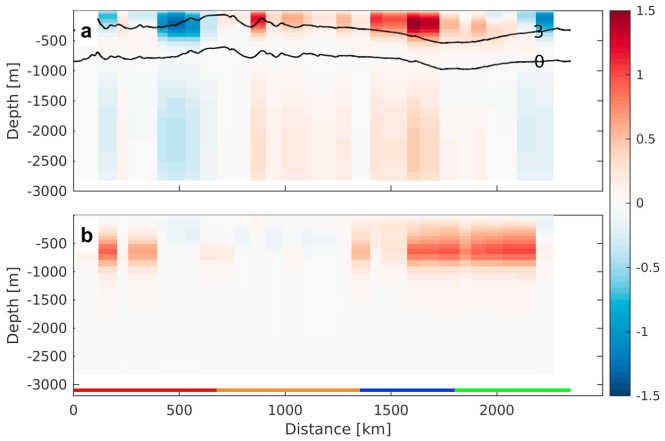

Figure 8. Vertical distribution of layer-integrated heat transport along segments with balanced volume transport for the (a) mean flow and for the (b) eddy fluxes, averaged in 80-km bins. The time averaging is similar to Figure 7b. Color bars show the heat transport in TW. Red, orange, blue, and green lines at the bottom identify the segments of the unwrapped Lofoten Basin contour. In (a), the black curves show temperature contours for 0 and 3 °C along the basin boundary.

counterclockwise along the basin contour and integrating along a new segment with balanced volume transport. The heat transports are then averaged in 80-km bins along the basin contour.

Alternatively, if one uses the volume average temperature in the LB as the reference temperature, heat transport can be calculated using arbitrary segment lengths without the requirement of zero net volume transport (Lee et al., 2004). However, the heat transport may be sensitive to the choice of the segment length. Constraining the segment lengths with zero net volume transport has the advantage that it defines the segments around the basin contour.

For this calculation, we time average between 1 January 1996 to 1 January 2004 (section 2.3). We require a minimum segment length of 200 km. The average segment length with balanced volume transport is 940 km, approximately two fifths of the length of the basin contour. We assume that the large amount of segments obtained, 1,413 in total, will be representative of where the heat fluxes enter the basin. Distribution of the time-averaged heat fluxes along the LB contour highlights where the mean or the eddy components dominate (Figure 7b). The depth-integrated heat transport indicates substantial heat into the basin as a mean flow in the southern sector (1,400–1,600 km) and of comparable magnitude transported out of the basin in the north (400–600 km). As expected, the heat associated with eddy fluxes are important in the east/northeast.

The vertical distribution of heat transport in the water column along the LB contour is calculated over the same segments with balanced volumed transport, but vertical integration is over each layer instead of the entire depth (Figure 8). The time averaging is similar to Figure 7b. The contributions of the mean flow and the eddy fluxes are presented separately. The mean flow advecting heat to the LB from the south (blue segment, 1,300–1,700 km) appears to be a near-surface feature, while the eddy fluxes supplying heat into the basin from the southeast/east/northeast are centered at approximately 700-m depth.

The heat transport, integrated around the basin and the entire depth (Figure 7a), is dominated by eddy fluxes in agreement with the earlier literature (Isachsen, 2015; Köhl, 2007; Koszalka et al., 2011). Along the LB contour, the mean heat flux shows a large variability (Figures 7b and 8) and give the largest contribution to heat input to the LB in the west and south, while the eddy fluxes dominate in the east and north. The large heat input to the LB in the south (Figures 7b and 8a) is supported by the surface drifters which showed a slab-like advective inflow to the LB in this region. These drifters entering from the south experience long residence time and significant temperature loss in the basin. Thus, the heat input in the south computed from the model is likely to contribute to the surface heat loss in the basin. Between about 600- and 800-m depth, the heat flux associated with the mean flow vanishes where the temperature of the inflow is approximately zero. At the same levels, the eddy fluxes dominate. The eddy fluxes supply heat to the LB deeper

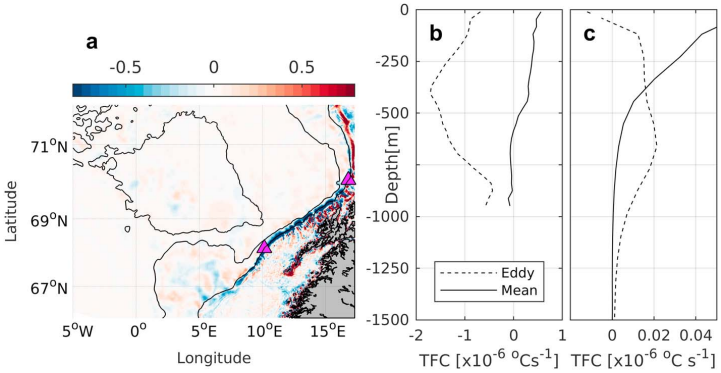

Figure 9. (a) Eddy temperature flux convergence (TFC) averaged over depth. The 1,000- and 2,000-m isobaths together with the Lofoten Basin are shown in black. Color bar shows the TFC in $10^{-6}\times$ °C/s. Triangles on the 1,000-m isobath define the segment over which the vertical profiles of mean and eddy fluxes shown in (b) are averaged. Average profiles of eddy and mean TFC are calculated over (b) the 1,000-m isobath off the Lofoten Escarpment and (c) the Lofoten Basin. Note we only show the upper 1,500 m in (c) as the fluxes vanish deeper in the water column. The time averaging is done for the period 1 January 1996 to 1 January 2004 (similar to Figures 7b and 8) for all panels.

in the water column at approximately 700 m and are not captured by surface drifters, possibly explaining why only 5% (6%) of the observed (synthetic) surface drifters stayed inside the LB more than 50 days. This is consistent with the observations of Poulain et al. (1996) and with Rossby, Prater, and Søiland (2009) who discussed the different behavior of surface drifters and RAFOS floats and found that the fraction of RAFOS floats ejected from the Slope Current toward the LB was larger than for the surface drifters. The findings are also consistent with Volkov et al. (2013) who reported differences between the eddy propagation pattern in the LB (westward and cyclonic propagation) affected by the deep currents and surface drifter trajectories. The heat from eddy fluxes between 500- and 1,000-m depth are therefore likely to give large contributions to the LB heat budget.

The results in Figures 7b and 8 are not based on closed integrals and must be interpreted with caution regarding the net heat transport. Also, they do not reveal information about the residence time in the basin. However, both the advective flux in the upper layers in the south and the eddy fluxes around 700-m depth in the east are supported by Lagrangian studies. Water parcels bringing heat into the basin at these locations also interact significantly with the basin and contribute to the heat loss. The mean heat fluxes centered around 1,500 km that advect about 1.5 TW heat into the basin are larger than the eddy fluxes of ∼1 TW at 700-m depth. Since the eddy fluxes are important to close the LB heat budget (Isachsen, 2015; Isachsen et al., 2012; Köhl, 2007; Richards & Straneo, 2015; Spall, 2010; Volkov et al., 2015), our estimate of the mean heat flux from the south implies a substantial advective heat contribution.

An analysis of the temperature flux convergence (TFC) supports the inferences from the mean and eddy fluxes discussed above. We compute the negative of divergence such that a positive value indicates convergence of temperature, that is, heating, as $-\nabla\cdot\langle\mathbf{u}'T'\rangle$ (i.e., the eddy TFC) and $-\langle\mathbf{u}\rangle\cdot\nabla\langle T\rangle$ (i.e., the mean TFC), using the 8-year average from 1 January 1996 to 1 January 2004. The second expression assumes a nondivergent horizontal flow analogous to Isachsen et al. (2012). Note the temperature fluxes computed in Figures 7 and 8 consist of both rotational and divergent components. The heat budget of the basin is governed by the divergent heat flux; hence, the rotational component should be separated. This difficult task is alleviated by analyzing the heat flux divergences, since the rotational component vanishes (Isachsen et al., 2012). Figure 9a shows the depth-averaged eddy TFC distribution in the domain, with elevated values over the Lofoten Escarpment. Along the Slope Current, there is a persistent divergence of eddy fluxes along the 1,000-m isobath (blue colors in Figure 9a). A segment along the Lofoten Escarpment, along the 1,000-m isobath marked between the triangles in Figure 9a, is analyzed in detail. Averages of the mean and eddy TFC are computed along this segment for each depth level, to obtain the vertical distribution (Figure 9b). A similar calculation is also made over the LB (Figure 9c).

The vertical profiles show a divergence of eddy fluxes along the Lofoten Escarpment (Figure 9b), indicating heat extracted by the eddies shed from the 1,000-m isobath. The divergence has a maximum around a depth of 400 m. Furthermore, the eddy flux divergences dominate the convergence of the mean flow, implying the importance of the cooling of the Slope Current by eddy fluxes in this region, which may become a heat source for warming of colder water offshore, also possibly deep into the LB. This is supported by the vertical profiles obtained inside the central LB contour (Figure 9c). Even though the magnitudes are smaller than at the slope, the eddy fluxes show convergence around a depth of 700 m. This is consistent with Figure 8b and suggests that the eddies shed off the Slope Current to some extent propagate into the LB. Furthermore, the convergence of fluxes associated with the mean flow is larger than the convergence of eddy fluxes and dominates near the surface. This is consistent with the drifter observations and implies that the contribution of the slab of AW advection from the southern sector is important for the LB heat budget.

4. Conclusions

Compared to the Greenland Basin and the Norwegian Basin, the LB stands out with 3 to 12 times larger volume-integrated net heat transport and 3 to 6 times larger surface heat loss. The main contributors to the LB heat budget are the mean advective heat flow from the AW along the southern LB sector and the eddy fluxes from the Lofoten Escarpment in the east.

Our main findings are (1) the contribution of near-surface heat transport by the mean flow entering the LB from south is of significant importance; (2) the heat transport from the Lofoten Escarpment is dominated by eddy fluxes and enters the LB from the east; and (3) the eddy temperature flux divergence has a subsurface maximum that is not captured by the surface drifters.

The southeastern corner of the LB is an entry hot spot for surface drifters. However, most of these drifters stay inside the basin for a short period, and hence, the associated heat loss is limited. Drifters with long residence time inside the basin enter from south and, to some extent, from east. The Eulerian and Lagrangian analyses both suggest that eddies propagate westward into the LB. A comparison of vertical profiles of eddy TFCs from the slope region and from the central basin supports this link. The eddy fluxes cool the mean slope current, a process dominated at subsurface, and act as a heat source in the central basin. The heat transport by the mean flow enters the basin from the south in the upper water column and averaged over the central LB, the convergence of temperature fluxes associated with the mean flow is the largest at surface. This is consistent with our analyses of observed and synthetic surface drifters which revealed that these water masses often experience long residence time inside the basin to contribute substantially to the LB heat loss.

The subsurface processes are important in controlling the heat fluxes and the TFC, both in the basin and over the slope. Detailed subsurface Lagrangian observations are needed. Because of the deep mixed layer in the LB, the water parcels can experience a vertical exchange in addition to the lateral exchange. 3-D Lagrangian trajectories, computed from eddy-resolving numerical simulations as presented here but with better vertical and time resolution and realistic vertical velocity fields, could identify pathway of water parcels in the water column and merit further studies.

Acknowledgments
This study received funding from the Research Council of Norway, through the project *Water mass transformation processes and vortex dynamics in the Lofoten Basin in the Norwegian Sea (PROVOLO)*, project 250784. The surface drifters used in this study are obtained from the Global Drifter Program (http://www.aoml.noaa.gov/phod/gdp/index.php). The model and drifter simulations were performed on resources provided by UNINETT Sigma2—the National Infrastructure for High Performance Computing and Data Storage in Norway. The 4-km ROMS model fields and the synthetic drifters are archived, open-access, at the Norstore research data archive (https://archive.norstore.no/). The 800-m ROMS model fields are available at the Thredds Service at the Norwegian Meteorological Institute (https://thredds.met.no/). The authors thank Inga Koszalka and Pål Erik Isachsen for their help and support, Jonathan Lilly for discussions, and two anonymous reviewers and the editor Laurie Padman for their suggestions and comments which helped to improve the manuscript.

References

Andersson, M., Orvik, K. A., Lacasce, J. H., Koszalka, I., & Mauritzen, C. (2011). Variability of the Norwegian Atlantic Current and associated eddy field from surface drifters. *Journal of Geophysical Research*, *116*, C08032. https://doi.org/10.1029/2011JC007078

Bosse, A., Fer, I., Søiland, H., & Rossby, T. (2018). Atlantic water transformation along its poleward pathway across the Nordic Seas. *Journal of Geophysical Research: Oceans*, *123*, 6428–6448. https://doi.org/10.1029/2018JC014147

Davis, R. E. (1991). Observing the general circulation with floats. *Deep Sea Research Part A. Oceanographic Research Papers*, *38*, S531–S571. https://doi.org/10.1016/S0198-0149(12)80023-9

Fer, I., Bosse, A., Ferron, B., & Bouruet-Aubertot, P. (2018). The dissipation of kinetic energy in the Lofoten Basin Eddy. *Journal of Physical Oceanography*, *48*, 1299–1316. https://doi.org/10.1175/JPO-D-17-0244.1

Haidvogel, D. B., Arango, H., Budgell, W. P., Cornuelle, B. D., Curchitser, E., Di Lorenzo, E., et al. (2008). Ocean forecasting in terrain-following coordinates: Formulation and skill assessment of the Regional Ocean Modeling System. *Journal of Computational Physics*, *227*(7), 3595–3624. https://doi.org/10.1016/j.jcp.2007.06.016

Isachsen, P. E. (2015). Baroclinic instability and the mesoscale eddy field aorund the Lofoten Basin. *Journal of Geophysical Research: Oceans*, *120*, 2884–2903. https://doi.org/10.1002/2014JC010448-

Isachsen, P. E., Koszalka, I., & Lacasce, J. H. (2012). Observed and modeled surface eddy heat fluxes in the eastern Nordic Seas. *Journal of Geophysical Research*, *117*, C08020. https://doi.org/10.1029/2012JC007935

Isachsen, P. E., LaCasce, J. H., Mauritzen, C., & Häkkinen, S. (2003). Wind-driven variability of the large-scale recirculating flow in the Nordic Seas and Arctic Ocean. *Journal of Physical Oceanography*, *33*(12), 2534–2550. https://doi.org/10.1175/1520-0485(2003)033<2534:WVOTLR>2.0.CO;2

Ivanov, V., & Korablev, A. A. (1995). Formation and regeneration of the pycnocline lens in the Norwegian Sea. *Russian Meteorology and Hydrology*, *9*(9), 62–69.
Köhl, A. (2007). Generation and stability of a quasi-permanent vortex in the Lofoten Basin. *Journal of Physical Oceanography*, *37*(11), 2637–2651. https://doi.org/10.1175/2007JPO3694.1
Koszalka, I., LaCasce, J. H., Andersson, M., Orvik, K. A., & Mauritzen, C. (2011). Surface circulation in the Nordic Seas from clustered drifters. *Deep-Sea Research Part I: Oceanographic Research Papers*, *58*(4), 468–485. https://doi.org/10.1016/j.dsr.2011.01.007
Koszalka, I., LaCasce, J. H., & Mauritzen, C. (2012). In pursuit of anomalies—Analyzing the poleward transport of Atlantic Water with surface drifters. *Deep-Sea Research Part II: Topical Studies in Oceanography*, *85*, 96–108. https://doi.org/10.1016/j.dsr2.2012.07.035
Laurindo, L. C., Mariano, A. J., & Lumpkin, R. (2017). An improved near-surface velocity climatology for the global ocean from drifter observations. *Deep-Sea Research Part I: Oceanographic Research Papers*, *124*, 73–92. https://doi.org/10.1016/j.dsr.2017.04.009
Lee, T., Fukumori, I., & Tang, B. (2004). Notes and correspondence temperature advection: Internal versus external processes. *Journal of Physical Oceanography*, *34*, 1936–1944.
Lumpkin, R., Grodsky, S. A., Centurioni, L., Rio, M. H., Carton, J. A., & Lee, D. (2013). Removing spurious low-frequency variability in drifter velocities. *Journal of Atmospheric and Oceanic Technology*, *30*(2), 353–360. https://doi.org/10.1175/JTECH-D-12-00139.1
Lumpkin, R., Maximenko, N., & Pazos, M. (2012). Evaluating where and why drifters die. *Journal of Atmospheric and Oceanic Technology*, *29*(2), 300–308. https://doi.org/10.1175/JTECH-D-11-00100.1
Lumpkin, R., & Pazos, M. (2007). Measuring surface currents with Surface Velocity Program drifters: The instrument, its data, and some recent results. In *Lagrangian analysis and prediction of coastal and ocean dynamics* (pp. 39–67). Cambridge: Cambridge University Press. https://doi.org/10.1017/CBO9780511535901.003
MacLachlan, C., Arribas, A., Peterson, K. A., Maidens, A., Fereday, D., Scaife, A. A., et al. (2015). Global Seasonal forecast system version 5 (GloSea5): A high-resolution seasonal forecast system. *Quarterly Journal of the Royal Meteorological Society*, *141*(689), 1072–1084.
Nilsen, J. E. Ø., & Falck, E. (2006). Progress in oceanography variations of mixed layer properties in the Norwegian Sea for the period 1948–1999. *Progress in Oceanography*, *70*, 58–90. https://doi.org/10.1016/j.pocean.2006.03.014
Nøst, O. A., & Isachsen, P. (2003). The large-scale time-mean ocean circulation in the Nordic Seas and Arctic Ocean estimated from simplified dynamics. *Journal of Marine Research*, *61*(2), 175–210. https://doi.org/10.1357/002224003322005069
Orvik, K. A., & Niiler, P. (2002). Major pathways of Atlantic water in the northern North Atlantic and Nordic Seas toward Arctic. *Geophysical Research Letters*, *29*(19), 1896. https://doi.org/10.1029/2002GL015002
Peralta-Ferriz, C., & Woodgate, R. A. (2015). Seasonal and interannual variability of pan-Arctic surface mixed layer properties from 1979 to 2012 from hydrographic data, and the dominance of stratification for multiyear mixed layer depth shoaling. *Progress in Oceanography*, *134*, 19–53. https://doi.org/10.1016/j.pocean.2014.12.005
Poulain, P. M., Warn-Varnas, a., & Niiler, P. P. (1996). Near-surface circulation of the Nordic seas as measured by Lagrangian drifters. *Journal of Geophysical Research*, *101*, 18,237–18,258. https://doi.org/10.1029/96JC00506
Raj, R. P., Chafik, L., Nilsen, J. E. Ø., Eldevik, T., & Halo, I. (2015). The Lofoten Vortex of the Nordic Seas. *Deep-Sea Research Part I: Oceanographic Research Papers*, *96*, 1–14. https://doi.org/10.1016/j.dsr.2014.10.011
Raj, R., Johannesen, J., Eldevik, T., Nilsen, J., & Halo, I. (2016). Quantifying mesoscale eddies in the Lofoten Basin. *Journal of Geophysical Research: Oceans*, *121*, 4503–4521. https://doi.org/10.1002/2016JC011637
Richards, C. G., & Straneo, F. (2015). Observations of water mass transformation and eddies in the Lofoten Basin of the Nordic Seas. *Journal of Physical Oceanography*, *45*(6), 1735–1756. https://doi.org/10.1175/JPO-D-14-0238.1
Rossby, T., Ozhigin, V., Ivshin, V., & Bacon, S. (2009). An isopycnal view of the Nordic Seas hydrography with focus on properties of the Lofoten Basin. *Deep-Sea Research Part I: Oceanographic Research Papers*, *56*(11), 1955–1971. https://doi.org/10.1016/j.dsr.2009.07.005
Rossby, T., Prater, M. D., & Søiland, H. (2009). Pathways of inflow and dispersion of warm waters in the Nordic seas. *Journal of Geophysical Research*, *114*, C04011. https://doi.org/10.1029/2008JC005073
Rudels, B., & Quadfasel, D. (1991). Convection and deep water formation in the Arctic Ocean-Greenland Sea System. *Journal of Marine Systems*, *2*(3-4), 435–450. https://doi.org/10.1016/0924-7963(91)90045-V
Segtnan, O. H., Furevik, T., & Jenkins, A. D. (2011). Heat and freshwater budgets of the Nordic seas computed from atmospheric reanalysis and ocean observations. *Journal of Geophysical Research*, *116*, C11003. https://doi.org/10.1029/2011JC006939
Shchepetkin, A. F., & McWilliams, J. C. (2005). The Regional Oceanic Modeling System (ROMS): A split-explicit, free-surface, topography-following-coordinate oceanic model. *Ocean Modelling*, *9*(4), 347–404. https://doi.org/10.1016/j.ocemod.2004.08.002
Shchepetkin, A. F., & McWilliams, J. C. (2009). Correction and commentary for "Ocean forecasting in terrain-following coordinates: Formulation and skill assessment of the regional ocean modeling system" by Haidvogel et al., J. Comp. Phys. 227, pp. 3595-3624. *Journal of Computational Physics*, *228*(24), 8985–9000. https://doi.org/10.1016/j.jcp.2009.09.002
Søiland, H., & Rossby, T. (2013). On the structure of the Lofoten Basin eddy. *Journal of Geophysical Research: Oceans*, *118*, 4201–4212. https://doi.org/10.1002/jgrc.20301
Spall, M. A. (2010). Dynamics of downwelling in an eddy-resolving convective basin. *Journal of Physical Oceanography*, *40*(10), 2341–2347. https://doi.org/10.1175/2010JPO4465.1
Toole, J. M., Timmermans, M. L., Perovich, D. K., Krishfield, R. A., Proshutinsky, A., & Richter-Menge, J. A. (2010). Influences of the ocean surface mixed layer and thermohaline stratification on Arctic Sea ice in the central Canada Basin. *Journal of Geophysical Research*, *115*, C10018. https://doi.org/10.1029/2009JC005660
Trodahl, M., & Isachsen, P. E. (2018). Topographic influence on baroclinic instability and the mesoscale eddy field in the northern north atlantic ocean and the nordic seas. *Journal of Physical Oceanography*, *48*(11), 2593–2607. https://doi.org/10.1175/JPO-D-17-0220.1
Umlauf, L., & Burchard, H. (2003). A generic length-scale equation for geophysical turbulence models. *Journal of Marine Research*, *61*(2), 235–265.
Uppala, S. M., Kållberg, P. W., Simmons, A. J., Andrae, U., Bechtold, V. D. C., Fiorino, M., et al. (2005). The ERA-40 Re-analysis. *Quarterly Journal of the Royal Meteorological Society*, *131*(612), 2961–3012.
Volkov, D. L., Belonenko, T. V., & Foux, V. R. (2013). Puzzling over the dynamics of the Lofoten Basin—A sub-Arctic hot spot of ocean variability. *Geophysical Research Letters*, *40*, 738–743. https://doi.org/10.1002/grl.50126
Volkov, D. L., Kubryakov, A. A., & Lumpkin, R. (2015). Formation and variability of the Lofoten basin vortex in a high-resolution ocean model. *Deep-Sea Research Part I: Oceanographic Research Papers*, *105*, 142–157. https://doi.org/10.1016/j.dsr.2015.09.001
Warner, J. C., Sherwood, C. R., Arango, H. G., & Signell, R. P. (2005). Performance of four turbulence closure models implemented using a generic length scale method. *Ocean Modelling*, *8*(1-2), 81–113.
Yu, L. S., Bosse, A., Fer, I., Orvik, K. A., Bruvik, E. M., Hessevik, I., & Kvalsund, K. (2017). The Lofoten Basin eddy: Three years of evolution as observed by Seagliders. *Journal of Geophysical Research: Oceans*, *122*, 6814–6834. https://doi.org/10.1002/2017JC012982

Paper II

Vertical Structure and Seasonal Variability of the Inflow to the Lofoten Basin Inferred From High-Resolution Lagrangian Simulations

J.S. Dugstad, I.M. Koszalka, P.E. Isachsen, K.F. Dagestad, I. Fer
Journal of Geophysical Research - Oceans, **124** (2019)

JGR Oceans

RESEARCH ARTICLE
10.1029/2019JC015474

Vertical Structure and Seasonal Variability of the Inflow to the Lofoten Basin Inferred From High-Resolution Lagrangian Simulations

Johannes S. Dugstad[1], Inga Monika Koszalka[2,3], Pål Erik Isachsen[4,5], Knut-Frode Dagestad[6], and Ilker Fer[1]

[1]Geophysical Institute, University of Bergen and Bjerknes Centre for Climate Research, Bergen, Norway, [2]Department of Meteorology, Stockholm University and the Stockholm University Baltic Sea Centre, Stockholm, Sweden, [3]Bolin Centre for Climate Research, Stockholm, Sweden, [4]Department of Geosciences, University of Oslo, Oslo, Norway, [5]Norwegian Meteorological Institute, Oslo, Norway, [6]Norwegian Meteorological Institute, Bergen, Norway

Key Points:
- The Atlantic Water inflow to the Lofoten Basin is concentrated in two main regions, the Lofoten Slope Inflow and the Helgeland Inflow
- Three-dimensional Lagrangian simulations are crucial to detect seasonal variations in the vertical structure and temperature changes of the inflows
- Water masses that are cooled in the Lofoten Basin mainly enter from the south at the surface and from the continental slope at depth

Correspondence to:
J. S. Dugstad,
jdu019@uib.no

Citation:
Dugstad, J. S., Koszalka, I. M., Isachsen, P. E., Dagestad, K.-F., & Fer, I. (2019). Vertical structure and seasonal variability of the inflow to the Lofoten Basin inferred from high-resolution Lagrangian simulations. *Journal of Geophysical Research: Oceans*, *124*, 9384–9403. https://doi.org/10.1029/2019JC015474

Received 11 JUL 2019
Accepted 4 NOV 2019
Accepted article online 13 NOV 2019
Published online 19DEC 2019

Abstract The Lofoten Basin in the eastern Nordic Seas plays a central role in modifying the warm Atlantic Water inflow toward the Arctic Ocean. Here, the Atlantic Water experiences increased residence times, cooling, and substantial transformation. In this study, we investigate the Atlantic Water inflow pathways to the Lofoten Basin and their vertical and seasonal variations using 2-D and 3-D Lagrangian simulations forced by a high-resolution ocean model. Atlantic Water enters the basin from all directions, but we find two main inflow pathways at all vertical levels, one close to the Lofoten Escarpment in the southeast, associated with the Slope Current, and another close to the Helgeland Ridge in the southwest, associated with the Front Current. The surface inflow exhibits a stronger seasonal forcing than the inflow at depth as well as a stronger heat loss that is dominated by water masses entering the basin from the south. At deeper levels, the warm inflow from the east cools, while the relatively colder inflow from the west warms. The 2-D and 3-D synthetic trajectories show similar pathways. However, they are affected differently by the seasonal signal, giving different heat exchange patterns. Our results have implications for how results from Lagrangian observations in the region should be interpreted.

Plain Language Summary The Lofoten Basin in the Nordic Seas is of fundamental importance for the modification of the warm northward flowing Atlantic Water. Much of the ocean heat is lost to the atmosphere in this region. This is maintained by warm water inflows from regions around. Here, we study these inflows, their vertical structure, seasonal variability, and contribution to the heat budget in the basin. We apply an ocean model to advect purposefully released particles in the Nordic Seas seeded at 15-, 200-, and 500-m depth and study their pathways and fates. We analyze both a horizontal 2-D (particles are fixed at depth) and a full 3-D (particles can move in the vertical) simulation and compare the two. We find that the water masses mainly enter the Lofoten Basin in two regions, one in the southeast and one in the southwest. However, the vertical structure reveals that water that is cooled enter the basin via different routes at the surface than at deeper levels. The seasonal variations are also larger at surface than at depth. The 2-D and 3-D simulations show overall similar patterns, but the 3-D simulation reveals larger seasonal variations than the 2-D simulation.

1. Introduction

The Lofoten Basin (LB) in the Norwegian Sea is recognized as a region for the retention and modification of the warm and saline Atlantic Water (AW) carried by the Norwegian Atlantic Current (NwAC) northward toward the Arctic Ocean (Koszalka et al., 2011; Mauritzen, 1996; Rossby et al., 2009). As the AW enters the Nordic Seas (a joint name for the Greenland, Iceland, and Norwegian Seas), the NwAC splits into two branches, the Slope Current and the Front Current embracing the LB to the east along the upper Norwegian continental slope and to the west along the Helgeland-Mohn Ridges, respectively (Orvik & Niiler, 2002; see also Figure 1a). The relatively warm AW spreads between the branches and experiences increased residence times in the basin (Rossby et al., 2009). Large surface heat and buoyancy loss in winter result in cooling (Isachsen, 2015; Rossby et al., 2009; Richards & Straneo, 2015), and the modified water masses sink and form a warm anomaly at depth, compensated by their high salinity (Bosse et al., 2018; Segtnan et al., 2011). The

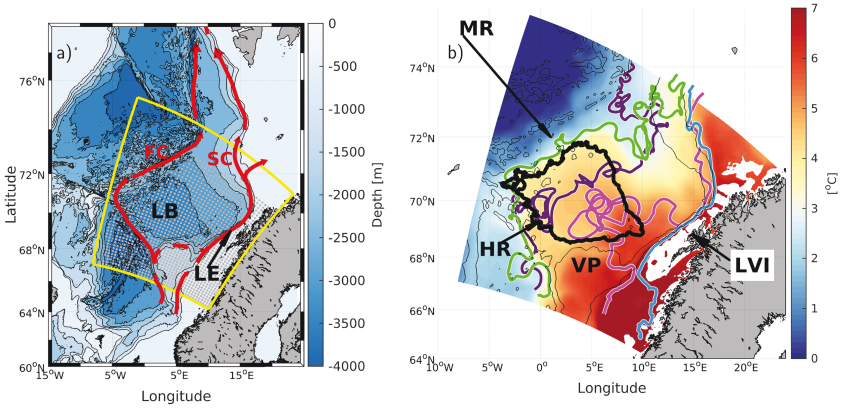

Figure 1. (a): Bathymetry map of the Nordic Seas showing the main pathways of the northward flowing Atlantic Water (red, the Slope Current, SC, and the Front Current, FC), the study domain (yellow) of the ROMS model used for the OpenDrift simulations, and the deployment grid for the synthetic drifters (gray dots). (b) ROMS model Eulerian temperature field at 200-m depth averaged over a period of 1996–1999. Superimposed are selected trajectories of 3-D synthetic drifters deployed at 200 m, illustrating pathways of the SC, (blue trajectory), FC (green trajectory), and the inflow to the LB via the Lofoten Slope Inflow (magenta) and the Helgeland Inflow (purple). Abbreviations are: LB = Lofoten Basin, LE = Lofoten Escarpment, HR = Helgeland Ridge, MR = Mohn Ridge, VP = Vøring Plateau, LVI = Lofoten-Vesterålen Islands, FC = Front Current, and SC = Slope Current.

AW extends vertically to a mean depth of 500–600 m and a maximum depth of approximately 800 m (Bosse et al., 2018; Mauritzen, 1996) (see also Figure 1b). Quantifying and understanding processes that modify the AW en route to the Arctic are important with implications for the regional climate and marine ecosystems (Årthun et al., 2018; Kovacs et al., 2011; Ogawa et al., 2018), as well as impacts on the Arctic sea ice cover (Årthun et al., 2019).

Quantifying the spatial distribution and temporal variability of mass and heat exchanges between the AW inflow and the LB is not a trivial task, as complex transient and mesoscale (10–100 km) processes contribute with large eddy heat fluxes (Isachsen et al., 2012; Spall, 2010). Several studies have pointed to the role of mesoscale eddies shed from the Slope Current off the Lofoten Escarpment and advected westward to the LB (Isachsen et al., 2012; Isachsen, 2015; Köhl, 2007; Raj et al., 2016; Volkov et al., 2015). This view is consistent with enhanced eddy kinetic energy densities and horizontal diffusivities in the eastern part of the LB as inferred from surface drifter data (Andersson et al., 2011; Koszalka et al., 2011). Subsurface acoustic RAFOS float trajectories have also shown eddy variability in this region (Rossby et al., 2009).

Analyses of hydrographic observations (Ivanov & Korablev, 1995) and model studies (Köhl, 2007; Volkov et al., 2013) have suggested that anticyclonic eddies from the Slope Current follow a cyclonic path toward the center of the LB. Volkov et al. (2013) also suggested that this cyclonic pattern is more pronounced in deeper levels (1,000–1,500 m). Furthermore, using subsurface RAFOS float observations, Rossby et al. (2009) showed that the flow at 200-m depth is strongly topographically steered. A large fraction of the RAFOS floats followed the Slope Current and entered the LB from east, trapped in eddies shed from the slope. However, analyses of surface drifters by Koszalka et al. (2013) and Dugstad et al. (2019) have suggested that the warm AW spreads and enters the LB from the south as a broad slab between the two NwAC branches, thus indicating a different pattern at the surface. In particular, the latter study found that the surface drifters with long residence time inside the basin enter along the southern part of the LB , mainly across the northern rim of the Vøring Plateau. In an attempt to partition the contribution of advective heat transport into the LB in their eddy-permitting model, Dugstad et al. (2019) found that the heat transport by the mean flow was important in upper layers along the southern sector of the basin, while the eddy heat fluxes from the Lofoten Escarpment in the east were enhanced at depths between 300 and 600 m. While the above studies suggest that both the mean flow and eddy fluxes contribute to the heat budget of the LB, the main routes

and vertical structure of the AW inflow to the basin, the associated heat exchange, and the temporal aspect of these exchanges remain poorly known.

We address these questions by analyzing trajectories from Lagrangian simulations driven by outputs from a 800-m horizontal resolution ocean model of the region. We investigate the main inflow routes, describe their vertical structure and seasonal variability, and estimate how this affects the AW-LB heat exchange. We analyze two Lagrangian simulations, one with only 2-D horizontal advection (similar to the motion of surface drifters and RAFOS floats) and one that also allows vertical advection (3-D), and compare the two. Deployments at three vertical levels (15, 200, and 500 m) are used to quantify the vertical structure of the AW-LB exchange. Our study thus complements Dugstad et al. (2019) who addressed the subsurface AW-LB exchange within the Eulerian framework only. Using the Lagrangian framework, we are able to study the pathways and fates of a particular water mass, namely, AW, as it enters and passes through the LB.

2. Data and Methods

2.1. Ocean Model

We integrate Lagrangian trajectories using the output from a high-resolution Regional Ocean Modeling System (ROMS) configuration for the eastern Nordic Seas. ROMS is a hydrostatic primitive equation model defined on a staggered C-grid and terrain-following vertical coordinates (Haidvogel et al., 2008; Shchepetkin & McWilliams, 2005, 2009). A fourth-order-centered scheme is used for vertical advection and a third-order upwind scheme for horizontal tracer and momentum advection. No explicit horizontal eddy viscosity or diffusion is applied but the upwind advection scheme exhibits implicit numerical diffusion. Unresolved vertical mixing processes are parameterized using the k-ϵ version of the General Length Scale scheme (Umlauf & Burchard, 2003; Warner et al., 2005). The skill of this scheme in representing vertical convection is satisfactory (Warner et al., 2005), and its effect on our results and interpretation is discussed in section 4.3. The open lateral boundaries are relaxed toward monthly fields from the Global Forecast Ocean Assimilation Model (MacLachlan et al., 2015), and the atmospheric forcing is provided by 6-hourly fields from the ERA-Interim atmospheric reanalysis (Dee et al., 2011). The model has 800-m horizontal resolution and 60 vertical layers with enhanced resolution near the surface (thickness varying from 2 to 5 m at surface toward 60 to 70 m toward the bottom). Model output (currents and hydrography) is stored every 6 hr for the period of 1996–1999. With this spatial and temporal resolution the model resolves mesoscale and even some submesocale processes (Isachsen, 2015; Trodahl & Isachsen, 2018) and thus captures the circulation features that dominate lateral stirring processes.

2.2. Lagrangian Simulations

For Lagrangian simulations, we employ OpenDrift (Dagestad et al., 2018), an open source Python-based framework for Lagrangian modeling, which operates off-line, that is, using a stored model velocity output. OpenDrift includes modules to simulate drift of various substances and objects such as oil, search and rescue, and plankton (Dagestad & Röhrs, 2019; Jones et al., 2016; Kvile et al., 2018). In this study, however, we follow the movement of water particles, using the most basic OpenDrift module for passive tracers advected solely with ocean currents. We will refer to the Lagrangian simulations as "synthetic drifters" to distinguish them from real surface drifter observations used for comparison (section 2.3). Two experiments of synthetic drifters are performed, using either only the horizontal velocity (2-D experiments) or the full three-dimensional velocity field (3-D experiments). Lagrangian positions are updated using the 6-hourly model currents by applying a fourth-order Runge-Kutta integration routine. Trajectories, that is, time series of Lagrangian positions (longitude, latitude, and depth) are stored with 6-hr intervals. ROMS potential temperature, salinity, and velocity outputs are linearly interpolated on the particle trajectories. We do not apply explicit lateral or vertical diffusion to avoid making trajectories too diffusive with respect to transport properties of the ROMS model solution used to force them. The question of adding additional diffusive term to compensate for the missed variability in off-line Lagrangian simulation has been a subject of a discussion but is usually avoided in studies using high-resolution model outputted at high frequency; see for example, Bower et al. (2011), Gelderloos et al. (2017), Rühs et al. (2019), and in our previous study, Dugstad et al. (2019), as well as van Sebille et al. (2018) and Wagner et al. (2019) and references herein. We will come back to this point in section 4.

The synthetic drifters are deployed at three levels, 15, 200, and 500 m (typical anchoring levels for surface drifters and RAFOS floats, respectively, and reaching down to the base of the AW in the Nordic Seas), and uniformly over the horizontal domain (marked in Figure 1a) in sets of 40×40 drifters (about 20-km spacing

Table 1
Statistics for the Entry Into the LB and Residence Time for Synthetic Drifters (2-D and 3-D Lagrangian Experiments)

			Lofoten Basin Drifters		Residence time [days]	
	Depth [m]	Total	all	outside [%]	all entries (LSI) (HI)	longest stay (LSI) (HI)
2D						
	15	164,013	99,588	60,432 [48]	10 (8) (13)	29 (19) (37)
	200	171,566	100,977	61,841 [47]	12 (10) (14)	39 (28) (44)
	500	143,455	92,759	53,603 [51]	16 (14) (19)	56 (47) (62)
3D						
	15	163,456	100,886	61,730 [49]	11 (10) (14)	35 (25) (43)
	200	164,227	102,304	63,148 [50]	13 (11) (15)	42 (32) (48)
	500	143,891	92,209	53,053 [51]	17 (14) (22)	59 (43) (76)

Note. Total: the total number of synthetic drifters considered in the analysis (see section 2.2). Lofoten Basin Drifters: the number of synthetic drifters interacting with the LB, both given by *all* drifters (both those deployed in the LB and those entering from outside) and the ones only entering the basin from *outside* (all minus the 39,156 drifters deployed in the LB). The percentage of drifters entering from outside, calculated as $\frac{outside}{Total-39{,}156} * 100$, is given in brackets. Residence time, all entries: the mean residence time for all synthetic drifter entries in the LB. Residence time, longest stay: the mean residence time for the longest stay in the basin (see section 3.2). The residence times in parentheses are given for drifters entering the basin across the LSI and HI segments, respectively.

between the deployments). The sets of 1,600 drifters are deployed every week from 1 January 1996 to 1 January 1999, giving 156 weeks of deployments (1,600∗156 = 249,600 drifters in total at each seeding depth). Each synthetic drifter is given a lifetime of 1 year. We disregard the deployments over shelf areas shallower than 200 m, which reduces the number of trajectories to 225,000 at 15 and 200 m and 195,000 at 500 m, and we apply absorbing boundary conditions that cause drifters that run over a shelf region shallower than 200 m or hit the open-ocean boundary of the model to be terminated. We also exclude from the analysis drifters that are deployed north of the northernmost part of the LB contour (26,988 drifters for each level, 2-D and 3-D), and about 15% of the total that are deployed in a cyclonic rim circulation of the Norwegian Sea to the south and recirculating southward and never reaching the LB.

The total number of analyzed synthetic drifters, for each vertical level and experiment, is given in Table 1. Furthermore, since we focus on the inflow to the LB, we will in most cases consider only the drifters entering the LB from outside (Table 1). As in Dugstad et al. (2019), we define the LB by the 3,000-m isobath (see highlighted black contour in Figure 1a). This contour is closed except in the southwest corner where the Helgeland Ridge opens toward the Norwegian Basin. We manually closed this 28-km-long segment.

2.3. Relative Dispersion of Real and Synthetic Drifters

To evaluate the velocity field in the model, we compare the Lagrangian trajectories deployed at 15-m depth to actual surface drifter observations using dispersion statistics. Surface drifter data from the eastern Nordic Seas (15–20° E, 62–75° N) were downloaded from the Global Drifter Programme database (https://www.aoml.noaa.gov/phod/gdp/ updated through 30 June 2018 at the time of download on 19 January 2019). The drifter positions (longitude, latitude) were quality controlled and interpolated via a kriging method to 6-hr intervals by the AOML/NOAA Drifter Data Assembly Center (Lumpkin & Pazos, 2007). This type of drifter consists of a surface buoy, with a transmitter and a temperature sensor and a subsurface drogue at 15-m depth. The drifter has a tether strain sensor for monitoring the presence of the drogue. Only trajectory segments with the drogue attached were used. The largest contribution to the total of 370 drifters came from the POLEWARD experiment under the International Polar Year (2007–2009) whereby 150 drifters were deployed at the Svinøy site (63° N), near the islands of Gimsøy, Bjørnøya, in the Barents Sea, and in the LB (Koszalka et al., 2009). Most of the POLEWARD drifters were deployed in pairs and triplets yielding nearly 100 drifter pairs. A smaller deployment (10 drifters) was also carried out during the ProVoLo experiment.

We evaluate the Lagrangian simulations by comparing the 2-D synthetic drifters deployed at 15-m depth with the observed surface drifters anchored at 15-m depth, using a relative dispersion statistics. The relative dispersion quantifies the spreading of nearby drifters due to spatial differences in the velocity field and can be regarded as a proxy for Eulerian wave number kinetic energy spectra (Koszalka et al., 2009; LaCasce, 2008). As in Koszalka et al. (2009) we consider chance pairs (drifters that came close together at any instant

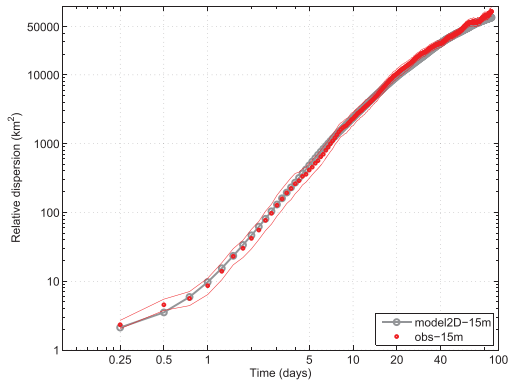

Figure 2. Ensemble-mean relative dispersion as a function of time for the observed surface drifters and for the 2-D synthetic drifters deployed and advected at anchoring depth of the surface drifters (15 m). The 95% confidence intervals for the observed relative dispersion are shown with red thin lines.

of time, not necessarily deployed together) and close separations (less than 2 km) . In addition, to avoid the drifter pair velocities that are correlated at the starting point of the analysis, we search pairs at 1-day intervals. This yields 461 chance pairs for the observed surface drifters (reduced by half after 100 days). For the synthetic trajectories, due to their larger number, we find pairs at 30-day intervals yielding over 200,000 pairs for the total duration of the experiment. This large number of drifters allows a statistical comparison.

The ensemble-mean relative dispersion of the synthetic and observed drifters is shown in Figure 2. The synthetic drifters reproduce the relative dispersion of the surface drifters very well. Both the initial exponential regime during the first 2 days and the Richardson regime at 2–10 days (Koszalka et al., 2009) are captured. This means that the near-surface turbulent transport processes including stirring by eddies and mean current shear are statistically well represented by the ROMS model output forcing the Lagrangian simulations. Unfortunately, a small number of the available RAFOS floats (∼20) in the eastern Nordic Seas prohibits a similar statistical evaluation at deeper levels.

3. Results

3.1. General Circulation Features

We first focus on the general circulation at 200 m, which is representative for the AW inflow in the eastern Nordic Seas, as the flows in this region are relatively weakly stratified and to a large extent steered by topography.

Figure 1a shows a schematic of mean currents superimposed on a bathymetric map, and Figure 1b shows the model domain and the model's time-averaged temperature field at 200 m carrying a signature of the warm AW filling the LB. Superimposed are four selected synthetic Lagrangian trajectories from the 3-D deployment at 200-m depth that illustrate main circulation features discussed in the text: the northward flowing Slope Current (blue) and Front Current (green) and two main inflow pathways to the LB from the east and west, given in magenta and purple colors, respectively (the inflows will be further discussed below). Similar circulation patterns are also identified in the 2-D synthetic drifters deployed at 200 m (not shown), and they are also evident in trajectories of the observed RAFOS floats ballasted at ∼250-m depth (Rossby et al., 2009).

3.2. Main Inflow Pathways and Residence Times in the LB

In order to visualize the main inflows to the LB, we plot "drifter density maps." These are obtained by counting occurrences of individual synthetic drifters in a grid of longitude-latitude bins and normalizing by the total number of drifters entering the LB. Figure 3 shows such maps to indicate pathways of drifters before LB entry, using drifters deployed at 15 and 500 m. Since a drifter can cross the LB contour several times, we consider trajectory segments from deployment until the entry of the longest period of stay in the basin. (When a drifter crosses the basin contour multiple times, it experiences several periods in the basin. One of the periods must be longer than the other ones. We refer to this as the longest period of stay, or simply the "longest stay.") Because the LB is located at high latitudes (around 70° N), the longitude bins are scaled by a factor $1/\cos(70°)$ relative to the latitude bins. Thus, we choose bin sizes of $0.73° \times 0.25°$. Only density maps from the 3-D simulation are shown in Figure 3, but the ones derived from 2-D simulations are similar. There are drifters entering the LB from all sides, but two major inflow regions stand out: the "Lofoten Slope Inflow" (LSI) to the southeast, close to the continental slope, and the "Helgeland Inflow" (HI) to the southwest, approximately where the 3,000-m contour does not close. These two inflow regions are marked with cyan segments in the figure. The importance of the LSI and HI is quantified by counting the number of drifters that entered the basin (for their longest stay) across these segments. The segment lengths amount to 16% (LSI) and 18% (HI) of the total LB contour length, but the percentage of drifters with a longest stay entry across these segments is larger. In the 3-D simulations LSI accounts for 24–25% of the drifters at all three levels, whereas for the HI the percentage of drifters increases from 17% at 15 m to 25% at 500 m. Results from the 2-D simulations agree to within 2%. This means that approximately 50% of the drifters

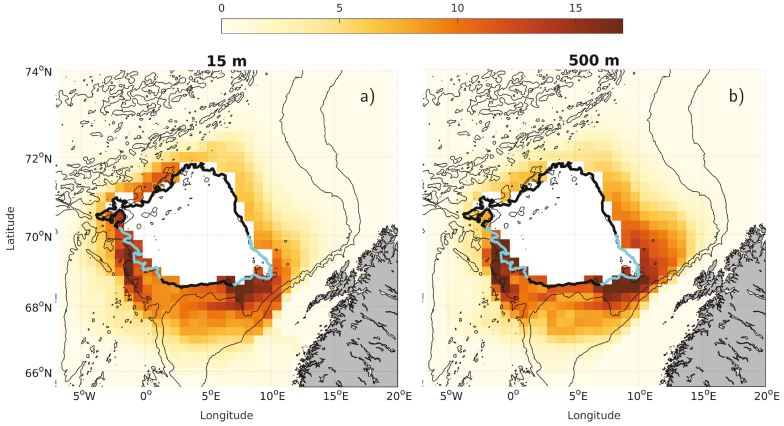

Figure 3. Density maps of 3-D synthetic drifters deployed at (a) 15 m and (b) 500-m depth entering the LB for their longest stay in the basin. Only segments from deployment until the longest stay entry are considered. The 1,000- and 2000-m isobaths are shown in black thin lines, and the 3,000-m isobath (thick black) defines the LB. The density maps show the occurrence percentage of drifters in a grid of longitude-latitude, relative to the number of drifters entering the basin for the respective deployment depth. The bin sizes are 0.73° × 0.25° (see section 3.2). Cyan segments show the LSI and HI segments along the LB contour.

enter the basin via the LSI and the HI segments combined, which is disproportionally large compared with the relative length of the segments. Hence, these inflows appear as key regions for the AW-LB exchange.

In general, the salient circulation features in the region are related to topography and thus appear similar in the 2-D and 3-D synthetic trajectories (Table 1). In both, the 2-D and 3-D simulations, similar percentages of synthetic drifters interact with the LB (~50%). The simulations also agree well in terms of residence times inside the LB. We report averages over two alternative residence times computed from the trajectories, the residence time of any entry to the basin (this can include short duration crossings of the basin contour) and the residence time of the longest stay. In both 2-D and 3-D simulations, the mean residence time for all entries is shortest for drifters deployed at 15 m (10 days) and longest for drifters deployed at 500 m (17 days). The same holds for the longest stay entries (30 and 60 days for drifters deployed at 15 and 500 m, respectively) indicating that the residence times increase with depth. If only sampling for the trajectories entering the LB across the LSI or HI segments (cyan segments in Figures 3a and 3b), the residence times also agree fairly well. The largest difference is seen for drifters deployed at 500-m depth and entering the LB via HI, where the longest stay residence time for the 3-D simulation is larger (76 vs. 62 days). The residence times are generally longer for the HI entries compared to the LSI entries (discussed in section 4.1).

Note that the synthetic drifters are integrated for only 1 year so the residence time statistics are likely underestimated with respect to an asymptotic case of infinite time or a multiyear integration; nevertheless, it is a useful diagnostic for the purpose of questions addressed in our work. The differences between the 2-D and 3-D simulations, their seasonal variation, and impact on heat exchange are further considered in sections 3.4–3.5.

3.3. Vertical Structure of the Inflow and Its Seasonal Variations in 3-D Lagrangian Simulations

Probability density functions (PDFs) of the depth of entry to the LB are calculated for the first entry and the longest stay entry using the 3-D synthetic drifters (Figure 4a). The PDF curves show that the majority of drifters enter the basin close to their deployment level, but they are skewed toward deeper levels, implying that more drifters have sunk relative to their deployment position.

To study the differences in vertical drifter movements, we calculate a monthly breakdown of the relative vertical displacement between the deployment position and the entry to the LB. Specifically, for each 3-D synthetic drifter with a longest stay entry in a given month, we compute its vertical displacement relative to its depth 30 days prior to entry (i.e., difference in depth at time of entry and 30 days earlier). The choice of a 30-day window was made to ensure a time span long enough to allow the drifters to be affected by

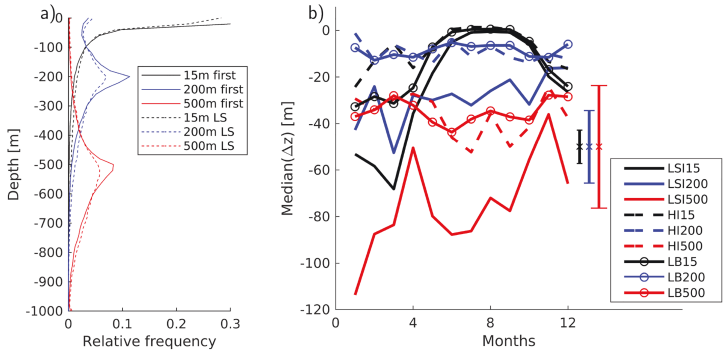

Figure 4. (a): Probability density functions (PDFs) of the entry depth into the LB for 3-D drifters for the first entry to the basin (solid) and the longest stay (LS, dashed); (b) seasonal median vertical displacements (negative = sinking) experienced by synthetic drifters between the day of their longest stay entry and 30 days earlier; for example, Month = 1 shows the median vertical displacement between the longest stay entry and 30 days before for drifters entering the basin in January. We show vertical displacements for drifters entering via the LSI (solid lines), HI (dashed lines), and the entire LB (solid lines with circles). Error bars for LSI15, LSI200, and LSI500 are also shown (see text). Error bars for other groups are similar. The LSI and HI are defined as the cyan-colored segments in Figures 3a and 3b.

different physical processes but also short enough as the time span should be shorter than the seasonal variability. A representative vertical displacement for the given month is obtained as the median value of all vertical displacements in that month (a negative vertical displacement indicates sinking). The ROMS vertical resolution gets coarser at depth. This imposes an inherent uncertainty in the vertical displacement in the Lagrangian simulations. We quantify this uncertainty using the model layer thickness (annual average) at the depth of the estimated median vertical displacement. The error bars increase with depth and are only shown for LSI for clarity (the geographical difference is not large).

The month-to-month calculations are done separately for the entries across the LSI and HI segments as well as for the entire basin contour as a comparison (Figure 4b). The drifter densities 30 days prior to the entries across LSI and HI, respectively, indicate that the drifters are concentrated around their respective entry regions (not shown). Thus, the drifters have not traveled from vastly different regions during this period; hence, they have not experienced particularly different physical processes, suggesting that our 30-day window is an appropriate choice. For all three categories, a seasonal signal is seen in surface layers (drifters deployed at 15 m) where winter months are characterized by a net sinking while summer months show drifter movements with negligible vertical displacement. Deep mixed layers in winter allow larger vertical displacements than a stratified water column in summer. The seasonal signal is also stronger for drifters entering via the LSI than via the HI or the basin as a whole, and the variations are strongest at the surface. At deeper levels (especially 500 m), the error bars are large, and the difference in vertical displacements is not statistically significant. But in general, Figure 4b implies a different vertical structure of the inflows in winter than in summer and that the net sinking is largest in the LSI region, indicating that waters entering here are the most buoyant and therefore most susceptible to cooling (with consequent sinking) in winter.

As the 3-D synthetic drifters are advected vertically, they enter the LB at various depths. Taking advantage of the spatially uniform deployment over the area, we further categorize the drifters based on the depth of the longest stay entry to the LB, independent of their initial deployment level. From the PDFs in Figure 4a, we find "break points" in drifter densities (where the various PDFs intersect) and use them to define three entry depth classes: (1) 0–130 m (62,355 drifters), (2) 130–370 m (51,915 drifters) and (3) 370 m to bottom (63,661 drifters). From this definition, a drifter that, for example, had its longest stay entry to the LB at 40-m depth would be defined to belong to Depth Class 1. The 3-D synthetic drifters in these three classes are further subdivided by which season they enter the LB (winter: January–March and summer: July–September).

As discussed above, the drifters experience sinking during winter, while during summer, the strong stratification restricts the drifters to float near their deployment level. This seasonal difference manifests itself as a smaller percentage of drifters being observed in Depth Class 1 during winter compared to summer, and

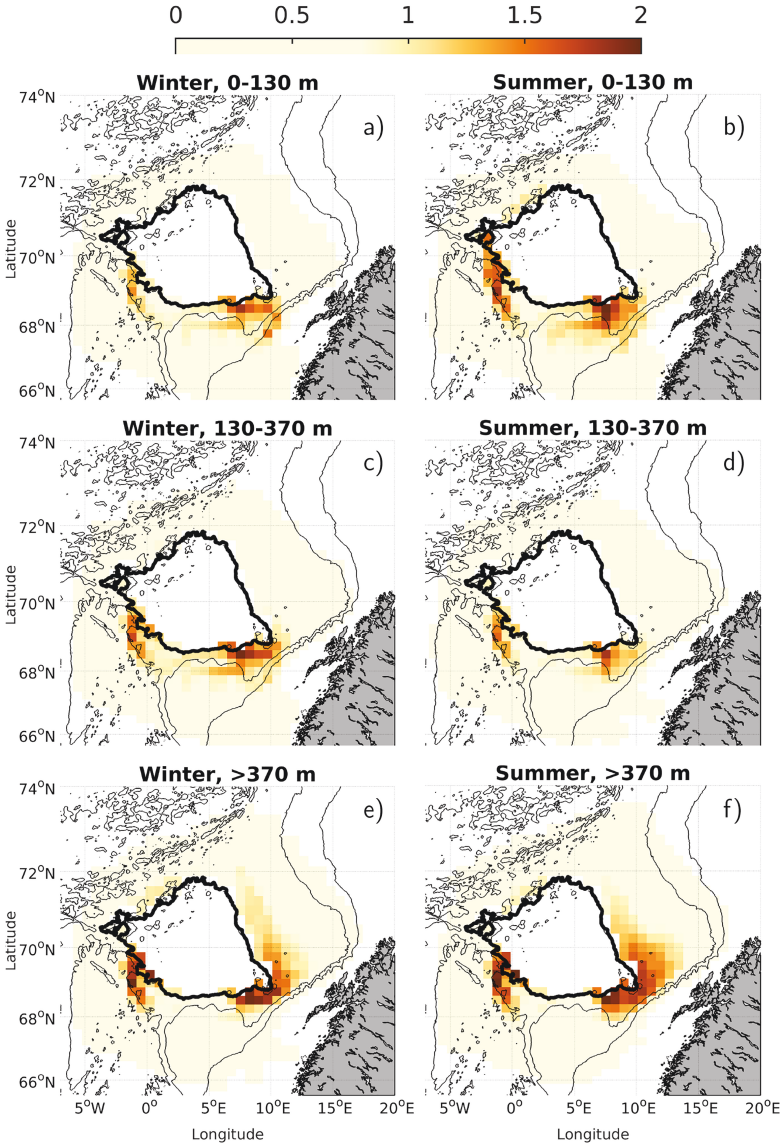

Figure 5. Density maps of 3-D synthetic drifters entering the LB in different seasons: (a, c, and e) Winter = January–March and (b, d, and f) Summer = July–September, and at different depths. Only trajectory segments from deployment until the longest stay entry are considered. The entry depth classes (see text) are 1:0–130 m (a,b), 2:130–370 m (c,d), 3:370–bottom (e,f). The color bar shows the percentage of drifters in a bin when normalized with the total number of drifters entering the basin summed over all depth classes (62,355 + 51,915 + 63,661 = 177,931). Bin sizes are as in Figure 3.

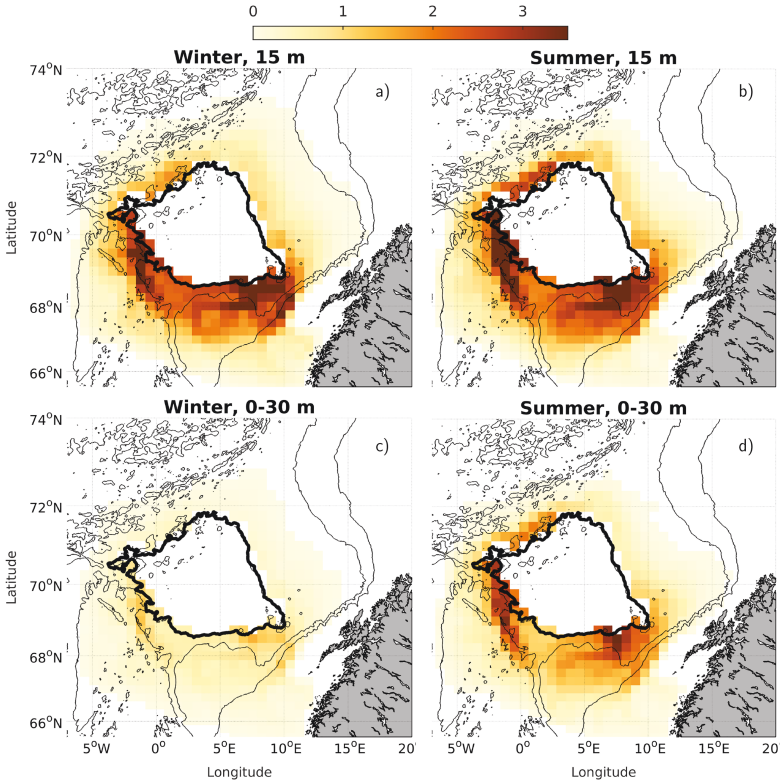

Figure 6. Density maps of (a and b) 2-D drifters at 15-m depth and (c and d) 3-D drifters deployed at 15 m entering the LB between 0- and 30-m depth in winter (January–March, left panels) and summer (July–September, right panels). Only trajectory segments from deployment until the longest stay entry are considered. Color bars show the percentage of drifters in a bin normalized with the total number of drifters entering the LB for the given deployment depth (2-D 15 m: 60,432; 3-D 15 m: 61,730). Bin sizes are as in Figure 3.

vice versa for Depth Class 2. Specifically, we estimate that among the drifters in Depth Class 1, about 28% enter the basin during summer and about 22% enter the basin during winter. Furthermore, we observe that during summer, the relative amount of drifters in Depth Class 1 that are deployed at 15 m is larger than during winter (82% vs. 62%). This is mainly because the drifters deployed at 15 m can sink in winter (to Depth Class 2) while they remain in Depth Class 1 during summer.

The density maps of drifters in the three depth classes (0–130 m, 130–370 m, and 370 m-bottom) are shown in Figure 5 for trajectory segments between deployment and the longest stay entry. The color bar indicates the percentage of drifters in a bin when normalized by the total number of drifters in all depth classes in order to better visualize the seasonal-vertical variations of the inflow to the LB. The seasonal behavior shows up in Figures 5a–5d as stronger colors (larger percentages) in panel b compared to panel a and also to some extent stronger colors in panel c compared to panel d. Note that the seasonal variability is stronger in Depth Class 1, nearby the surface where the atmospheric cooling/warming largely affects the stratification of the water column. For Depth Class 3, at depths below 370 m, (Figures 5e and 5f) the synthetic drifter densities and patterns show only weak seasonal variation.

Despite the seasonal variations in the density maps, the main inflow pathways toward the basin are similar. For Depth Classes 1 and 2 the LSI and HI are pronounced in both seasons. For Depth Class 3 we also observe these features, but in the east toward the continental slope, we also notice enhanced drifter densities around

Table 2
Percentages of Synthetic Drifters (2-D and 3-D Lagrangian Experiments) Classified According to the Temperature Loss in the LB During Their Longest Stay in the Basin

		1	2	3	4
	Depth/depth class	<−1 ° C [%]	−1–0 ° C [%]	0–1 ° C [%]	>1 ° C [%]
2-D					
	15 m	7	13	8	4
	200 m	5	15	13	2
	500 m	3	11	11	3
3-D					
	(0–130 m)	8	14	10	3
	(130–370 m)	2	14	12	1
	(370 m-bottom)	1	16	14	0

Note. Temperature Class 1 (drifters that experience more than 1 ° C cooling), Temperature Class 2 (between 0 and 1 ° C cooling), Temperature Class 3 (between 0 and 1 ° C warming), and Temperature Class 4 (more than 1 ° C warming). Listed are percentages of drifters deployed at 15-, 200-, and 500-m depths (2-D) and drifters belonging to Depth Classes 1, 2, and 3 (3-D) that belonged to the given temperature class. The percentages are computed by normalizing by the number of drifters entering the LB independent on deployment level/depth class (2-D: 60,432 + 61,841 + 53,603 = 175,884 drifters; 3-D: 62,355 + 51,915 + 63,661 = 177,931 drifters).

larger stretches of the basin boundary. We take this as indication of enhanced topographic steering of flow (and drifters) at depth.

3.4. Two-Dimensional Versus Three-Dimensional Lagrangian Trajectories

We assess the differences between the 2-D and 3-D simulations in terms of the near-surface circulation where the vertical displacements and seasonality are more pronounced (Figure 6). We show winter (left panels) and summer (right panels) density maps for the 2-D synthetic drifters at 15 m (top panels) and the 3-D synthetic drifters deployed at 15 m and entering the LB at the depth of 0–30 m (15 m ± 15 m, bottom panels). The maps reveal that the seasonality in drifter distributions is much more pronounced for the 3-D synthetic drifters than for the 2-D synthetic drifters. For instance, the percentage of 3-D drifters that enter the basin in winter versus summer between 0- and 30-m depth, when normalized to the amount of 3-D drifters deployed at 15 m that entered the LB (Table 1), is 8% and 20%, respectively. This strong seasonality is again coupled to the vertical structure of the inflow: During winter (panel c), the 3-D drifters have sunk below our defined depth range, and as a consequence, they have lower occurrence density than in summer (panel d), consistent with our interpretation of results shown in the previous section. For the 2-D drifters, the drifter densities in different seasons can only be affected by a change of pathways between summer and winter that would make the amount of drifters entering the basin at the given depth to change between the seasons. However, the drifter densities between winter and summer are similar (Figures 6a and 6b), and the two seasons account for approximately the same percentage of drifters entering the basin (winter: 24%, summer: 25%) when normalized against the amount of 2-D drifters entering the basin when deployed at 15 m (Table 1), indicating a strong difference between the 2-D and 3-D drifters.

A similar comparison of the 2-D and 3-D drifters deployed at 200- and 500-m depths (not shown) reveals seasonal differences, but with smaller amplitude at 200 m and hardly discernible at 500 m. This result is consistent with Figures 5e and 5f for Depth Class 3, indicating similar drifter densities and patterns in the two panels, implying that the seasonal variation in vertical displacement of the drifters is small when we integrate the drifter densities over the water column below 370-m depth.

3.5. Implications for Heat Exchange

As seen from Figure 5 and mentioned in section 3.3, the inflows to the LB preferentially come more from the slope at deeper levels compared to the surface. It is of interest to see whether this has an impact on the AW-LB heat exchange. As a proxy to quantify the heat exchange associated with the inflow, we study pathways toward the LB of synthetic drifters that experience a certain temperature change within the basin. We thereby assume that the temperature change occurs along the drifter trajectory (see section 4.3 for further discussion). Because several previous studies used 2-D surface drifters and RAFOS floats to study the heat

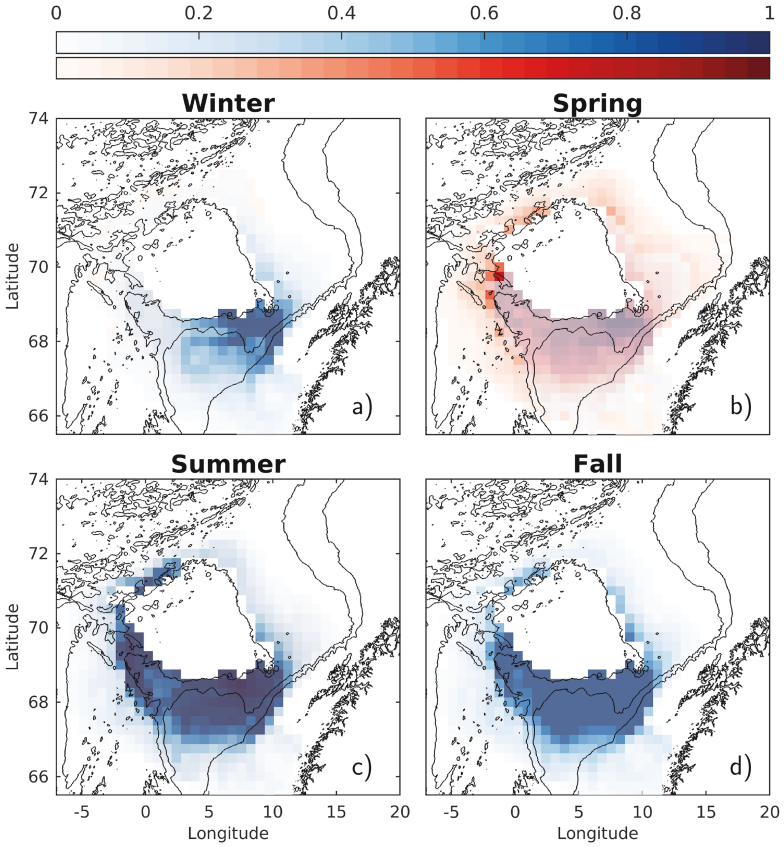

Figure 7. Drifter density maps of 3-D drifters in Depth Class 1 (0–130 m) that belonged to (blue colors) Temperature Class 1 (cooling more than 1 ° C in the LB) and (red colors) Temperature Class 4 (warming more than 1 ° C in the LB) subsampled by the season of the longest stay entry to the LB. Only trajectory segments from deployment until the longest stay entry are considered. Color bars show the percentage of drifters in each bin relative to the total number of 3-D drifters belonging to Depth Class 1 (62,355 drifters). Since the color maps can overlap, blue colors are mapped over red colors using 30% transparency. Bin sizes are as in Figure 3.

exchange (Dugstad et al., 2019; Isachsen et al., 2012; Koszalka et al., 2013; Rossby et al., 2009), we also investigate the differences between the 2-D Lagrangian simulations (synthetic drifters are fixed at their respective deployment depths) and 3-D Lagrangian simulations (where we apply the entry depth classes defined in section 3.3).

Similar to the analysis in Dugstad et al. (2019), we quantify the temperature change during the longest stay in the LB for each synthetic drifter by calculating the temperature change between the entry and the exit of this stay: $\Delta T = T_{exit} - T_{entry}$, where T_{exit} and T_{entry} are the synthetic drifter temperatures at the longest stay exit point and longest stay entry point, respectively. Because we require that a synthetic drifter exits the basin, trajectory segments that terminate their lifetime inside the basin are excluded from the analysis. Due to generally short residence times at the surface and slightly longer at deeper levels, this affects only a small percentage of trajectories that increases at deeper levels: for the 2-D drifters, 0% (15 m), 3% (200m), and 9% (500 m) and for the 3-D drifters, 1% (Depth Class 1), 4% (Depth Class 2), and 12% (Depth Class 3).

Based on ΔT, we define four temperature classes: (1) drifters that cooled by more than 1 ° C; (2) cooled by 0–1 ° C; (3) warmed by 0–1 ° C; and (4) warmed by more than 1 ° C. The percentages of drifters in

each temperature class normalized with respect to all drifters that entered the LB summed over deployment depths (2-D = 175,884 drifters) or depth classes (3-D = 177,931 drifters) are given in Table 2. Note that the percentages do not sum up to 100, because the drifters terminated in the basin were not taken into account. In general, for both 2-D and 3-D drifters more drifters are cooled in the basin than warmed, implying a net heat loss in the basin for the drifters that enter. About 54% (55%) of the 2-D (3-D) drifters experienced cooling in the basin and 41% (40%) of the 2-D (3-D) drifters experienced warming (the rest ended their lifetime in the basin). In Temperature Class 1 with largest temperature loss, water parcels associated with drifters deployed at 15-m depth give the largest contributions to the heat loss in the basin (Table 2). However, drifters at deeper levels also indicate significant contribution to the heat loss. We note that the relative amount of drifters in Temperature Class 1 is larger than the amount of drifters in Temperature Class 4 (possibly with the exception of drifters at the deepest levels), indicating a net temperature loss in the LB. This is consistent with a net surface heat loss in the basin of 5.2 TW that was estimated by Dugstad et al. (2019) from a ROMS model with 4-km grid resolution when averaged between 1997 and 2005. Surface heat fluxes were unfortunately not saved from our model runs, but the drifter results are consistent with direct estimates of the lateral heat transport into the LB. Using model velocity and temperature fields from January 1996 to January 2000, we found a net advective heat transport convergence of 12 TW in the basin. The gap between this result and the surface heat loss estimated by Dugstad et al. (2019) is likely due to the different model configurations (e.g., resolution) and that the averaging is done over different time periods.

We construct synthetic drifter density maps of Temperature Classes 1 and 4 divided in four seasons: January–March, April–June, July–September, and October–December. The density maps for 3-D drifters in Depth Class 1 from deployment until their longest stay entry are shown in Figure 7 (2-D drifters deployed at 15 m have very similar patterns and seasonal variations and are therefore not shown). Synthetic drifters that enter the basin during late summer and fall mainly cool (blue shades) while those entering in late spring (April–June) experience warming (red shades) in the basin where they spend the following summer months. Late winter entries also experience cooling, in particular from the LSI. In late summer and early winter, drifter entries along the entire southern LB boundary experience cooling. This is consistent with Dugstad et al. (2019), who showed that the surface water masses with the largest temperature decrease in the LB entered the LB as a slab from the south.

The results for the 2-D synthetic drifters deployed at 500 m (Figure 8) can be compared to the 3-D drifters in Depth Class 3 (depths larger than 370 m; Figure 9). Note that the relative contribution at these levels are larger for the 2-D drifters than the 3-D drifters (Table 2). Therefore, the color scale is different in Figures 8 and 9 (discussed further in section 4.2). The general pathways, without taking seasonality into consideration, are similar in the 2-D and 3-D simulations with a cooling pronounced for the entries from the east and warming for entries from the west. Unlike at the surface (cf. Figure 7), the drifter density associated with cooling along the southern boundary of the basin is less pronounced, and instead, the inflows from the LSI and HI regions appear more important: LSI for the cooling of the warm AW entering from the east and HI for the warming of the colder waters from the FC, especially for the 2-D drifters (Figure 8). Seasonal variations are more pronounced in the 3-D drifters (Figure 9). Notably, there are approximately two times more 3-D drifters in Temperature Class 1 (cooling) that enter the basin during winter (January–March) than the other seasons. In winter the drifters that are cooled enter the basin from all sides, implying that the associated water masses are affected by the atmospheric cooling regardless of their entry region. We also notice that the cooling at deeper levels is delayed compared to near the surface (Figure 7) where the drifters experienced intense cooling in July–December. Largest warming (strong red colors) is seen in spring (Figure 9b), likely related to atmospheric warming. Summer and fall patterns are similar and resemble those for the 2-D drifters showing the cooling from the LSI and warming from the HI.

4. Discussion

4.1. Effects of Dynamics and Residence Times in the Basin

Our analyses show that the drifters entered the LB via two main routes, the LSI and the HI. While we have primarily focused on the inflow to the LB, the dynamics inside the LB is also of importance for the modification of the water parcels entering the basin, particularly by affecting the residence times in the basin (Table 1). In Figure 10, we show density maps similar to Figure 5, but now for the full trajectories including the trajectory segments in the basin. Superimposed binned velocity fields estimated from the same drifter data show a large cyclonic circulation around the basin, consistent with Volkov et al. (2013). Many of the HI

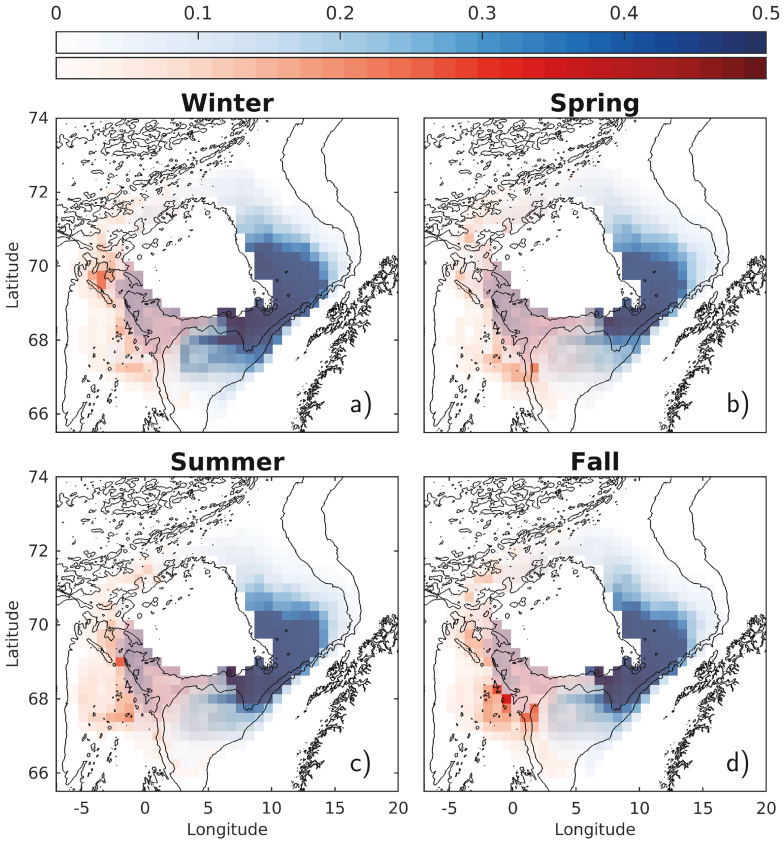

Figure 8. Drifter density maps of 2-D drifters deployed at 500-m depth that belonged to (blue colors) Temperature Class 1 (cooling more than 1 ° C in the LB) and (red colors) Temperature Class 4 (warming more than 1 ° C in the LB) subsampled by the season of the longest stay entry to the LB. Only trajectory segments from deployment until the longest stay entry to the basin are considered. Color bars show the percentage of drifters in each bin relative to the total number of 2-D drifters entering the LB when deployed at 500-m level (53,603 drifters). Since the color maps can overlap, blue colors are mapped over red colors using 30% transparency. Bin sizes are as in Figure 3.

drifters, that is drifters that entered the LB through the HI, follow this pattern and travel a comparatively long distance in the basin, which likely increases their residence times. As mentioned in section 3.2 the occurrence density of HI drifters increases with depth. Furthermore, since the residence times inside the basin are longer for HI drifters, this region appear to be an important route for the water that is warmed in the basin.

The percentages reported in section 3.2 indicated that the relative amount of drifters entering the LB via the LSI were almost constant with depth, but for the HI the relative amount of drifters increased from 17 to 25% for drifters deployed at 15 and 500 m, respectively. The HI is concentrated in the region where the LB contour do not close originally. Isachsen et al. (2003) and Nøst and Isachsen (2003) showed that the currents in the Nordic Seas follow the topography. Hence, as the 3,000-m isobath near the HI turns eastward and along the northern rim of the Vøring Plateau, the drifters could experience this topographical steering and veer eastward into the basin. The velocity vectors in Figure 10 support this. While the variability in wind and stratification would disturb topographical steering in upper layers (e.g., for deployments at 15- and 200-m depth), their influence diminish with depth. The drifters deployed at 500 m would feel strong topographic

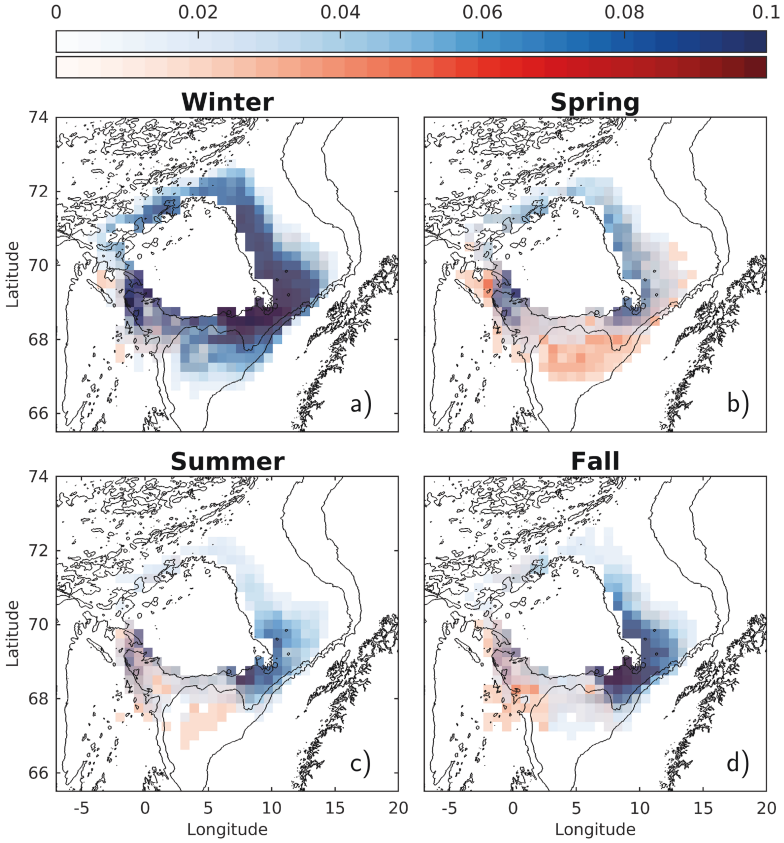

Figure 9. Drifter density maps of 3-D drifters in Depth Class 3 (370 m-bottom) that belonged to (blue colors) Temperature Class 1 (cooling more than 1 ° C in the LB) and (red colors) Temperature Class 4 (warming more than 1 °C in the LB) subsampled by the season of the longest stay entry to the LB. Only trajectory segments from deployment until the longest stay entry to the basin are considered. Color bars show the percentage of drifters in each bin relative to the total number of 3-D drifters in Depth Class 3 (63,661 drifters). Since the color maps can overlap, blue colors are mapped over red colors with 30% transparency. Bin sizes are as in Figure 3.

potential vorticity gradients and remain locked to topography, leading to larger percentages of entry via the HI compared to near the surface.

Inside the LB, the velocity fields revealed the anticyclonic structure of the Lofoten Basin Eddy (LBE) in the center (Ivanov & Korablev, 1995; Fer et al., 2018). The location of this large vortex is close to the Helgeland Ridge. The retention by the eddy is expected to increase the residence time in the basin, particularly for the HI entries. In addition to the LBE, the velocity fields indicated surface-intensified anticylonic structures close to the LSI at the edge of the basin contour. These anticyclonic circulations can have consequences for the residence time of the LSI entries, for example, lead to a relatively rapid exit from the LB in this region and fairly short residence times for the LSI drifters in the LB compared to the HI drifters. The EKE map from the ROMS model (averaged between 1996 and 1999, not shown) identified this region as a secondary EKE maximum (in addition to the LBE). This is consistent with the satellite-derived EKE observations reported in Isachsen et al. (2012), surface drifter trajectories shown by Koszalka et al. (2011), and with the eddy census from altimeter data and surface drifters by Raj et al. (2016). The LSI as an eddy hot spot is further supported by a local deepening of time-averaged potential density surfaces there. For example, the $\sigma_0 = 27.9$ kg/m^3

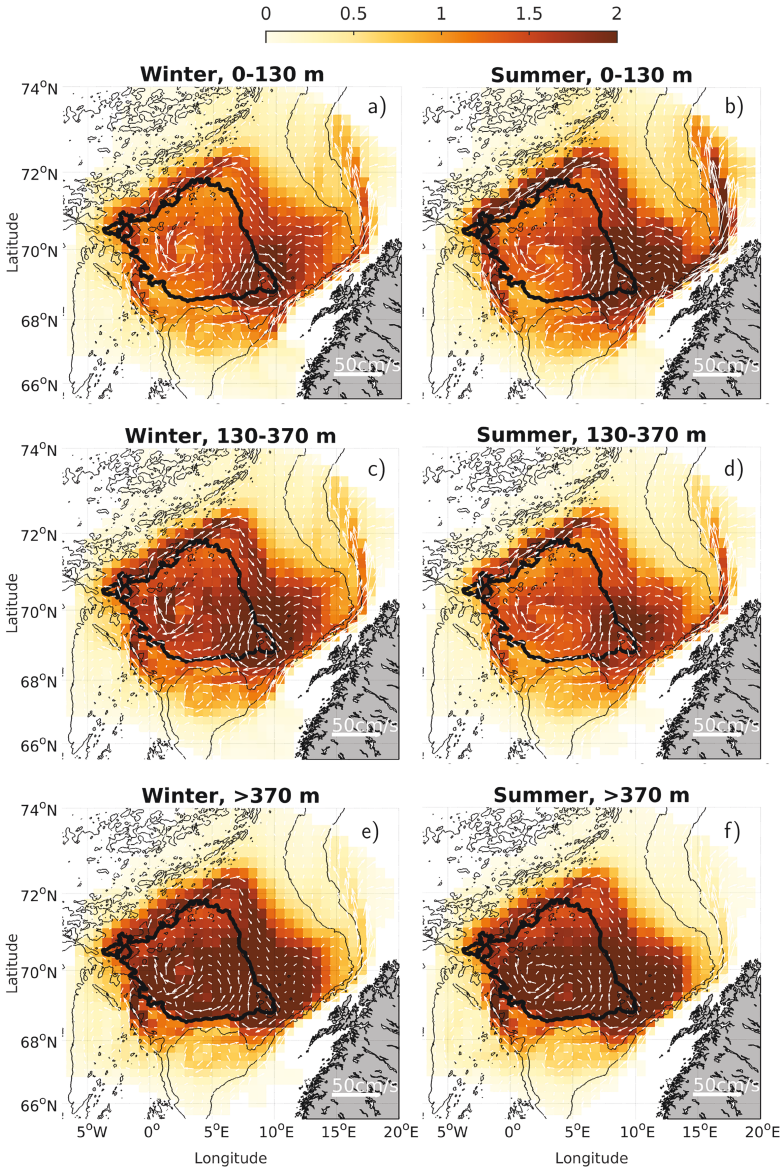

Figure 10. Density maps of 3-D synthetic drifters entering the LB in different seasons, (a, c, and e) January–March and (b, d, and f) July–September, and at different depths. We consider the longest stay entry to define the depth classes 1:0–130 m (a,b), 2:130–370 m (c,d) and 3:370 m–bottom (e,f). Thus, density maps are similar to Figure 5, but here we analyze full trajectories. The color bar shows the percentage of drifters when normalized with the total number of drifters entering the basin summed over depth classes (62,355 + 51,915 + 63,661 = 177,931). Superimposed are the corresponding velocity vectors binned from drifter velocities. Bin sizes are as in Figure 3 and are the same for the drifter density and the velocity fields.

surface reached 600-m depth in the LSI region, approximately the same as in the LB center, consistent with Rossby et al. (2009) and Richards and Straneo (2015). The mean temperature at 200 m was also higher at the LSI compared to the basin (Figure 1b), implying retention of warm water close to the LSI. Because of the on average warm temperature signal in the LSI region, the winter cooling was also more intense there, resulting in larger vertical displacements than in the HI during winter (Figure 4b).

We observe generally higher drifter densities in the basin at deeper levels (Figures 10e and 10f). Drifters at deeper levels from the LSI are advected farther into the basin compared to the surface, suggesting decreased residence times for the 15- and 200-m LSI drifters as a result of the secondary EKE maximum. The increased residence time at depth together with deep-reaching warm water in the LSI compared to surroundings contributes to the strong cooling of water masses entering the LB from the slope via the LSI (Figures 8 and 9).

4.2. Missing Structure and Variability in 2-D Analyses and Observations

The warm Atlantic inflow to the LB exhibits seasonal variability related to changes in atmospheric forcing and the resulting sinking and mixed layer depth evolution. During winter, the 3-D synthetic drifters experience larger vertical displacements (causing the redistribution of the drifters in the vertical), while during summer, the strong stratification restrict the drifters to their deployment level. The seasonal differences are stronger at the surface and less pronounced at depth and lead to differences in the vertical distributions of the synthetic drifters in the 2-D and 3-D simulations, in particular at the surface layer. The combined vertical-seasonal variations of the inflow have consequences for the heat exchange between the AW inflow and the LB.

The seasonal signal at deeper levels in the 3-D drifters was more pronounced than in the 2-D drifters. Half of the 3-D drifters in Temperature Class 1 and Depth Class 3 entered the basin at depths shallower than 500 m. Therefore, they were more likely to be affected by seasonal variations in contrast to the 2-D drifters fixed at 500-m depth. For this reason, deep drifters that are cooled could enter the basin from many regions in winter, but those that experience warming entered typically from south during spring. Another important difference between the 2-D and 3-D drifters is that the number of drifters in Temperature Classes 1 and 4 at deeper levels were substantially less for 3-D drifters (Table 2). While the 2-D drifters are fixed in depth, we observed differences in the depth of entry for the different temperature classes in the 3-D drifters. The majority of 3-D drifters sunk toward the basin (Figure 4), and the median depth of entry for drifters in Depth Class 3 was 545 m. The sinking was also reflected in the temperature classes. The entry median depth for the largest temperature change classes (1 and 4) was about 500 m. These depths are at the base of the Atlantic layer, and the sinking therefore has a large impact on the temperature changes in the basin. The majority of drifters sunk below the Atlantic layer where the water masses are more uniform. The vertically rigid 2-D drifters therefore likely overestimate the temperature changes.

Some important implications of our results thus emerge regarding real Lagrangian observations. Several previous studies have used 2-D surface drifters anchored at 15-m depth and equipped with a temperature sensor to study the AW inflow in the Nordic Seas and its seasonal or winter expression (Andersson et al., 2011; Isachsen et al., 2012; Koszalka et al., 2013; Poulain et al., 1996). Our results suggest that such surface drifters must be used with caution. They do not correctly represent seasonal variations in the surface inflow, which is affected by winter cooling and sinking and then summer warming and restratification (Figures 5 and 6). Furthermore, as the 3-D synthetic drifters also indicate a net sinking toward the LB (Figure 4a), the surface drifters that are anchored at a given depth may give a wrong representation of the water mass characteristics (i.e., salinity and temperature) with time since they do not capture the changes associated with the vertical motion. Our results also suggest that surface drifters alone cannot be used to accurately study the inflow and associated heat exchange because of the variations in the vertical structure of the inflow. To this end, the subsurface floats should complement the surface drifters, as was already pointed out by Rossby et al. (2009). However, due to instrument and deployment costs and technical challenges, there are very few (~20) subsurface float observations in the eastern Nordic Seas and the LB. The observations are too few to provide a basis for the statistical evaluation of our Lagrangian simulations. Furthermore, the subsurface floats that have been used previously in the Nordic Seas are mainly isobaric and thus cannot capture vertical motions, for example, the net sinking experienced by water parcels. Isopycnal floats exist and can to some extent move in the vertical. But by tending to follow isopycnals, they are ill-suited for detecting the diabatic transformations experienced by water parcels. Development of an affordable subsurface float technology that would allow numerous deployments and provide a more realistic measure of the vertical motion

is therefore a priority. Such observations would be invaluable in studying the cooling and sinking processes in the LB, and water mass transformation processes in general. Lacking the observation technology, studies using fully 3-D synthetic drifters serve as a good complement to the already existing Lagrangian field observations.

4.3. Limitations of Our Approach

Our results about the vertical structure and seasonal variations of the inflow are generally consistent with previous studies based on observations and Eulerian modeling (Dugstad et al., 2019; Isachsen et al., 2012; Rossby et al., 2009). However, our study is the first to study the inflow to the LB using 2-D and 3-D Lagrangian simulations based on a high-resolution ocean model.

The relative dispersion statistics from the 2-D Lagrangian simulations at 15 m compared very well with the surface drifter observations, giving confidence on the ability of the ocean model and the Lagrangian model to simulate the near-surface flows. A statistical comparison with observations at deeper levels was not possible because of too few float data. Since computations at deeper levels are based on similar methods, we assumed that drifters at these levels were able to represent the associated flows. The 2-D and 3-D simulations agreed well in pathways and statistics of drifters interacting with the LB and residence time analysis in the basin. We interpreted this as an indication that the 3-D drifters were physically meaningful. Furthermore, the 3-D drifters showed intuitive results, for instance that they moved more freely in the vertical when the stratification was weak and that they were trapped closer to their deployment depth when the stratification was stronger. We therefore have confidence in the 3-D drifters, and, together with the 2-D drifters, the analyzed trajectories can be used to study our earlier defined research problems.

In assessing our results pertaining to vertical motions, one has to bear in mind that the ROMS model used here is hydrostatic and hence does not reproduce convection processes occurring in the LB exactly, but merely parameterizes them. So the results shown and discussed here are related to large-scale and mesoscale flow features rather than to small-scale mixing processes. Although the $k-\epsilon$ vertical mixing scheme applied here has been shown to compare favorably with laboratory experiments (Warner et al., 2005), errors in the mixing scheme can be expected to impact our model predictions, including the resolved vertical flow field. However, mixing-related errors in the model's vertical velocities cannot be too large since the vertical velocities are also constrained by the topographically guided horizontal flow via the continuity equation. Most of our findings regarding vertical motions are also very clear and intuitive. There is a strong distinction in vertical displacements between summer and winter, and there is strong evidence of a net sinking in the LB region with time, consistent with the on average large surface heat and buoyancy loss there (Richards & Straneo, 2015). A closer investigation into the effects of various choices for the vertical parameterization schemes is beyond the scope of this study. And, as argued, the core features seen herein are likely fairly robust to such choices.

The ability of off-line Lagrangian simulations in representing the parameterized vertical diffusion present in the ROMS model can also be questioned. However, for a model output of high-resolution and high output frequency as used here, it is customary not to include additional diffusion; see, for example, Bower et al. (2011), Gelderloos et al. (2017), Rühs et al. (2019), and Dugstad et al. (2019). This is because the dominant turbulent (nonlocal) transport by ocean eddies is resolved and the local small-scale mixing is small in comparison. Adding vertical diffusion (parameterized as random walk for the synthetic drifters) could lead to distorting of the synthetic drifter spreading and make the Lagrangian simulations too diffusive and thus inconsistent with the Eulerian ocean model used to force them. The inclusion of vertical diffusion (as well as lateral diffusion) in Lagrangian models must address a proper choice of the stochastic model and its coefficients with respect to the unresolved nonlocal mixing, boundary effects, and spatially variable diffusivity; see, for example, Hunter et al. (1993), Griffa (1996), and Berloff and McWilliams (2002). In a recent study, Wagner et al. (2019) evaluated the ability of off-line Lagrangian simulations to reproduce spreading of a tracer patch simulated in-line with the advection diffusion equation of the ocean model. They used a daily output of a high-resolution model and a vertical diffusivity coefficient varying by 5 orders of magnitude with depth and seasonally. The detected differences in vertical spreading were small and attributed to daily averaging of the model output and the depth variations in the vertical diffusivity. The model output in our case is four times as frequent (for comparable Lagrangian integral time scale in both regions), which further enhances ability of our Lagrangian model to represent transport processes. However, if we were to

add an unknown yet realistic value of vertical spreading, it would not change the general conclusions from our study but rather enhance the differences between the 2-D and 3-D simulations.

Throughout our discussion regarding temperature changes in the basin, we have used terminology such as "AW-LB heat exchange" and that "drifters can experience cooling." These statements assume that the synthetic drifters represent actual water parcels accurately and that the temperature changes occur along the drifter trajectories. This common assumption can be questioned, as there are no actual measurements on how "Lagrangian" a synthetic drifter or an observed drifter/float is. Especially, since observed drifters/floats are 2-D, they only follow the horizontal components of the flow that can result in errors. However, given that the vertical shear is weak, one can assert that they represent the water masses quite well (LaCasce, 2008; Rossby et al., 2009). The synthetic drifters, and especially the 3-D drifters, can even better represent the trajectory of a water parcel than the observations. They are advected by Lagrangian equations and are therefore purely Lagrangian, with the exception of small numerical errors and uncertainties.

5. Summary and Conclusions

We have studied the AW inflow to the LB by analyzing 2-D (fixed depth) as well as fully 3-D Lagrangian trajectories of synthetic drifters advected by currents from a high-resolution ocean model of the region. Synthetic drifters deployed at three levels (15, 200, and 500 m) were used to deduce the main inflow pathways of AW into the basin, including the vertical structure of the inflow and its seasonal variations. We inferred patterns of heat exchange associated with the inflow at different depths and seasons.

The 2-D Lagrangian simulations at 15 m were compared to surface drifter observations in terms of relative dispersion statistics, showing a close agreement. This gave confidence to the ability of the ocean model and the Lagrangian model to simulate the near-surface flows.

A large percentage of the inflow to the LB (about 50% synthetic drifters at all depths) was concentrated in two regions: one to the east, at the slope close to the Lofoten Islands (LSI), and one to the west, close to the Helgeland Ridge (HI). The mean residence time in the LB increased with depth as the drifters at deeper levels were advected further into the basin compared to drifters near the surface.

The inflow at different depths exhibited seasonal variability, which was most pronounced in the east (LSI). These seasonal differences were stronger at the surface where they led to differences in the distributions of the synthetic drifters in the 2-D and 3-D simulations.

The combined vertical-seasonal variations of the inflow affected the inferred heat exchange between the AW inflow and the LB in the surface layer. The strongest cooling in the LB was experienced by synthetic drifters entering from a broad southern region and was intensified in winter. In late winter the cooling was experienced mostly by the drifters entering from the southeast, through the LSI. During the summer, the synthetic drifters in the surface layer experienced a seasonal warming. This pattern in the near-surface layer was similar in the 2-D and 3-D drifter simulations.

The pattern of the temperature change was different in deeper layers where the 2-D and 3-D simulations also differed. However, the general pathways were quite similar in the two simulations, showing that the cooling was mainly experienced by the warm AW inflow entering from the east (LSI) while the synthetic drifters entering via HI in the west tracked the colder waters of the FC. The 2-D simulations did not capture the seasonal variations at 500 m, but they were pronounced in the 3-D simulations. We explained the differences by the vertical sinking of the 3-D drifters. The drifters that experienced seasonality typically entered the basin at levels shallower than 500 m. However, because the majority of 3-D drifters entered the basin below the base of the Atlantic layer, we found fewer 3-D drifters that experienced large cooling/warming at deeper levels compared to the 2-D drifters at 500-m depth.

Our results suggest that surface drifters must be used with caution, as they might give wrong representations of the seasonal variations in the surface inflow, which is affected by winter cooling and sinking, and summer warming and restratification. The temperature and salinity changes associated with the vertical movements and the variations in the vertical structure of the inflow are not captured by the 2-D synthetic drifters or the surface drifters anchored at a given depth. Lacking the observation technology that can represent the vertical motion associated with water mass transformations, statistical analysis of a large number of 3-D synthetic drifters from high-resolution Lagrangian simulations provides insight.

Acknowledgments
This study received funding from the Research Council of Norway, through the project *Water mass transformation processes and vortex dynamics in the Lofoten Basin in the Norwegian Sea (ProVoLo)*, Project 250784. The surface drifters used in this study are obtained from the Global Drifter Programme (https://www.aoml.noaa.gov/phod/gdp/). The ROMS simulation was made by Marta Trodahl and Nils M. Kristensen of the Norwegian Meteorological Institute and run on resources provided by UNINETT Sigma2-The National Infrastructure for High Performance Computing and Data Storage in Norway; the drifter simulations were performed on servers provided by the Norwegian Meteorological Institute in Oslo, Norway. The ROMS model fields are available at the Thredds Service at the Norwegian Meteorological Institute (https://thredds.met.no/). The 2-D and 3-D Lagrangian simulations will be archived, open-access, at the Norstore research data archive (https://archive.norstore.no/).

References

Andersson, M., Orvik, K. A., Lacasce, J. H., Koszalka, I., & Mauritzen, C. (2011). Variability of the Norwegian Atlantic Current and associated eddy field from surface drifters. *Journal of Geophysical Research*, *116*, C08032. https://doi.org/10.1029/2011JC007078

Årthun, M., Bogstad, B., Daewel, U., Keenlyside, N., Sando, A., & Schrum, C. (2018). Climate based multi-year predictions of the Barents Sea cod stock. *PLoS ONE*, *13*(10), e0206319. https://doi.org/https://doi.org/10.1371/journal.pone.0206319

Årthun, M., Eldevik, T., & Smedsrud, L. H. (2019). The role of Atlantic heat transport in future Arctic winter sea ice loss. *Journal of Climate*, *32*(11), 3327–3341. https://doi.org/10.1175/JCLI-D-18-0750.1

Berloff, P. S., & McWilliams, J. C. (2002). Material transport in oceanic gyres. Part II: Hierarchy of stochastic models. *Journal of Physical Oceanography*, *32*(3), 797–830.

Bosse, A., Fer, I., Søiland, H., & Rossby, T. (2018). Atlantic Water transformation along its poleward pathway across the Nordic Seas. *Journal of Geophysical Research: Oceans*, *123*, 6428–6448. https://doi.org/10.1029/2018JC014147

Bower, A., Lozier, M., & Gary, S. (2011). Export of Labrador Sea Water from the subpolar North Atlantic: A Lagrangian perspective. *Deep Sea Research Part II: Topical Studies in Oceanography*, *58*, 1798–1818. https://doi.org/10.1016/j.dsr2.2010.10.060

Dagestad, K. F., Röhrs, J., Breivik, O., & Ådlandsvik, B. (2018). OpenDrift v1.0: A generic framework for trajectory modelling. *Geoscientific Model Development*, *11*(4), 1405–1420. https://doi.org/10.5194/gmd-11-1405-2018

Dagestad, K. F., & Röhrs, J. (2019). Prediction of ocean surface trajectories using satellite derived vs. modeled ocean currents. *Remote Sensing of Environment*, *223*, 130–142. https://doi.org/10.1016/j.rse.2019.01.001

Dee, D. P., Uppala, S. M., Simmons, A. J., Berrisford, P., Poli, P., Kobayashi, S., & Vitart, F. (2011). The ERA-Interim reanalysis: Configuration and performance of the data assimilation system. *Quarterly Journal of the Royal Meteorological Society*, *137*(656), 553–597. https://doi.org/10.1002/qj.828

Dugstad, J., Fer, I., LaCasce, J. H., Sanchez de La Lama, M., & Trodahl, M. (2019). Lateral heat transport in the Lofoten Basin: Near-surface pathways and subsurface exchange. *Journal of Geophysical Research: Oceans*, *124*, 2992–3006. https://doi.org/10.1029/2018JC014774

Fer, I., Bosse, A., Ferron, B., & Bouruet-Aubertot, P. (2018). The dissipation of kinetic energy in the Lofoten Basin Eddy. *Journal of Physical Oceanography*, *48*, 1299–1316. https://doi.org/10.1175/JPO-D-17-0244.1

Gelderloos, R., Haine, T. W. N., Koszalka, I., & Magaldi, M. (2017). Seasonal variability in warm-water inflow towards Kangerdlugssuaq Fjord. *Journal of Physical Oceanography*, *7*(47), 1685–1699. https://doi.org/10.1175/JPO-D-16-0202.1

Griffa, A. (1996). Applications of stochastic particle models to oceanographic problems. In R. J. Adler, P. Müller, & B. L. Rozovskii (Eds.), *Stochastic Modelling in Physical Oceanography* (pp. 113–140): Birkhäuser Boston.

Haidvogel, D. B., Arango, H., Budgell, W. P., Cornuelle, B. D., Curchitser, E., Di Lorenzo, E., & Wilkin, J. (2008). Ocean forecasting in terrain-following coordinates: Formulation and skill assessment of the Regional Ocean Modeling System. *Journal of Computational Physics*, *227*(7), 3595–3624. https://doi.org/10.1016/j.jcp.2007.06.016

Hunter, J. R., Craig, P. D., & Phillips, H. E. (1993). On the use of random walk models with spatially variable diffusivity. *Journal of Computational Physics*, *106*(2), 366–376. https://doi.org/10.1016/S0021-9991(83)71114-9

Isachsen, P. E. (2015). Baroclinic instability and the mesoscale eddy field aorund the Lofoten Basin. *Journal of Geophysical Research: Oceans*, *120*, 2884–2903. https://doi.org/10.1002/2014JC010448-

Isachsen, P. E., Koszalka, I., & Lacasce, J. H. (2012). Observed and modeled surface eddy heat fluxes in the eastern Nordic Seas. *Journal of Geophysical Research*, *117*, C08020. https://doi.org/10.1029/2012JC007935

Isachsen, P. E., LaCasce, J. H., Mauritzen, C., & Häkkinen, S. (2003). Wind-driven variability of the large-scale recirculating flow in the Nordic Seas and Arctic Ocean. *Journal of Physical Oceanography*, *33*(12), 2534–2550. https://doi.org/10.1175/1520-0485(2003)033<2534:WVOTLR>2.0.CO;2

Ivanov, V., & Korablev, A. A. (1995). Formation and regeneration of the pycnocline lens in the Norwegian Sea. *Russian Meteorology and Hydrology*, *9*(9), 62–69.

Jones, C. E., Dagestad, K. F., Breivik, Ø., Holt, B., Röhrs, J., Christensen, K. H., & Skrunes, S. (2016). Measurement and modeling of oil slick transport. *Journal of Geophysical Research: Oceans*, *121*, 7759–7775. https://doi.org/10.1002/2016JC012113

Köhl, A. (2007). Generation and stability of a quasi-permanent vortex in the Lofoten Basin. *Journal of Physical Oceanography*, *37*(11), 2637–2651. https://doi.org/10.1175/2007JPO3694.1

Koszalka, I., LaCasce, J. H., Andersson, M., Orvik, K. A., & Mauritzen, C. (2011). Surface circulation in the Nordic Seas from clustered drifters. *Deep-Sea Research Part I: Oceanographic Research Papers*, *58*(4), 468–485. https://doi.org/10.1016/j.dsr.2011.01.007

Koszalka, I., LaCasce, J. H., & Mauritzen, C. (2013). In pursuit of anomalies—Analyzing the poleward transport of Atlantic Water with surface drifters. *Deep-Sea Research Part II: Topical Studies in Oceanography*, *85*, 96–108. https://doi.org/10.1016/j.dsr2.2012.07.035

Koszalka, I., LaCasce, J. H., & Orvik, K. A. (2009). Relative dispersion in the Nordic Seas. *Journal of Marine Research*, *67*(4), 411–433. https://doi.org/10.1357/002224009790741102

Kovacs, K. M., Lydersen, C., Overland, J. E., & Moore, S. E. (2011). Impacts of changing sea-ice conditions on Arctic marine mammals. *Marine Biodiversity*, *41*(1), 181–194. https://doi.org/10.1007/s12526-010-0061-0

Kvile, K. Ø., Romagnoni, G., Dagestad, K. F., Langangen, Ø., & Kristiansen, T. (2018). Sensitivity of modelled North Sea cod larvae transport to vertical behaviour, ocean model resolution and interannual variation in ocean dynamics. *ICES Journal of Marine Science*, *75*(7), 2413–2424. https://doi.org/10.1093/icesjms/fsy039

LaCasce, J. H. (2008). Statistics from Lagrangian observations. *Progress in Oceanography*, *77*(1), 1–29. https://doi.org/10.1016/j.pocean.2008.02.002

Lumpkin, R., & Pazos, M. (2007). Measuring surface currents with Surface Velocity Program drifters: The instrument, its data, and some recent results. *Lagrangian Analysis and Prediction of Coastal and Ocean Dynamics*, 39–67 (Chapter 2). https://doi.org/10.1017/CBO9780511535901.003

MacLachlan, C., Arribas, A., Peterson, K. A., Maidens, A., Fereday, D., Scaife, A. A., & Madec, G. (2015). Global Seasonal forecast system version 5 (GloSea5): A high-resolution seasonal forecast system. *Quarterly Journal of the Royal Meteorological Society*, *141*(689), 1072–1084.

Mauritzen, C. (1996). Production of dense overflow waters feeding the North Atlantic across the Greenland-Scotland Ridge. Part 1: Evidence for a revised circulation scheme. *Deep Sea Research Part 1: Oceanographic Research Papers*, *43*(6), 769–806. https://doi.org/10.1016/0967-0637(96)00037-4

Nøst, O. A., & Isachsen, P. (2003). The large-scale time-mean ocean circulation in the Nordic Seas and Arctic Ocean estimated from simplified dynamics. *Journal of Marine Research*, *61*(2), 175–210. https://doi.org/10.1357/002224003322005069

Ogawa, F., Keenlyside, N., Gao, Y., Koenigk, T., Yang, S., Suo, L., & Semenov, V. (2018). Evaluating impacts of recent Arctic Sea ice loss on the Northern Hemisphere winter climate change. *Geophysical Research Letters*, *45*(7), 3255–3263. https://doi.org/10.1002/2017GL076502

Orvik, K. A., & Niiler, P. (2002). Major pathways of Atlantic water in the northern North Atlantic and Nordic Seas toward Arctic. *Geophysical Research Letters*, *29*(19), 1896. https://doi.org/10.1029/2002GL015002

Poulain, P. M., Warn-Varnas, a., & Niiler, P. P. (1996). Near-surface circulation of the Nordic seas as measured by Lagrangian drifters. *Journal of Geophysical Research*, *101*, 18,237–18,258. https://doi.org/10.1029/96JC00506

Raj, R., Johannesen, J., Eldevik, T., Nilsen, J., & Halo, I. (2016). Quantifying mesoscale eddies in the Lofoten Basin. *Journal of Geophysical Research: Oceans*, *121*, 4503–4521. https://doi.org/10.1002/2016JC011637

Richards, C. G., & Straneo, F. (2015). Observations of water mass transformation and eddies in the Lofoten Basin of the Nordic Seas. *Journal of Physical Oceanography*, *45*(6), 1735–1756. https://doi.org/10.1175/JPO-D-14-0238.1

Rossby, T., Ozhigin, V., Ivshin, V., & Bacon, S. (2009). An isopycnal view of the Nordic Seas hydrography with focus on properties of the Lofoten Basin. *Deep-Sea Research Part I: Oceanographic Research Papers*, *56*(11), 1955–1971. https://doi.org/10.1016/j.dsr.2009.07.005

Rossby, T., Prater, M. D., & Søiland, H. (2009). Pathways of inflow and dispersion of warm waters in the Nordic Seas. *Journal of Geophysical Research*, *114*, C04011. https://doi.org/10.1029/2008JC005073

Rühs, S., Schwarzkopf, F. U., Speich, S., & Biastoch, A. (2019). Cold vs. warm water route—Sources for the upper limb of the Atlantic Meridional Overturning Circulation revisited in a high-resolution ocean model. *Ocean Science*, *15*(3), 489–512. https://doi.org/10.5194/os-15-489-2019

Segtnan, O. H., Furevik, T., & Jenkins, A. D. (2011). Heat and freshwater budgets of the Nordic seas computed from atmospheric reanalysis and ocean observations. *Journal of Geophysical Research*, *116*, C11003. https://doi.org/10.1029/2011JC006939

Shchepetkin, A. F., & McWilliams, J. C. (2005). The regional oceanic modeling system (ROMS): A split-explicit, free-surface, topography-following-coordinate oceanic model. *Ocean Modelling*, *9*(4), 347–404. https://doi.org/10.1016/j.ocemod.2004.08.002

Shchepetkin, A. F., & McWilliams, J. C. (2009). Correction and commentary for "Ocean forecasting in terrain-following coordinates: Formulation and skill assessment of the regional ocean modeling system" by Haidvogel et al., J. Comp. Phys. 227, pp. 3595-3624. *Journal of Computational Physics*, *228*(24), 8985–9000. https://doi.org/10.1016/j.jcp.2009.09.002

Spall, M. A. (2010). Dynamics of downwelling in an eddy-resolving convective basin. *Journal of Physical Oceanography*, *40*(10), 2341–2347. https://doi.org/10.1175/2010JPO4465.1

Trodahl, M., & Isachsen, P. E. (2018). Topographic influence on baroclinic instability and the mesoscale eddy field in the northern North Atlantic Ocean and the Nordic Seas. *Journal of Physical Oceanography*, *48*(11), 2593–2607. https://doi.org/10.1175/JPO-D-17-0220.1

Umlauf, L., & Burchard, H. (2003). A generic length-scale equation for geophysical turbulence models. *Journal of Marine Research*, *61*(2), 235–265.

van Sebille, E., Griffies, S. M., Abernathey, R., Adams, T. P., Berloff, P., Biastoch, A., & Zika, J. D. (2018). Lagrangian ocean analysis: Fundamentals and practices. *Ocean Modelling*, *121*(October 2017), 49–71. https://doi.org/10.1016/j.ocemod.2017.11.008

Volkov, D. L., Belonenko, T. V., & Foux, V. R. (2013). Puzzling over the dynamics of the Lofoten Basin—A sub-Arctic hot spot of ocean variability. *Geophysical Research Letters*, *40*, 738–743. https://doi.org/10.1002/grl.50126

Volkov, D. L., Kubryakov, A. A., & Lumpkin, R. (2015). Formation and variability of the Lofoten basin vortex in a high-resolution ocean model. *Deep-Sea Research Part I: Oceanographic Research Papers*, *105*, 142–157. https://doi.org/10.1016/j.dsr.2015.09.001

Wagner, P., Rühs, S., Schwarzkopf, F. U., Koszalka, I., & Biastoch, A. (2019). Can Lagrangian tracking simulate tracer spreading in a high-resolution Ocean General Circulation Model? *Journal of Physical Oceanography*, *49*(5), 1141–1157. https://doi.org/10.1175/JPO-D-18-0152.1

Warner, J. C., Sherwood, C. R., Arango, H. G., & Signell, R. P. (2005). Performance of four turbulence closure models implemented using a generic length scale method. *Ocean Modelling*, *8*(1-2), 81–113.

Paper IV

Norwegian Atlantic Slope Current along the Lofoten Escarpment

I. Fer, A. Bosse, J.S. Dugstad
Ocean Science, **16** (2020)

Ocean Sci., 16, 685–701, 2020
https://doi.org/10.5194/os-16-685-2020

Ocean Science Open Access EGU

Norwegian Atlantic Slope Current along the Lofoten Escarpment

Ilker Fer[1], **Anthony Bosse**[1,a], **and Johannes Dugstad**[1]

[1]Geophysical institute, University of Bergen, and Bjerknes Centre for Climate Research, Bergen, Norway
[a]now at: Aix-Marseille Univ., Université de Toulon, CNRS, IRD, MIO UM 110, Marseille, France

Correspondence: Ilker Fer (ilker.fer@uib.no)

Received: 21 February 2020 – Discussion started: 27 February 2020
Revised: 28 April 2020 – Accepted: 5 May 2020 – Published: 4 June 2020

Abstract. Observations from moored instruments are analyzed to describe the Norwegian Atlantic Slope Current at the Lofoten Escarpment (13° E, 69° N). The data set covers a 14-month period from June 2016 to September 2017 and resolves the core of the current from 200 to 650 m depth between the 650 and 1500 m isobaths. The along-isobath current, vertically averaged between 200 and 600 m depth, has an annual cycle amplitude of 0.1 m s^{-1}, with the strongest currents in winter, and a temporal average of 0.15 m s^{-1}. Higher-frequency variability is characterized by fluctuations that reach 0.8 m s^{-1}, lasting for 1 to 2 weeks, and extend as deep as 600 m. In contrast to observations in Svinøy (2° E, 63° N), the slope current is not barotropic and varies strongly with depth (a shear of 0.05 to 0.1 m s^{-1} per 100 m in all seasons). Within the limitations of the data, the average volume transport of Atlantic Water is estimated at 2.0 ± 0.8 Sv ($1\,\text{Sv} = 10^6\,\text{m}^3\,\text{s}^{-1}$), with summer and winter averages of 1.6 and 2.9 Sv, respectively. The largest transport is associated with the high temperature classes ($> 7\,^\circ$C) in all seasons, with the largest values of both transport and temperature in winter. Calculations of the barotropic and baroclinic conversion rates using the moorings are supplemented by results from a high-resolution numerical model. While the conversion from mean to eddy kinetic energy (e.g., barotropic instability) is likely negligible over the Lofoten Escarpment, the baroclinic conversion from mean potential energy into eddy kinetic energy (e.g., baroclinic instability) can be substantial, with volume-averaged values of $(1–2) \times 10^{-4}$ W m^{-3}.

1 Introduction

The relatively mild climate of Norway is largely attributed to the northern extension of the North Atlantic Drift, the Norwegian Atlantic Current that transports warm and saline water masses toward the Arctic Ocean (Seager et al., 2002; Rhines et al., 2008). These nutrient-rich warm waters contribute to supporting the entire food chain and sustain the productive waters around Norway (see, e.g., Sundby, 2000, for a discussion on recruitment of Atlantic cod stocks). The circulation pattern is organized in two main branches originating from the Iceland–Faroe and Faroe–Shetland gaps (Poulain et al., 1996; Orvik and Niiler, 2002) (Fig. 1a): the Norwegian Atlantic Slope Current (the slope current hereinafter) and the Norwegian Atlantic Front Current (the front current hereinafter). The diverging isobaths of the Lofoten Basin in the Norwegian Sea guide the two branches. The slope current follows the shelf break along the Norwegian continental slope northward and continues into the Barents Sea and Fram Strait. The front current follows the 2000 m isobath, veers west at the flanks of Vøring Plateau and continues poleward along the Mohn Ridge (Orvik and Niiler, 2002; Bosse and Fer, 2019).

The front current, which is not addressed in this study, has not been measured in detail using current meter arrays, but geostrophic transport estimates are available from hydrography. At the Svinøy section (63° N, about 300 km downstream of the Faroe–Shetland Channel), a baroclinic geostrophic transport estimate of the front current was 3.4 Sv ($1\,\text{Sv} = 10^6\,\text{m}^3\,\text{s}^{-1}$) (Orvik et al., 2001); however, the total geostrophic transport from repeated Seaglider transects reached 6.8 Sv (Høydalsvik et al., 2013), implying a large barotropic contribution. Farther north, detailed glider observations of the front current over the Mohn Ridge confirm

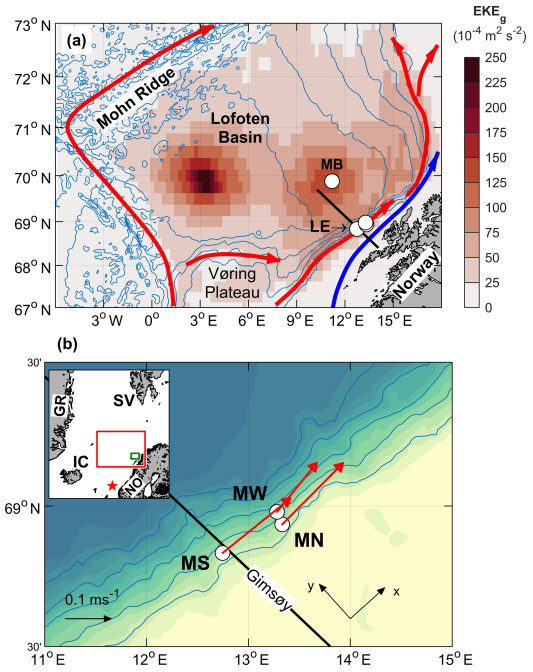

Figure 1. **(a)** Bathymetry of the Lofoten Basin in the Norwegian Sea (ETOPO1, contours at 500 m intervals) and EKE_g averaged over the period 1993 to 2018, calculated using sea level anomalies from satellite altimeter observations. General circulation of the warm Atlantic Water is indicated by red arrows, showing the slope current and the front current. The Norwegian coastal current is indicated by the blue arrow. The black transect is the portion of the Gimsøy section shown in Fig. 2. Mooring positions are shown by circles, also showing the basin mooring (MB) at the secondary EKE_g maximum. The Lofoten Escarpment (LE) is the steep slope region near the slope moorings. **(b)** A zoom-in to the moorings analyzed in this study, showing MS, MN and MW together with 200–600 m depth-averaged current vectors (scale on lower left), the Gimsøy section (black) and the orientation of the coordinate system (along-isobath, x, and cross-isobath, y). Blue isobaths are drawn every 500 m. The inset is a location map with domains of **(a)** and **(b)** marked in red and green, respectively. The monitoring location for the Svinøy section is shown by the red star. NO: Norway, SV: Svalbard, IC: Iceland, GR: Greenland.

large transport rates, giving a 4.5 Sv annual average with an approximately 2 Sv barotropic contribution (Bosse and Fer, 2019).

The University of Bergen, Norway, has monitored the slope current transport at the Svinøy section since 1995 at the location indicated by a star in the inset of Fig. 1b (Orvik et al., 2001). The slope current there is about 40 km wide between the 200 and 900 m isobaths, with an annual mean speed of 0.3 m s^{-1}. The average annual transport of this barotropic branch is 4.4 Sv (Orvik et al., 2001; Orvik and Skagseth, 2003). The slope current accelerates along steep topography off the Lofoten Escarpment near the Lofoten Islands (Poulain et al., 1996). The Norwegian coastal current (blue arrow Fig. 1) carries relatively fresh water over the shelf and as the shelf gets narrow near the Lofoten Escarpment, there might be interactions with the slope current. Here, there are no published moored current meter records, but surface drifters indicate velocities reaching 1 m s^{-1} (Andersson et al., 2011). The transport and variability of the slope current in this region are not known. It is hypothesized that the current becomes increasingly unstable near this topographic steepening. Using time-averaged fields of an eddy-resolving numerical ocean simulation, Isachsen (2015) showed that the steep Lofoten Escarpment exhibits enhanced unstable baroclinic growth rates and large velocity variability, suggesting high lateral diffusion rates. The structure and transport of the slope current at the Lofoten Escarpment are the focus of this study.

The Lofoten Basin is affected by Atlantic Water (AW) transport and becomes a major heat reservoir that is exposed to large surface heat losses (Rossby et al., 2009b; Dugstad et al., 2019a) and substantial water mass transformations (Rossby et al., 2009a; Bosse et al., 2018). AW enters the basin both as a broad slab in the upper layers between the two branches (Rossby et al., 2009b; Dugstad et al., 2019a) and by eddies detached from the unstable slope current (Köhl, 2007; Isachsen, 2015; Volkov et al., 2015; Richards and Straneo, 2015). The eddy-induced lateral heat fluxes distribute heat in the basin (Spall, 2010; Isachsen et al., 2012; Dugstad et al., 2019a). The region is energized, which is manifested in the map of average geostrophic eddy kinetic energy (Fig. 1a; see Sect. 3) showing two maxima: one in the center, associated with a permanent, energetic eddy (Ivanov and Korablev, 1995; Søiland and Rossby, 2013; Fer et al., 2018; Bosse et al., 2019), and a secondary maximum closer to the slope, likely associated with the variability induced by the slope current. The energetics and the variability of the slope current remain to be constrained by observations.

The study was conducted as a part of the "Water mass transformation processes and vortex dynamics in the Lofoten Basin of the Norwegian Sea" (PROVOLO) project. The overall objective of PROVOLO was to describe and quantify the processes and pathways of energy transfer and mixing in the Lofoten Basin and their role in water mass transformation. Observations from multiple cruises, gliders and subsurface floats were analyzed and reported elsewhere with focus on AW transformation (Bosse et al., 2018), the permanent Lofoten Basin Eddy (Fer et al., 2018; Bosse et al., 2019) and the frontal structure across the Mohn Ridge (Bosse and Fer, 2019). The mooring component concentrated on the slope current. Here we report the first observations of the volume transport rates, energetics and their variability from weekly to seasonal timescales based on the mooring records.

Table 1. Mooring deployment and recovery details. Total depth is estimated from the deepest pressure sensor, mooring line construction and the ship's echo sounder.

Mooring	Latitude	Longitude	Depth (m)	Deployed	Recovered
MS	68° N 50.038′	012° E 44.777′	672	31 May 2016	8 September 2017[a]
MN	68° N 56.109′	013° E 19.866′	655	1 June 2016	8 September 2017[b]
MW	68° N 58.759′	013° E 16.845′	1500	1 June 2016	8 September 2017
MB	69° N 52.89′	011° E 11.89′	2925	2 June 2016	9 September 2017

[a] Water column line is lost. [b] Water column line is recovered on 24 August 2016.

2 Data

2.1 Moorings

A set of four moorings was deployed across the continental slope of the eastern Lofoten Basin (Fig.1). A deployment and recovery summary is listed in Table 1, and full details are provided with the documentation following the data set (Fer, 2020). The mooring name convention is Mooring North (MN), South (MS), West (MW) and Basin (MB). MB was located at the secondary geostrophic eddy kinetic energy (EKE_g) maximum (Fig. 1a) to address the mesoscale variability in the basin. Data from this mooring will be analyzed for a separate study and are not reported here. The observations cover a 14-month period from June 2016 to September 2017.

The arrangement of the three moorings on the slope (Fig. 1b) was designed to cover the core of the slope current (two moorings at the 650 and 1500 m isobaths, MN and MW) and to investigate the covariability along the slope (two moorings at the 650 m isobath). The along-isobath distance between MS and MN is 26 km, and the cross-isobath distance between MN and MW is about 5 km. Moorings MS and MN at the 650 m isobath each consisted of one bottom unit and a water column line with distributed conductivity–temperature–depth (CTD) sensors. The bottom units were approximately 25 m tall and equipped with an RDI 75 kHz Long Ranger acoustic Doppler current profiler (ADCP) in a spherical flotation and a Sea-Bird Scientific SBE37 Microcat with CTD sensors. This approach mitigated the high risk due to fisheries activities. The ADCP bottom unit and mooring line pairs were deployed close to each other at approximately the same isobath (within 5 m) and within 250 m horizontally; they will be treated as a single mooring. Unfortunately, both water column mooring lines at MN and MS were damaged by fishing boats. The MS line was lost with no data return. The MN line was cut after 3 months. The drifting MN line and the sensors were recovered, giving 3 (summer) months of temperature and salinity data in the water column. The current profile and the near-bottom CTD data from the bottom units were successfully recovered and cover the whole study period.

The moorings were densely instrumented and sampled at an hourly rate or faster, covering a large fraction of the water column. The instrument target depths can be seen on the vertical axis in Fig. 4, introduced later. Currents were measured using ADCPs, mainly RDI 75kHz Long Rangers for the moorings reported here, and point current meters (Aanderaa SeaGuard, Xylem Inc.). The ADCPs on MN, MS and MW were placed to cover the dynamic core of the slope current (at approximately 10 m height above the seabed at the 650 m isobath and at 740 m depth at the 1500 m isobath, each pointing upward with about 550 m range). Temperature, salinity and pressure were sampled using SBE temperature loggers (SBE56 and SBE39) and CTD recorders (Microcat, SBE37). The detailed instrument distribution on moorings can be found in the data set documentation (Fer, 2020). Current measurements were corrected for magnetic declination. After all moorings were recovered, a calibration CTD cast was made with all mooring SBE sensors attached to the ship's CTD frame. The temperature and salinity measurements were corrected to be internally consistent and also against the calibration cast and the profiles taken when the moorings were in water. The applied offset corrections for each instrument are listed in the data set report and vary in the range of $(1\text{–}40)\times10^{-3}$ °C for temperature and $(2\text{–}50)\times10^{-3}$ for practical salinity.

Substantial vertical displacements ("knockdown") of the mooring line occurred in response to strong current events at MW and MB (not reported here). At MW, the vertical displacements recorded by the uppermost pressure sensor at the 75 m target depth were 7 m (50th percentile), 15 m (80th percentile, corresponding to a total duration of about 3 months) and 68 m (97th percentile, corresponding to events with a total duration of 2 weeks). The vertical displacements were reduced by approximately a factor of 2 at the level of the ADCP flotation at 740 m depth. The velocity measurements from the ADCPs installed in the bottom units at MN and MS were relatively unaffected by the mooring motion (typical vertical displacements associated with knockdown were less than 1 m with a 97th percentile value of 2 m). Overall, the moorings were equipped with several pressure sensors, which we used to approximate the depth of temperature, salinity and current measurements in the water column.

A data set was prepared after correcting for mooring knockdowns. Data from all instruments were first averaged into 1 h intervals (if the sampling rate was faster) and then interpolated to a common 1 h time array. Time series of instrument depth were constructed at each time and for each instrument using vertical interpolation of the known target depth (of instruments with a pressure sensor) and the measured pressure to the target depths of all instruments. Hourly profiles of temperature, salinity and horizontal current were then vertically interpolated to a uniform 10 m vertical resolution. Data gaps at a given vertical level were typically caused by mooring knockdown or lack of acoustic scatterers for Doppler velocity measurements. At MW, velocity measurements were relatively limited in the vertical. The data gap in the time series was 18 % at 250 m depth, reaching 60 % at 200 m. The vertical extent of temperature measurements at MW was better: the temporal gap at 90 m was only 20 %, increasing to 70 % at 80 m. The missing velocity data at MN comprised 35 % at 150 m, increasing to 50 % at 80 m. A depth level with a data coverage less than 30 % of the total measurement duration was excluded from the data set.

The initial accuracy of the SBE sensors is $\pm 2 \times 10^{-3}$ °C for temperature, $\pm 3 \times 10^{-4}$ S m^{-1} for conductivity and ± 1 dbar for pressure (drift over 1 year is comparable to initial accuracy for temperature and pressure and 10 times the initial accuracy for conductivity). For the deployment setup used, the ADCPs have a single-ping (profile) statistical error of 2.5 cm s^{-1}, which is reduced to 0.4 cm s^{-1} for the ensemble average profile with 35 pings. The compass direction is accurate to $\pm 2°$. Conservative error estimates are ± 1 cm s^{-1} for velocity, $\pm 10^{-2}$ °C for temperature and $\pm 10^{-2}$ for practical salinity.

For the analysis in this study, we rotated the coordinate system by 42° from the east, with the x axis pointing along-isobath and the y axis cross-isobath toward deeper water (see Fig. 1b). The mean orientation of the slope was calculated using isobaths from ETOPO1 near the slope moorings. Current components are along-isobath, u, and cross-isobath, v. The hourly averaged data set was filtered using a 14 d low-pass filter for background fields and a 35 h to 14 d band-pass filter for eddy covariance and conversion rate calculations. In both cases a third-order phase-preserving Butterworth filter was used.

2.2 Other data

Atmospheric forcing was obtained from the European Centre for Medium-Range Weather Forecasts (ECMWF) ERA-Interim (Dee et al., 2011) reanalysis over the historical time period from 1979 to 2018 and from the higher-resolution ERA-5 reanalysis (Copernicus Climate Change Service, 2017) over the mooring observation period. Surface net fluxes Q_{net} (downward positive) were computed as the sum of net shortwave and longwave contributions and latent and sensible heat fluxes. Time series of fluxes were extracted at the nearest grid point from mooring sites. We calculated $\mathrm{EKE_g}$ using the surface geostrophic velocity anomalies obtained from the sea level anomaly from the multimission altimeter satellite gridded sea surface height observations distributed by the EU Copernicus Marine Service Information.

Hydrography data from the standard Gimsøy section available from four occupations during the mooring period (on 30 July 2016, 19 November 2016, 8 March 2017 and 7 June 2017) were obtained from the Norwegian Marine Data Centre.

Climatological transects at the Svinøy and Gimsøy sections were constructed from a hydrographical atlas of the Nordic Seas (Bosse and Fer, 2018). This is a merged data set including observations from shipboard CTD, Argo profiling floats and underwater gliders between 2000 and 2017. To construct the sections discussed in Sect. 7, we used all profiles located within 25 km of distance from the Svinøy and Gimsøy transects, projected horizontally onto the transect and binned in 5 km cross-sectional intervals. Seasonal averages for temperature and salinity were smoothed using a Gaussian moving window of 10 km variance. Finally, we calculated the annual mean by averaging over four seasonal sections.

In order to assess how representative our discussion of energetics obtained from mooring data is of the volume-averaged energetics in the region, we performed calculations using outputs from a high-resolution Regional Ocean Modelling System (ROMS) configuration in the Nordic Seas. ROMS is a hydrostatic model with terrain-following coordinates that solves the primitive equations on a staggered C grid (Shchepetkin and McWilliams, 2009; Haidvogel et al., 2008). The model outputs used here have a horizontal resolution of 800 m, have 60 vertical layers with increased resolution towards the surface (1–3 m at the surface and about 60 m at the bottom) and are stored as 6-hourly outputs. The model fields are described in detail in Dugstad et al. (2019b).

3 Context and environmental forcing

The standard Gimsøy section was visited four times throughout the mooring period. An average section using the subset of stations taken in all four occupations is representative of the hydrography during the measurements (Fig. 2; also compare to the section from climatology presented in Sect. 7). The AW, identified by temperatures above 5 °C and Absolute Salinities $S_{\mathrm{A}} > 35.17$, covered the 50–700 m layer from the shelf edge toward the basin, overlying the fresher and colder deeper water. The interface between these water masses meets the bottom slope at about 700 m. A relatively fresh layer on the shelf is associated with the Norwegian coastal current. The moorings MN and MW, marked in Fig. 2, show that the range of current measurements sufficiently covered the AW layer and the dynamical core at the slope identified by sloping isotherms.

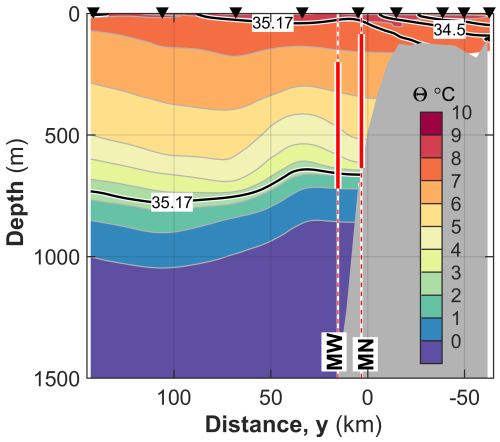

Figure 2. Conservative Temperature (Θ, in color, contours at 1 °C intervals) and Absolute Salinity (black lines; 34, 34.5 and 35.17 g kg^{-1} contours) distribution at the Gimsøy section averaged over four occupations throughout the mooring period. Only stations (arrowheads) with four profiles are used. $S_A = 35.17$ approximately corresponds to a practical salinity of 35 (typical lower limit for AW) at this latitude, 300 dbar pressure and 5 °C temperature. Bathymetry is from ETOPO1. Distance along y is referenced to the 500 m isobath. The moorings MN and MW are shown at the distance on the section corresponding to their deployment isobaths. The vertical extent of the ADCP current profiling is marked with thick red.

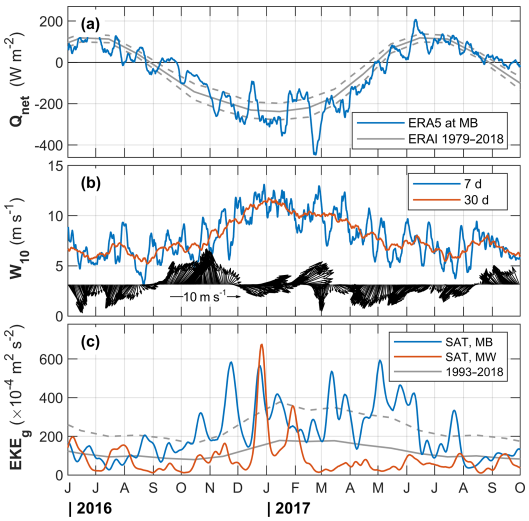

Figure 3. Environmental forcing conditions throughout the mooring deployment period. **(a)** Net surface heat flux, Q_{net}, from ERA5 at the grid point closest to MB, together with the monthly average and 1 standard deviation (σ) envelope for the period between 1979 and 2018. **(b)** Weekly and monthly averages of 10 m wind speed and wind vectors from ERA5. **(c)** EKE$_g$ from satellite altimetry calculated at the grid point closest to MB (blue) and MW (red), together with the monthly average and 1 σ between 1993 and 2018 at MB.

A summary of the environmental forcing during the measurement period shows that the net surface flux was typical of the long-term average, with an event of strong heat loss exceeding the 1 standard deviation (σ) envelope from mid-February to early March 2017 (Fig. 3a). Wind speed showed seasonal variability, increasing from 5 m s^{-1} in summer to 12 m s^{-1} in winter (Fig. 3b). We averaged the EKE$_g$ from satellite altimetry in a 30 km radius at the basin mooring location (an EKE$_g$ maximum region; see Fig. 1a) and at MW and compare the evolution throughout the mooring deployment in Fig. 3c. The EKE$_g$ records confirm that MB is 2 to 5 times more energetic in general, except in summer when both locations were relatively quiescent.

4 Average properties and seasonal profiles

Profiles temporally averaged in the winter (DJF), spring (MAM), summer (JJA) and fall (SON) months at MW and MN show strong vertical shear in u in the upper 600 m at both moorings (Fig. 4). In contrast to the barotropic slope current at Svinøy, the current at the Lofoten Escarpment clearly has a strong baroclinic component. Background shear between 200 and 600 m depth was 0.05 to 0.10 m s^{-1} per 100 m in all seasons, with a maximum in the fall. The fall was characterized by maximum baroclinicity, whereas winter was characterized by maximum barotropic currents, consistent with increased winds. Increased baroclinicity in the fall could partly be due to seasonal freshening of the coastal current reinforcing the density gradients and partly due to increased Ekman transport toward the shore observed from September to March (see northward winds implying eastward Ekman transport in Fig. 3b). It is also likely that the slope current could interact with the fresh coastal current due to the narrow shelf off the Lofoten Escarpment.

Over the full record, the 200–600 m depth-averaged u was 0.15 m s^{-1}. The strongest currents were observed in winter with an average of 0.20 m s^{-1} at MW and 0.25 m s^{-1} at MN (approximately twice the summer average) when the temperature was also the highest. The average winter temperature at MW was 7.3 °C compared to 5.8 °C (at MW) or 6 °C (at MN) in summer. The average temperature in the 200–600 m range was warmer by more than 1 °C in winter. This could partly be explained by vertical redistribution through winter vertical mixing of heat contained in the seasonal thermocline and partly by changes in AW properties flowing into the Nordic Seas. The cross-isobath component was weak (typically ±0.02 m s^{-1}) and increased in spring and winter, with the largest 200–600 m depth-averaged values in winter (0.05 m s^{-1} at MW) and an increased variability with

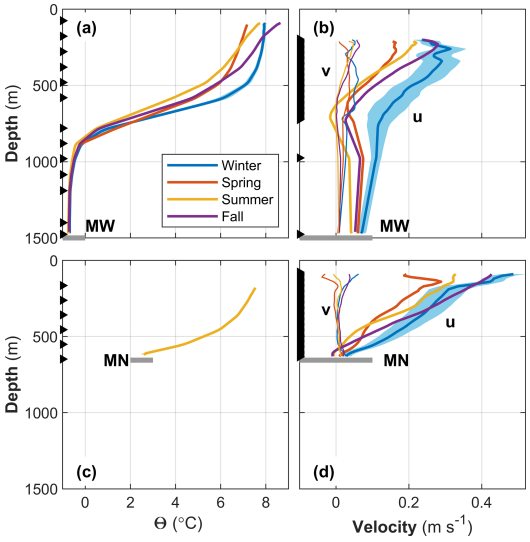

Figure 4. Time-averaged profiles of **(a, c)** Θ and **(b, d)** velocity components u (thick) and v (thin lines) for moorings MW **(a, b)** and MN **(c, d)**. Time averaging is made over the seasons winter, spring, summer and fall, as indicated in the legend. The gray horizontal line marks the seabed. Arrowheads on the vertical axis mark the target depth of measurements. The error bars are the standard error using a decorrelation timescale of 7 d, for clarity shown only for winter (summer for MN temperature), and are comparable in other seasons. The error shading for temperature is not distinguishable from the average profile.

depth (Fig. 4b, d). In the upper part of the water column at MW, averaged cross-isobath velocities in fall exceeded the winter values. This is consistent with the increased EKE_g at the MW location, calculated from satellite measurements in November 2016 (Fig. 3c). In deep layers (> 900 m) at MW, barotropic currents were between 0.05 and 0.10 m s^{-1}.

The summer profiles in Fig. 4 are averages over the summers of 2016 and 2017. When averaged separately (not shown), temperature profiles at MW are very similar, equal to within 0.5 °C in the upper 600 m and identical in deeper layers. At MW, u was 0.01 m s^{-1} larger below 300 m (a small barotropic increase) in summer 2017, and shear was stronger in the upper 300 m, increasing by 0.06 m s^{-1} to 200 m depth. At MN, summer average profiles of u in the bottom 250 m were identical in 2016 and 2017, but shear was stronger higher in the water column (above 400 m) in summer 2017, with u increasing by an additional 0.10 m s^{-1} to 200 m depth. This implies substantial interannual variability in the upper 300–400 m, which cannot be resolved by our limited times series.

5 Temporal variability

The currents measured at moorings MW and MN were highly variable (Fig. 5). The 14 d low-passed currents were strongest in the fall and winter (Fig. 5a–d). The annual cycle of the 200–300 m vertically averaged u at MN had an amplitude of 0.10 m s^{-1} and explains 20 % of the variance obtained using a sinusoidal fit to daily data (not shown). These figures are similar for MW for 300–400 m averaged currents (depth ranges are chosen to ensure continuous time series unaffected by mooring knockdowns). The cross-isobath components show a less pronounced seasonality with 0.01–0.02 m s^{-1} (5 %–15 % variance explained) at both moorings. The temperature record at MW also shows strong seasonality. The amplitude of the annual sinusoidal fit to the temperature time series increases from 0.6 °C at 200–300 m to 1 °C at 500–600 m, accounting for 60 %–70 % of the variance, and rapidly decays deeper.

The largest along-isobath currents reach 0.8 m s^{-1} at both moorings, last for 1 to 2 weeks and extend as deep as 600 m. In periods with strong u, the cross-isobath velocity is also energized. These energetic periods also correspond to the peaks in EKE_g obtained from satellite altimetry at the MW location (Fig. 3c). Isotherms (available only at MW for the entire mooring record) show vertical displacements of the order of 100 m, consistent with mesoscale meandering of the slope current.

For comparison, in the Svinøy section Skagseth and Orvik (2002) showed that the fluctuations of the slope current are a combination of longer periodic forced oscillations, which are a direct response to the wind (periods in the 3–5 and 16–32 d bands), and free waves corresponding to the first and second topographic wave modes (dominant periods of 40–70 and 80–110 h).

We analyzed fluctuations in the low-passed fields relative to the annual cycle to assess dominant timescales and amplitudes of variability. The time series of fluctuations of u at MN averaged between 200 and 300 m shows 13 events with a peak-to-peak amplitude of 0.2–0.3 m s^{-1} and a mean duration of 8 ± 2 d at an average interval (time separation between events) of 35 ± 10 d. Similar numbers of events with a comparable timescale are detected for temperature oscillations exceeding 0.5 °C.

At shorter timescales, the 35 h to 14 d band-passed variability is shown in Fig. 5e–f for u. The structure of band-passed v is very similar (not shown), with approximately half the amplitude of u. The band-passed fields show highly energetic current variability reaching ± 0.4 m s^{-1} (variability for v is ± 0.2 m s^{-1}). A similar event analysis of the fluctuations in the filtered band (averaged between 200 and 300 m at MN and between 300 and 400 m at MW) results in very similar properties for MN and MW. Typically, 40–50 events are detected in u with a peak-to-peak amplitude of 0.15–0.20 m s^{-1} and a mean duration of 2 ± 1 d at an average interval of 10 ± 7 d. The cross-isobath component shows about 40 events

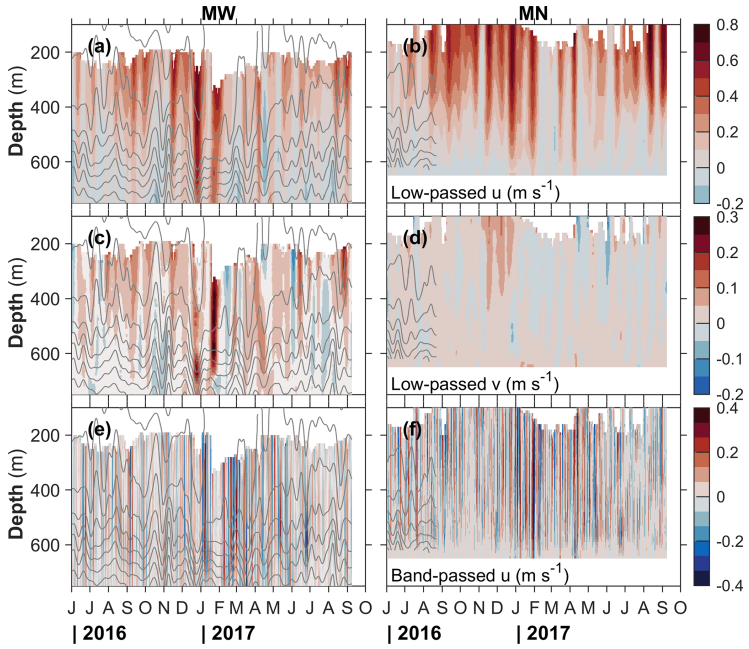

Figure 5. Depth–time variability of observed currents in the 100–700 m depth range at **(a, c, e)** MW and **(b, d, f)** MN. The rows are **(a, b)** low-passed along-isobath current, **(c, d)** low-passed cross-isobath current and **(e, f)** band-passed along-isobath current. The structure of the band-passed cross-isobath (not shown) is similar, with approximately half the amplitude. The variability in the deeper parts of MW is small and not shown for ease of comparison with MN. Isotherms at 1 °C intervals are shown in gray in all panels. Note the lack of water column temperature data after the first 3 months at MN.

with a peak-to-peak amplitude of $0.10 \pm 0.03\,\mathrm{m\,s^{-1}}$ at similar durations and time intervals. The energetics and conversion rates are further discussed in Sect. 8.

We estimated a decorrelation timescale as the e-folding timescale from an exponential fit to the autocorrelation function from hourly velocity time series. At both moorings at the 650 m isobath (MN and MS), the 200–600 m depth-averaged along-isobath currents are correlated at timescales up to 6 d. The decorrelation timescale at MW is comparable (7.3 d). For reference, the advection time between the along-isobath separation of MS and MN is 2 d using the mean speed of $0.15\,\mathrm{m\,s^{-1}}$. Over the 26 km separation, u values at MN and MS are highly coherent, with a maximum correlation coefficient of $r = 0.6$ at a 41 h lag (consistent with the 2 d advection timescale). The cross-isobath components are not significantly correlated. The lateral separation of 5 km between MN and MW is comparable to the Rossby deformation radius; here u is highly coherent ($r = 0.9$ at 8 h lag), and the cross-isobath components are fairly correlated, with $r = 0.24$ at a 2 d timescale with MN leading.

6 Transport

Transport calculations were made with daily averages of the 14 d low-passed current and temperature fields from moorings MW and MN using the along-isobath component of the current. First, transport densities (i.e., transport in a water column with 1 m width) were calculated by integrating vertically between 50 and 650 m depth, roughly corresponding to the AW layer. We extended the shallowest available measurement upward to 50 m, for which near-surface data are missing. The gaps in the velocity and temperature profiles vary between the moorings and are summarized in Sect. 2. A total transport was then estimated by assigning a constant width for each mooring (12.5 km for the outer mooring MW and 7.6 km for the inner mooring MN, justified below). Positive (northeastward, Q_p) and negative (southwestward, Q_n) transport as well as the net transport ($Q_\mathrm{p} + Q_\mathrm{n}$) in 1 °C temperature classes were computed. We estimated the transport of Atlantic Water (Q) as the net transport of water warmer than 5 °C. Average transports over the entire record, over summer months and winter months are listed in Table 2. Results are summarized in Fig. 6.

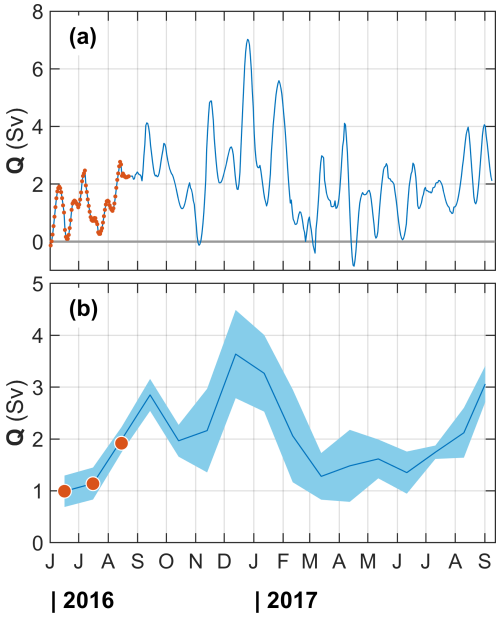

Figure 6. Total AW transport in the 50–650 m range covered with moorings MN and MW, assigning a width of 12.5 km to MW and 7.6 km to MN (see the text for details and sensitivity to choices). AW is defined with $\Theta > 5\,^{\circ}\mathrm{C}$ as measured at MW, which has temperature sensors throughout the deployment. MN has a temperature record in the first 3 months, and the transport calculation using those records (red) agrees with MW. **(a)** Daily transports from 14 d low-passed records and **(b)** monthly averages of the transports shown in **(a)**. The envelope is ± standard error using a decorrelation timescale of 7 d.

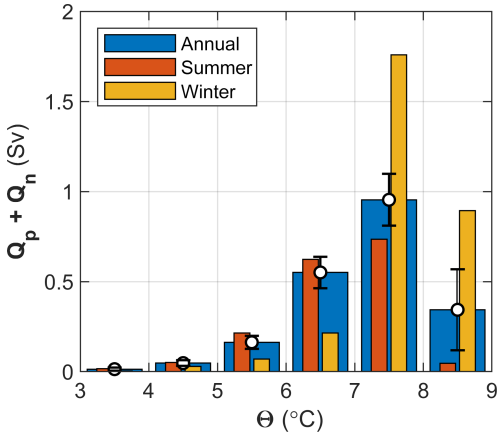

Figure 7. Total net transport ($Q_p + Q_n$) in the 50–650 m depth range averaged into temperature classes for the entire record (annual), summer (JJA) and winter (DJF). Error bars (± standard error) are shown for the annual averages.

The moorings MN and MW are separated by 5.3 km (horizontal distance between the locations), and when projected onto the cross-isobath section the distance is about 5 km (the relative angle between the mooring line orientation and the cross-isobath direction is 20°). We assume that the velocity measured at each mooring is representative for the half-width (2.5 km) to the next mooring. We further extend the width of MW 10 km off-slope (distance to the 2500 m isobath) and MN 10 km onshore (distance to the 250 m isobath). These choices are motivated by the coverage of the dynamic AW core at the Gimsøy section (see Fig. 2). The outer edge corresponds to the location where the 5 °C isotherm is shallowest and covers the relatively steep lateral isopycnal gradient toward the slope. The width of the water column for the outer mooring MW used in the transport calculation is then $10 + 2.5 = 12.5$ km. The width of the inner mooring is $2.5 + 5.1 = 7.6$ km; 5.1 km is an effective width accounting for the shallowing bottom in the 10 km onshore of MN. The resulting cross-sectional area (600 m × 7.6 km) is equivalent to the area between 50 and 650 m depth obtained by integrating the actual topography to 10 km onshore of the 650 m isobath.

The choice of total width for the transport calculation is consistent with the lateral structure of the depth-integrated geostrophic current inferred from the Gimsøy hydrographic section. From the four occupations of the Gimsøy section, we calculated the geostrophic transport relative to surface pressure. Depth-integrated geostrophic current peaks at an isobath between 500 and 750 m, suggesting that MN and MS are positioned near the maximum velocities of the slope current. The lateral structure of the depth-integrated relative geostrophic current was fairly symmetric and reduced to 20 % of its maximum over a total width of 25–30 km. This lateral structure is also consistent with the vertically integrated geostrophic shear from the annual mean climatology discussed later (red contours in Fig. 9a). As a result we find that the choice of cross-isobath width extending between the 2500 and 250 m isobaths for transport calculations is justified.

Two moorings closely spaced over the slope cannot resolve the full dynamics of the slope boundary current. However, the comparison with the Gimsøy section suggests that the dynamic core of the slope current can be captured by the mooring records. The individual occupations of the section show that the bulk of the AW is in the upper 650 m, which is resolved by our moorings. The relative geostrophic transports for AW calculated in the Gimsøy section between 50–650 and 50–1500 m were identical to within 0.1 Sv; hence, the limited vertical range of our transport calculation does not introduce additional errors in the baroclinic contribution.

Table 2. Volume transport calculations. Positive transport, Q_p, is directed northwest out of section, Q_n is southeastward and Q is the total AW transport with $\Theta \geq 5\,^{\circ}$C. n is the degrees of freedom (daily data points divided by a decorrelation time of 7 d). The values in square brackets are $[\pm\sigma; \pm se]$, where σ is the standard deviation, and se is the standard error ($se = \sigma/\sqrt{n}$). Additionally, a total error estimate for Q (see the text) is given.

		Transport (Sv)		
Period	n	Q_p	Q_n	Q
Annual	66	2.1 [±1.3; ±0.2]	−0.1 [±0.1; ±0.0]	2.0 ± 0.8 [±1.3; ±0.2]
Summer	26	1.7 [±1.0; ±0.2]	−0.1 [±0.1; ±0.0]	1.6 ± 0.7 [±0.9; ±0.2]
Summer-16	13	1.5 [±0.8; ±0.2]	−0.1 [±0.1; ±0.0]	1.4 ± 0.6 [±0.7; ±0.2]
Summer-17	13	2.0 [±1.0; ±0.3]	−0.1 [±0.1; ±0.0]	1.9 ± 0.7 [±0.9; ±0.3]
Winter	13	3.0 [±1.9; ±0.5]	−0.0 [±0.1; ±0.0]	2.9 ± 0.9 [±1.9; ±0.5]

Together with the temporal averages and 1 standard deviation, σ, we also report the standard error of the mean and a representative total transport error estimate. The standard error is calculated as $se = \sigma/\sqrt{n}$ using degrees of freedom (n) and taking into account the decorrelation timescale of 7 d (Sect. 5). We calculate a representative transport error estimate for winter, summer and annual data points separately, accounting for the time variability in statistics. At each mooring, we assume root mean squared errors of about 20 % (4 km) in the effective width and 0.05 m s^{-1} in the depth-averaged current (corresponding to 30 m^2 s^{-1} of transport density). A simple calculation using these figures, ignoring the statistics, would lead to an error of 0.12 Sv. Using the mean and σ of the observed transport density (for winter, summer and all data separately), we generate 100 random data points from a normal distribution and calculate the transport (without imposed error) using a 20.1 km width. The distribution of transport is approximately normal in each season, and this assumed distribution for error analysis is justified. We then generate 100 values for transport density and width from a random distribution with imposed errors and calculate the total transport (with error). The root mean squared value of the difference between transport values with and without error from this 100-point realization gives one error estimate. We draw 1000 bootstrap error estimates and average them to obtain the reported error. The transport error is 0.8 Sv for the annual average, 0.7 Sv for summer and 0.9 Sv for winter. This is typically less than the standard deviation and 3–4 times the standard error (Table 2).

There is large variability in Q, with 1 to 4 Sv oscillations at a 2- to 4-week timescale (Fig. 6a). The transport variability can be due to the current meandering outside the moorings rather than a change in the along-isobath transport. Transport maxima were observed in winter. The transport approached zero at the trough of the oscillations, but the flow reversal was negligible. Total AW transport was typically northward. The monthly averaged transport of AW increased 3-fold in fall and winter, with a monthly average maximum of about 3.6 Sv in December, from about 1–2 Sv in summer (Fig. 6b). The transport in temperature classes is shown in Fig. 7. When averaged over summer and winter months separately, transport in high temperature classes (7–9 °C) was stronger in winter, whilst the low temperature classes (4–7 °C) were stronger in summer. This is because the maximum AW-layer-averaged temperatures occurred in winter (e.g., compare the winter and summer temperature profiles at MW; Fig. 4a) when the transport was also large (Fig. 6). In winter, the vertical mixing of the warm surface layer resulted in a low stratified AW layer of 7–8 °C. The largest transport was in the 7–8 °C water for both seasons. We hypothesize that the largest warm water transport in winter is a consequence of the annual cycle of depth-averaged temperature coinciding with the time of the strongest barotropic currents in winter. Seasonal variability with transport and temperature maxima in winter and minima in the autumn was also observed in the Svinøy section, with an annual cycle amplitude in currents of about 0.10 m s^{-1} (Orvik and Skagseth, 2005).

Statistics of the volume transport are summarized in Table 2. Overall, AW transport averaged over the entire record was 2.0 ± 0.8 Sv (± total error; $\sigma = 1.3$ Sv, $se = 0.2$ Sv). The winter average (2.9 ± 0.9 Sv) was larger than the summer average (1.6 ± 0.7 Sv), which is significant when considering the se but not the total error. Averaged separately, transport was stronger in summer 2017 relative to summer 2016, increasing from 1.4 ± 0.6 to 1.9 ± 0.7 Sv in summer 2017. The difference was significant relative to the se.

The crude estimate of the width of the slope current must be treated with caution. The sensitivity to the choice of mooring width is approximately linear. Reducing the total effective width by a factor of 2, to 10 km, reduces the mean AW transport from 2.0 to 1.0 Sv. AW transports, on the other hand, are not sensitive to the definition of the AW temperature and vertical integration limits. Recalculating the transport using water with $\Theta \geq 3$ (instead of $\Theta \geq 5$) increases Q by less than 0.1 Sv. While the upper layers are characterized by lower-salinity water, the proportion of AW entrained into the upper 50 m should ideally be accounted for in the AW transport estimates. In the core of the slope current between MN and MW, salinity from the hydrographical atlas vertically averaged in the upper 50 m varies between 35.25 and

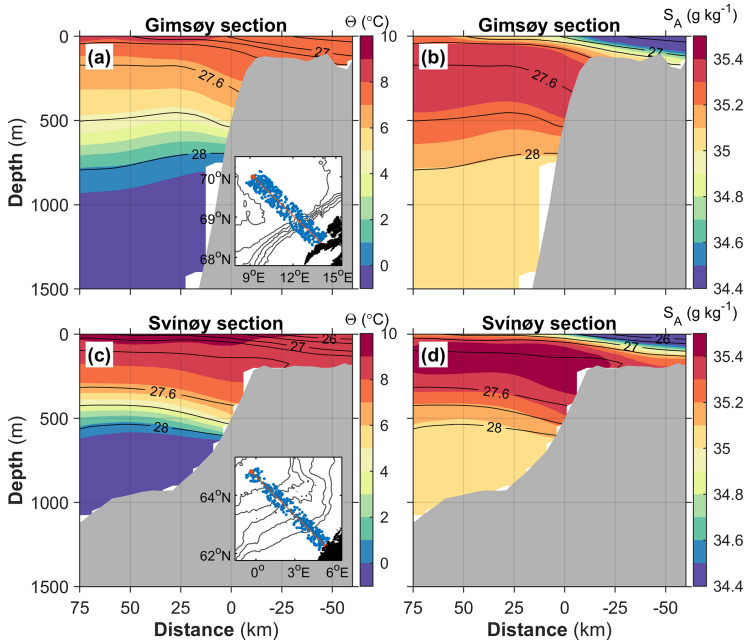

Figure 8. Mean **(a–c)** Θ and **(b–d)** S_A distribution along the Gimsøy and Svinøy sections obtained from the Nordic Seas data set (Bosse and Fer, 2018). The contour interval is 1 °C for Θ and 0.1 g kg^{-1} for S_A. Salinity is saturated at 34.4 g kg^{-1}, but minimum values are 33.0 at Svinøy and 33.9 at Gimsøy. Isopycnals (potential density anomaly referenced to surface pressure, σ_0; black) are drawn at 0.2 kg m^{-3} intervals to 27 kg m^{-3}, followed by 26.5 and 26 kg m^{-3} for shelf waters. An inset map for each section shows the profiles used, located within 25 km of distance from the sections. Distance is referenced to the 500 m isobath.

34.95 g kg^{-1} (not shown). Assuming shelf waters of salinity less than 34 g kg^{-1}, the fraction of AW in the mixed water would exceed 65 % to 80 %. We limit our estimates at 50 m mainly because of a lack of reliable current measurements. Including the upper 50 m by extending the uppermost available current measurement to the surface and assuming a 100 % AW fraction increases the total mean transport by 0.3 Sv (from 2.0 Sv), well within the error estimates.

7 Climatological structure and comparison with the Svinøy section

There is a substantial transformation of AW between the Svinøy (63° N) and Gimsøy (69° N) sections, discussed in detail by Bosse et al. (2018). Analyses in temperature–salinity space of isopycnal layers described how and where AW was progressively transformed to denser isopycnals. While the most important transformation occurred in the western part of the Lofoten Basin, lateral exchanges generated by instabilities of the slope current substantially modified the characteristics of the AW transported from the Svinøy to Gimsøy section. A climatological view of the hydrography shows the important poleward cooling and freshening of AW (Fig. 8). As the AW is modified, isopycnals with a potential density anomaly σ_0 less than 27.7 kg m^{-3} rise. At the core of the slope current, the displacement of the 27.5 isopycnal reaches 150 m, switching from being located below the AW core to above. This isopycnal layer is also where the largest spiciness injection – an indicator of water mass transformation by diapycnal mixing – was reported (Bosse et al., 2018). Deeper isopycnals sink from Svinøy to Gimsøy, which could be related to the intermediate waters subducted along the Mohn Ridge front and AW transformations in the Lofoten Basin, decreasing the stratification in the AW pycnocline. As a result of winter mixing driven by intense air–sea fluxes, the AW pycnocline in the Lofoten Basin is more diffuse and deeper at around 800 m (vs. 500 m farther south). The cross-isobath temperature and salinity gradients across the slope current also exhibit a different structure, suggesting different contributions to geostrophic currents (via thermal wind balance) and a change with latitude in the baroclinicity of the slope current (Fig. 9).

The cross-isobath gradients are relatively weaker at Gimsøy compared to the Svinøy section, and so are the temperature contribution (positive at the slope, negative on the shelf)

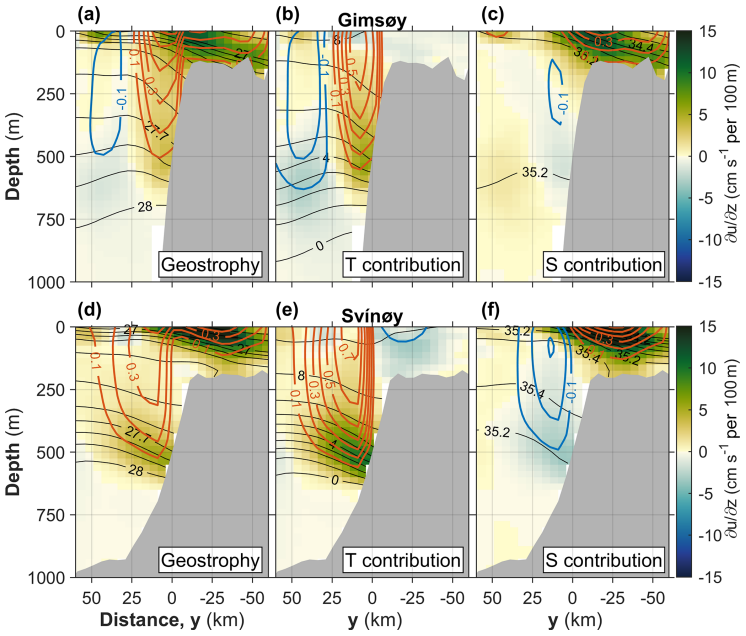

Figure 9. Vertical shear from thermal wind balance for the **(a, b, c)** Gimsøy and **(d, e, f)** Svinøy sections using the annual mean hydrography shown in Fig. 8. Panels **(a)** and **(d)** are the total geostrophic shear, panels **(b)** and **(e)** are the thermal contribution, and panels **(c)** and **(f)** are the haline contribution to shear. Vertically integrated shear is also contoured (blue: negative; red: positive values). Distance is referenced to the 500 m isobath. Isolines are drawn at 0.1 kg m^{-3} for σ_0 (down to 27 kg m^{-3} and with additional 26.5 and 26 kg m^{-3} contours), 1 °C for Θ, 0.2 g kg^{-1} for S_A and 0.1 m s^{-1} for vertically integrated shear.

and haline contribution (negative at the slope, positive on the shelf) to the geostrophic shear (Fig. 9). Furthermore, the coastal current core – identified by the positive shear driven by salinity on the shelf – interacts more strongly with the slope current at Gimsøy. This can be explained by the steeper slope of the Lofoten Escarpment, which has a stronger control on the mean position of the slope current. Note that the broader region of isopycnal gradients at Svinøy does not necessarily imply a broader current but could result from a more variable position linked to a weaker steepness of the slope.

To further compare the baroclinicity of the slope current at these two locations, we vertically integrated the different contributions to the geostrophic shear with a level of no motion at the bottom (geostrophic velocity contours in Fig. 9). The baroclinicity of the slope current indeed increases with latitude: poleward geostrophic currents exceed 0.6 m s^{-1} at Gimsøy compared to about 0.4 m s^{-1} at Svinøy, despite the stronger contribution from vertically integrated shear due to temperature (0.75 m s^{-1} at Svinøy vs. 0.56 m s^{-1} at Gimsøy). A strong negative shear due to salinity counterbalances the thermally driven geostrophic shear of the current at Svinøy (reaching -0.31 m s^{-1} integrated from the bottom to 150 m and -0.25 m s^{-1} to the surface). At Gimsøy, this value reaches only -0.12 m s^{-1} from the bottom to 250 m and becomes insignificant when integrated to the surface. This suggests that the cross-isobath salinity gradient is important for the baroclinicity of the slope current, even in a region where temperature accounts for most of the density variations. Changes in the baroclinicity of the slope current can thus be expected following AW salinity interannual variability (e.g., important freshening observed recently by Mork et al., 2019).

8 Energetics

The kinetic energy content and variability of the slope current, as well as conversion rates associated with the barotropic and baroclinic instability of the current, are presently unconstrained by observations. Using our limited mooring records, we attempt to quantify the energetics of the slope current at the Lofoten Escarpment. For the following analysis, we obtained the fluctuations, denoted by primes, by band-pass filtering the hourly data with cutoff frequencies corresponding to 35 h and 14 d.

We start with the variability in depth-averaged along- and cross-isobath currents, the horizontal eddy kinetic energy density, EKE, and their relation to wind forcing. The EKE (J kg^{-1} or m^2 s^{-2}) is

$$\mathrm{EKE} = \frac{1}{2}\left(u'^2 + v'^2\right). \quad (1)$$

The along-isobath current variability and the evolution of EKE were partly forced by the along-isobath wind modulating the geostrophic shear by cross-front Ekman transport (Fig. 10a–c). The annual average wind speed was 4.3 ± 2.3 m s^{-1} (in this section the figures after "±" are 1σ). In winter, the average and maximum wind speed values were 6 and 11 m s^{-1}, respectively. Depth-averaged (200–600 m) u at MW was 0.15 ± 0.12 m s^{-1}, with a maximum of 0.6 m s^{-1} in winter (winter average was 0.25 ± 0.16 m s^{-1}). The maximum correlation between depth-averaged u and the along-isobath component of the wind W_x was obtained at a 2 d lag ($r = 0.6$). While no significant correlation was detected with the cross-isobath component, v increased in amplitude and variability in winter (from its annual average of 0.03 ± 0.04 m s^{-1}) to 0.05 ± 0.07 m s^{-1}, reaching a maximum of 0.26 m s^{-1}.

From 30 d moving averages, EKE was $(65 \pm 38) \times 10^{-4}$ m^2 s^{-2}, with a maximum of 185×10^{-4} m^2 s^{-2}. Daily average values were similar but with a 3 times larger standard deviation and a maximum of 790×10^{-4} m^2 s^{-2}. The maximum EKE was observed in winter, consistent with stronger and favorable downfront winds. When averaged over winter months EKE was $(100 \pm 41) \times 10^{-4}$ m^2 s^{-2}.

An estimate of the baroclinic (BC) and barotropic (BT) conversion rates can be made by assuming no variability in the along-isobath direction and that the cross-isobath gradients dominate. Similar calculations were made in both idealized (channel) model studies (e.g., Spall et al., 2008) and using mooring array data in the West Spitsbergen Current (von Appen et al., 2016), in the East Greenland Current (Håvik et al., 2017), and across the boundary current at the Beaufort shelf break and slope (Spall et al., 2008). A positive value of BC indicates conversion from mean potential energy into EKE by growing eddies extracting energy from the mean state. The conversion from mean kinetic energy into EKE is quantified by BT. In this case, the kinetic energy is extracted from the mean flow by eddies transporting along-isobath momentum down the mean velocity gradient (e.g., Spall et al., 2008). The baroclinic conversion rate can be approximated by

$$\mathrm{BC} = g\overline{v'\rho'}\frac{\partial z}{\partial y}, \quad (2)$$

where the cross-isobath velocity fluctuation v' and the density fluctuation ρ' are obtained by 35 h–14 d band-pass filtering the hourly data; $\rho_0 = 1027$ kg m^{-3} is a reference density, g is gravitational acceleration, and we applied a temporal averaging (overbar) using 30 d moving averaging. The mean isopycnal slope, $\partial z/\partial y$, was calculated as $(\partial\overline{\rho}/\partial y)/(\partial\overline{\rho}/\partial z)$. The barotropic conversion rate can be approximated by

$$\mathrm{BT} = -\rho_0\overline{u'v'}\frac{\partial \overline{u}}{\partial y}. \quad (3)$$

As in the BC calculations, fluctuations are the 35 h–14 d band-passed hourly data, and time averaging is over 30 d. While the velocity data coverage is good in both moorings, density (through salinity measurement) measurements are limited. At MW, density measurements are available at target depths of 75, 380, 980 and 1476 m. At MN, the near-bottom sensor (648 m) recorded throughout, but the sensors at 165 and 455 m recorded only until September (the water column line was cut 3 months after the deployment). Note that motion-corrected mooring data were gridded and interpolated. Based on the density measurement coverage, we picked the 400 m level as a representative depth (in AW and in the wedge of the AW current with steep isopycnals; Fig. 2) at which we can obtain vertical and lateral gradients but only for 3 months into the record. We calculated the vertical gradient at 400 m at MW using the records at 300 and 500 m

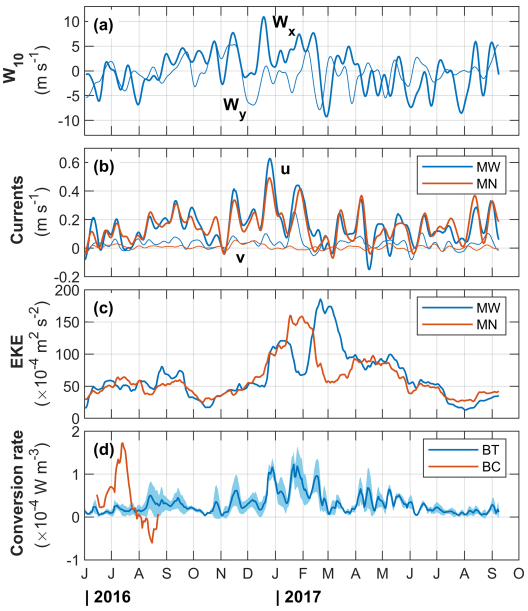

Figure 10. Time series of **(a)** ERA5 wind along-isobath (W_x) and cross-isobath (W_y) components, **(b)** 200–600 m averaged u and v measured at mooring MW (blue) and MN (red), **(c)** 200–600 m averaged EKE at MW (blue) and MN (red), and **(d)** barotropic (BT, blue) and baroclinic (BC, red) conversion rates. BC is at the 400 m level and only available for 3 months. BT is the depth average and 1 standard deviation envelope over calculations at 200, 300, 400, 500 and 600 m. All curves are 30 d moving averages.

and the lateral gradient from the records at 400 m. Whilst the baroclinic conversion rate time series is limited only to 3 months, the barotropic conversion rate can be calculated for the entire duration. We computed BT at 300, 400, 500 and 600 m depths. Results are summarized in Fig. 10d.

The average barotropic conversion rate (averaged over both moorings, over multiple levels and over 14 months) was $(0.3\pm0.2)\times10^{-4}\,\mathrm{W\,m^{-3}}$. The maximum value reached $1.2\times10^{-4}\,\mathrm{W\,m^{-3}}$. The baroclinic conversion rate (only available in the summer for the first 3 months of the mooring period) was comparable at $(0.4\pm0.6)\times10^{-4}$, with a maximum of $1.7\times10^{-4}\,\mathrm{W\,m^{-3}}$. For reference, a conversion rate of $10^{-4}\,\mathrm{W\,m^{-3}}$ for 1 d accounts for ρ_0 EKE of $O(10)\,\mathrm{J\,m^{-3}}$ or EKE of $O(100)\times10^{-4}\,\mathrm{m^2\,s^{-2}}$.

Observed EKE and the conversion rates at the Lofoten Escarpment can be compared to other relevant observations. In Fram Strait von Appen et al. (2016) analyzed 12-year-long time series from moorings with a focus on the West Spitsbergen Current. EKE at 75 m depth was $50\times10^{-4}\,\mathrm{m^2\,s^{-2}}$ in summer and increased to $200\times10^{-4}\,\mathrm{m^2\,s^{-2}}$ in winter. At 250 m depth the magnitude was approximately reduced to half. These values, overall, are similar to the EKE at the Lofoten slope. In terms of baroclinic and barotropic conversion rates, the two sites are also comparable: in the West Spitsbergen Current BT was on the order of $0.1\times10^{-4}\,\mathrm{W\,m^{-3}}$, and BC at 75 m was $0.5\times10^{-4}\,\mathrm{W\,m^{-3}}$ in summer, increasing to $1.5\times10^{-4}\,\mathrm{W\,m^{-3}}$ in winter. Summer mean and maximum values are identical (within measurement uncertainties) to the corresponding values from our observations at 400 m in summer.

Using a mooring array Håvik et al. (2017) analyzed the structure and variability of the shelf break East Greenland Current for the period September 2011 to August 2012. EKE at 100 m was up to $700\times10^{-4}\,\mathrm{m^2\,s^{-2}}$ in November 2011 when a reversal of shelf break current was observed; otherwise, typical values varied between 10×10^{-4} and $100\times10^{-4}\,\mathrm{m^2\,s^{-2}}$, similar to the values at the Lofoten Escarpment. Ignoring the energetic reversal event, BT at 100 m was on the order of $0.1\times10^{-4}\,\mathrm{W\,m^{-3}}$ and BC varied in the range of $(1–5)\times10^{-4}\,\mathrm{W\,m^{-3}}$; both conversion rates are similar to those in the West Spitsbergen Current and the slope current.

The conversion rates calculated from our moorings may not be representative of the volume-averaged conversion rates over the slope region. In order to assess this, we compare the observations to high-resolution numerical model results in Sect. 9.

9 Conversion rates from a high-resolution model

In order to better interpret the conversion rates obtained from moorings, we calculate volume-averaged conversion rates in the region using the outputs from high-resolution ROMS runs (Sect. 2.2). We first compute the baroclinic and barotropic conversion rates over a domain covering the slope region identified in Fig. 11. The conversion rates in a 3D, right-handed coordinate system are formulated in Olbers et al. (2012, pp. 376–377). The baroclinic conversion rates are computed from

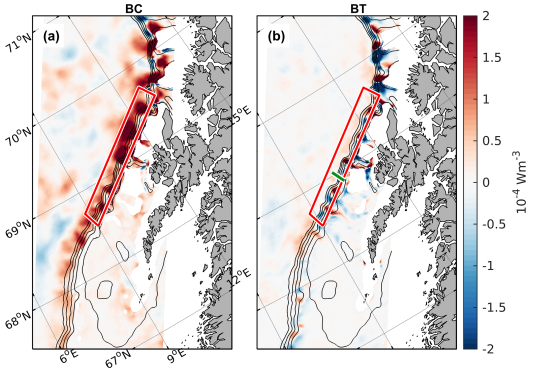

Figure 11. Maps of **(a)** baroclinic and **(b)** barotropic conversion rates averaged over 1 year (1999) between 100 and 1000 m depth or to the bottom in shallower areas. Longitudes and latitudes are identical in both panels and are only labeled in **(a)**. The red box is the slope region where the volume-averaged conversion rates shown in Fig. 12a are computed. The green line across the slope in **(b)** marks a segment across the mooring positions used for the comparison of the volume average with segment and virtual mooring calculations (see the text and Fig. 12b). Black contours show the 200, 400, 600, 800 and 1000 m isobaths.

$$\mathrm{BC} = -\rho_0\overline{\boldsymbol{u}'b'}\cdot\nabla\overline{b}/N^2 = g\left(\frac{\partial\overline{\rho}}{\partial z}\right)^{-1}\left(\overline{u'\rho'}\frac{\partial\overline{\rho}}{\partial x}+\overline{v'\rho'}\frac{\partial\overline{\rho}}{\partial y}\right). \quad (4)$$

Here $\boldsymbol{u}=(u,v)$ is the horizontal velocity field (the formulation is valid for both the model grid and the along- and cross-isobath rotated coordinate system), $b=-g\rho/\rho_0$ is the buoyancy, $N^2=-\frac{g}{\rho_0}\frac{\partial\overline{\rho}}{\partial z}$ is the buoyancy frequency, ρ is the potential density referenced to the surface, g is the gravitational acceleration and $\rho_0=1027\,\mathrm{kg\,m^{-3}}$ is a reference density. The primes denote deviations from an average state (overbar), averaged over multiple eddy timescales, e.g., for velocity $u'=u-\overline{u}$. A positive value of BC indicates a transfer of potential energy from the mean flow to eddies.

We calculate the barotropic conversion rates from

$$\begin{aligned}\mathrm{BT} &= -\rho_0\left(\overline{u'\boldsymbol{u}'}\cdot\nabla\overline{u}+\overline{v'\boldsymbol{u}'}\cdot\nabla\overline{v}\right)\\ &= -\rho_0\left(\overline{u'u'}\frac{\partial\overline{u}}{\partial x}+\overline{u'v'}\left(\frac{\partial\overline{u}}{\partial y}+\frac{\partial\overline{v}}{\partial x}\right)+\overline{v'v'}\frac{\partial\overline{v}}{\partial y}\right). \quad (5)\end{aligned}$$

A positive value of BT indicates a transfer of kinetic energy from the mean flow to eddies.

We compute BC and BT after interpolating the model fields to uniform z levels of 10 m vertical spacing. The time averaging is calculated over monthly windows to avoid any

seasonal bias in the eddy fluxes. We arbitrarily chose the year 1999 from the model fields (available from 1996 to the end of 1999). Monthly conversion rates are then averaged vertically between 100 and 1000 m depth (i.e., we exclude the near-surface variability). A global annual average is then obtained by averaging over these 12 months. Results are shown in Fig. 11.

The baroclinic conversion rates are typically positive and largest along the slope, indicating that potential energy is extracted from the slope current to feed eddies that are generated there. The barotropic conversion rates, on the other hand, show larger spatial variability, with smaller amplitudes and abrupt sign changes along the slope. The baroclinic processes therefore appear to be the main contributor to the conversion of energy from the mean flow to eddies along the slope.

Monthly conversion rates over the slope, volume-averaged over the red box identified in Fig. 11a and between 100 and 1000 m depth, show that the baroclinic conversion rates dominate (Fig. 12a), implying that the baroclinic instability of the slope current extracts energy from the mean flow to eddies.

The motivation here is to assess whether the conversion rates obtained from a mooring array are representative of the volume-averaged values. To do this we define a segment across the slope (green in Fig. 11b) that stretches between the mooring positions of MW and MN and extend it further by 10 km at both sides. We then perform two types of calculations: (1) we compute BT and BC at the model grid resolution and average along the entire segment, and (2) we compute BT and BC using model data from the virtual mooring positions. To be consistent with the observations we apply Eqs. (2)–(3), rotate the coordinate system to along and across isobaths, calculate BC only at 400 m depth, and vertically average BT between 200 and 600 m. The motivation of performing the segment calculation is to better resolve the lateral shear (based on about 40 grid points compared to only two virtual moorings). The conversion rates are shown in Fig. 12b.

While there are differences between the segment and virtual mooring estimates (Fig. 12b), the conversion rates are comparable, with no systematic differences. Lateral shear and isopycnal slopes using only two moorings separated by about 5 km could thus be used in calculations of the conversion rates in one transect. We also note that BT is similar to the observations (blue line in Fig. 10d), with magnitudes of $(0–1)\times10^{-4}\,\mathrm{W\,m^{-3}}$ and maximum values around $1\times10^{-4}\,\mathrm{W\,m^{-3}}$. Observed BC is available only in the summer months (red line in Fig. 10d) and compares fairly well with the BC from virtual moorings. However, a comparison with the volume-averaged conversion rates shows that calculations using virtual moorings alone overestimate BT, underestimate BC, introduce spurious changes in sign and are not representative of the overall conversion rates on the slope.

The discrepancy in BT is partly due to the different depth averaging (100 to 1000 m vs. 200 to 600 m; note that the lat-

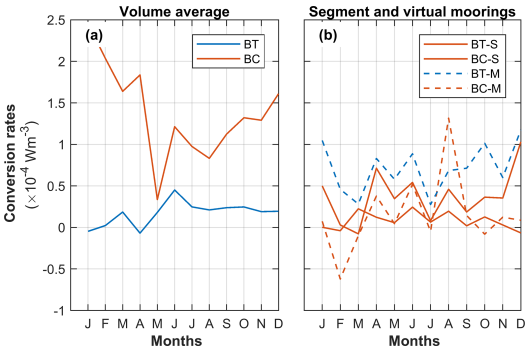

Figure 12. Monthly averaged barotropic (blue) and baroclinic (red) conversion rates **(a)** vertically averaged between 100 and 1000 m depth inside the red box in Fig. 11 and **(b)** along a segment across the slope (green line in Fig. 11b) using model horizontal resolution (BT-S and BC-S, solid lines) and using two virtual moorings (BT-M and BC-M, dashed lines). Calculations were made using Eqs. (4)–(5) in **(a)** and using Eqs. (2)–(3) in **(b)**. The baroclinic conversion rates in **(b)** are shown at 400 m depth, whereas the barotropic conversion rates are averaged between 200 and 600 m depth, i.e., directly comparable to the observations.

ter range is constrained by available observations, whereas the former covers the depth range of interest on the slope region, excluding the upper surface processes) and partly because the volume-averaged calculations include the divergent terms (first and last term in Eq. 5) in addition to the terms related to shear (second term). The highly variable spatial structure observed in BT cannot be resolved with a high-resolution single segment or a couple of moorings. Furthermore, volume averaging over BT with changing signs leads to a negligible average BT, which cannot be resolved with the moorings. The discrepancy in BC is mainly because the volume-averaged calculations are based on a depth average between 100 and 1000 m, whereas the mooring calculations are only taken at 400 m depth due to limited observations. BC cannot be captured by the calculations from a single level.

Based on the analysis of the model outputs, we conclude that the mooring-derived conversion rates must be interpreted with caution and may not be representative of the real conversion rates in the region. While we cannot confirm using the limited observations, the model results suggest that the average conversion rates on the Lofoten Escarpment are likely dominated by baroclinic instability of the slope current.

10 Summary and conclusions

The Norwegian Atlantic Slope Current at the Lofoten Escarpment is described using 14-month-long mooring records in the period from June 2016 to September 2017. Despite the limited number of moorings, the observations resolve the

core of the current from 200 to 650 m depth over the shelf break and the upper continental slope. The data set represents the first moored observations on a yearly timescale from this region and offers important constraints on the mean properties, transport rates, temporal variability and energy conversion rates of the slope current.

The 200–600 m averaged current shows an annual cycle with an amplitude of $0.1\,m\,s^{-1}$, with the strongest currents in winter, and has a temporal average of $0.15\,m\,s^{-1}$. The 14 d low-pass-filtered along-isobath currents reach $0.8\,m\,s^{-1}$, lasting for 1 to 2 weeks, and extend as deep as 600 m. The variability in the along-isobath current is partly forced by the along-isobath wind stress, with a maximum correlation of 0.6 at a 2 d lag. In contrast to observations in Svinøy, the slope current is not barotropic and varies strongly with depth (shear of 0.05 to $0.1\,m\,s^{-1}$ per 100 m in all seasons).

The average volume transport of Atlantic Water is 2.0 ± 0.8 Sv, with summer and winter averages of 1.6 ± 0.7 and 2.9 ± 0.9 Sv, respectively. The largest transport is associated with warm water in all seasons, and the water temperatures are the highest in winter.

Calculations of the barotropic and baroclinic conversion rates from the moorings are supplemented by results from a high-resolution numerical model. While the conversion from mean kinetic energy into eddy energy (e.g., barotropic instability) is likely negligible over the Lofoten Escarpment, the baroclinic conversion from mean potential energy into eddy kinetic energy (e.g., baroclinic instability) can be substantial, with volume-averaged values on the order of $10^{-4}\,W\,m^{-3}$. Eddy kinetic energy and conversion rates in the slope current are comparable to the published results from the West Spitsbergen Current and the East Greenland Current.

Fishing activity in the region makes it highly challenging to maintain moorings; however, extended time series with better cross-isobath and vertical coverage are needed to study the dynamics and variability of the slope current. The attempts to calculate (observation-based) energy conversion rates remain inconclusive. The utilization of autonomous underwater vehicles, such as gliders, can help collect high-quality observations but will be difficult to operate in the strong boundary current. The slope current and its instability are important players in the energetics of the Lofoten Basin and merit further studies.

Data availability. Mooring data used in this analysis are available from Fer (2020) and at https://doi.org/10.21335/NMDC-1664980441 through the Norwegian Marine Data Centre with a Creative Commons Attribution 4.0 International License. The data set of the Nordic Seas (Bosse and Fer, 2018) is available from https://doi.org/10.21335/NMDC-1131411242 through the Norwegian Marine Data Centre with a Creative Commons Attribution 4.0 International License. Other environmental data are obtained using the Copernicus Climate Change Service (2017) and European Centre for Medium-Range Weather Forecasts (ECMWF). Sea level anomaly data are obtained from the EU Copernicus Marine Service Information, product SEALEVEL_GLO_PHY_L4_REP_OBSERVATIONS_008_047.

Author contributions. IF conceived the experiment, processed and analyzed the mooring data, and wrote the paper. AB extracted and analyzed the surface forcing and the Nordic Seas climatology data. JD calculated conversion rates from existing model fields. All authors contributed to interpreting and discussing the results and reviewing the paper.

Competing interests. Ilker Fer is a member of the editorial board of *Ocean Science*, but other than that the authors declare no competing interests.

Acknowledgements. This study received funding from the Research Council of Norway through the project "Water mass transformation processes and vortex dynamics in the Lofoten Basin in the Norwegian Sea (PROVOLO)" (project 250784). The ROMS simulation was made by Marta Trodahl and Nils M. Kristensen of the Norwegian Meteorological Institute and run on resources provided by UNINETT Sigma2 – the National Infrastructure for High Performance Computing and Data Storage in Norway. We thank the crew and participants of the deployment and recovery cruises, particularly Helge Bryhni, Algot Peterson and Henrik Søiland for their help with the mooring work. We thank Kjell Arild Orvik for making available the Svinøy mooring data used in the discussion forum. Insightful and constructive comments from Michael A. Spall and two anonymous reviewers helped improve the discussion version of this paper.

Financial support. This research has been supported by the Norges Forskningsråd (grant no. 250784).

Review statement. This paper was edited by Mario Hoppema and reviewed by Michael A. Spall and two anonymous referees.

References

Andersson, M., Orvik, K. A., LaCasce, J. H., Koszalka, I., and Mauritzen, C.: Variability of the Norwegian Atlantic Current and associated eddy field from surface drifters, J. Geophys. Res., 116, C08032, https://doi.org/10.1029/2011jc007078, 2011.

Bosse, A. and Fer, I.: Hydrography of the Nordic Seas, 2000–2017: A merged product, Norwegian Marine Data Centre, https://doi.org/10.21335/NMDC-1131411242, 2018.

Bosse, A. and Fer, I.: Mean structure and seasonality of the Norwegian Atlantic Front Current along the Mohn Ridge from repeated glider transects, Geophys. Res. Lett., 46, 13170–13179, https://doi.org/10.1029/2019gl084723, 2019.

Bosse, A., Fer, I., Søiland, H., and Rossby, T.: Atlantic Water Transformation Along Its Poleward Pathway Across

the Nordic Seas, J. Geophys. Res., 123, 6428–6448, https://doi.org/10.1029/2018JC014147, 2018.

Bosse, A., Fer, I., Lilly, J., and Søiland, H.: Dynamical controls on the longevity of a non-linear vortex: The case of the Lofoten Basin Eddy, Sci. Rep.-UK, 9, 13448, https://doi.org/10.1038/s41598-019-49599-8, 2019.

Copernicus Climate Change Service (C3S): ERA5: Fifth generation of ECMWF atmospheric reanalyses of the global climate, Copernicus Climate Change Service Climate Data Store (CDS), available at: https://cds.climate.copernicus.eu/cdsapp#!/home (last access: 2 February 2019), 2017.

Dee, D. P., Uppala, S. M., Simmons, A. J., Berrisford, P., Poli, P., Kobayashi, S., Andrae, U., Balmaseda, M. A., Balsamo, G., Bauer, P., Bechtold, P., Beljaars, A. C., van de Berg, L., Bidlot, J., Bormann, N., Delsol, C., Dragani, R., Fuentes, M., Geer, A. J., Haimberger, L., Healy, S. B., Hersbach, H., Hólm, E. V., Isaksen, L., Kållberg, P., Köhler, M., Matricardi, M., Mcnally, A. P., Monge-Sanz, B. M., Morcrette, J. J., Park, B. K., Peubey, C., de Rosnay, P., Tavolato, C., Thépaut, J. N., and Vitart, F.: The ERA-Interim reanalysis: Configuration and performance of the data assimilation system, Q. J. Roy. Meteor. Soc., 137, 553–597, https://doi.org/10.1002/qj.828, 2011.

Dugstad, J., Fer, I., LaCasce, J., Sanchez de La Lama, M., and Trodahl, M.: Lateral Heat Transport in the Lofoten Basin: Near-Surface Pathways and Subsurface Exchange, J. Geophys. Res., 124, 2992–3006, https://doi.org/10.1029/2018jc014774, 2019a.

Dugstad, J. S., Koszalka, I. M., Isachsen, P. E., Dagestad, K.-F., and Fer, I.: Vertical Structure and Seasonal Variability of the Inflow to the Lofoten Basin Inferred From High-Resolution Lagrangian Simulations, J. Geophys. Res., 124, 9384–9403, https://doi.org/10.1029/2019jc015474, 2019b.

European Centre for Medium-Range Weather Forecasts (ECMWF): The ERA-Interim reanalysis dataset, Copernicus Climate Change Service (C3S), available at: https://www.ecmwf.int/en/forecasts/datasets/archive-datasets/reanalysis-datasets/era-interim (last access: 2 February 2019), 2011.

Fer, I.: Physical oceanography data from moorings in the Lofoten Basin, Norwegian Sea: June 2016–September 2017, Dataset, Norwegian Marine Data Centre, https://doi.org/10.21335/NMDC-1664980441, 2020.

Fer, I., Bosse, A., Ferron, B., and Bouruet-Aubertot, P.: The dissipation of kinetic energy in the Lofoten Basin Eddy, J. Phys. Oceanogr., 48, 1299–1316, https://doi.org/10.1175/JPO-D-17-0244.1, 2018.

Haidvogel, D. B., Arango, H., Budgell, W. P., Cornuelle, B. D., Curchitser, E., Di Lorenzo, E., Fennel, K., Geyer, W. R., Hermann, A. J., Lanerolle, L., Levin, J., McWilliams, J. C., Miller, A. J., Moore, A. M., Powell, T. M., Shchepetkin, A. F., Sherwood, C. R., Signell, R. P., Warner, J. C., and Wilkin, J.: Ocean forecasting in terrain-following coordinates: Formulation and skill assessment of the Regional Ocean Modeling System, J. Comput. Phys., 227, 3595–3624, https://doi.org/10.1016/j.jcp.2007.06.016, 2008.

Håvik, L., Våge, K., Pickart, R. S., Harden, B., Appen, W.-J. v., Jonsson, S., and Østerhus, S.: Structure and Variability of the Shelfbreak East Greenland Current North of Denmark Strait, J. Phys. Oceanogr., 47, 2631–2646, https://doi.org/10.1175/jpo-d-17-0062.1, 2017.

Høydalsvik, F., Mauritzen, C., Orvik, K. A., LaCasce, J. H., Lee, C. M., and Gobat, J.: Transport estimates of the Western Branch of the Norwegian Atlantic Current from glider surveys, Deep-Sea Res. Pt. I, 79, 86–95, https://doi.org/10.1016/j.dsr.2013.05.005, 2013.

Isachsen, P. E.: Baroclinic instability and the mesoscale eddy field around the Lofoten Basin, J. Geophys. Res., 120, 2884–2903, https://doi.org/10.1002/2014JC010448, 2015.

Isachsen, P. E., Koszalka, I., and LaCasce, J. H.: Observed and modeled surface eddy heat fluxes in the eastern Nordic Seas, J. Geophys. Res., 117, C08020, https://doi.org/10.1029/2012JC007935, 2012.

Ivanov, V. and Korablev, A. A.: Formation and regeneration of the pycnocline lens in the Norwegian Sea, Russ. Meteorol. Hydrol., 9, 62–69, 1995.

Köhl, A.: Generation and stability of a quasi-permanent vortex in the Lofoten Basin, J. Phys. Oceanogr., 37, 2637–2651, https://doi.org/10.1175/2007JPO3694.1, 2007.

Mork, K. A., Skagseth, Ø., and Søiland, H.: Recent warming and freshening of the Norwegian Sea observed by Argo data, J. Climate, 32, 3695–3705, https://doi.org/10.1175/JCLI-D-18-0591.1, 2019.

Olbers, D., Willebrand, J., and Eden, C.: Ocean Dynamics, Springer Verlag Berlin, Berlin, 2012.

Orvik, K. A. and Niiler, P.: Major pathways of Atlantic water in the northern North Atlantic and Nordic Seas toward Arctic, Geophys. Res. Lett., 29, 1896, https://doi.org/10.1029/2002GL015002, 2002.

Orvik, K. A. and Skagseth, Ø.: Monitoring the Norwegian Atlantic slope current using a single moored current meter, Cont. Shelf Res., 23, 159–176, https://doi.org/10.1016/S0278-4343(02)00172-3, 2003.

Orvik, K. A. and Skagseth, Ø.: Heat flux variations in the eastern Norwegian Atlantic Current toward the Arctic from moored instruments, 1995–2005, Geophys. Res. Lett., 32, L14610, https://doi.org/10.1029/2005gl023487, 2005.

Orvik, K. A., Skagseth, Ø., and Mork, M.: Atlantic inflow to the Nordic Seas: current structure and volume fluxes from moored current meters, VM-ADCP and SeaSoar-CTD observations, 1995–1999, Deep-Sea Res. Pt. I, 48, 937–957, https://doi.org/10.1016/S0967-0637(00)00038-8, 2001.

Poulain, P. M., Warn-Varnas, A., and Niiler, P. P.: Near-surface circulation of the Nordic seas as measured by Lagrangian drifters, J. Geophys. Res., 101, 18237–18258, https://doi.org/10.1029/96JC00506, 1996.

Rhines, P., Häkkinen, S., and Josey, S. A.: Is Oceanic Heat Transport Significant in the Climate System?, in: Arctic-Subarctic Ocean Fluxes: Defining the Role of the Northern Seas in Climate, edited by: Dickson, R. R., Meincke, J., and Rhines, P., 87–109, Springer Netherlands, Dordrecht, 2008.

Richards, C. G. and Straneo, F.: Observations of water mass transformation and eddies in the Lofoten Basin of the Nordic Seas, J. Phys. Oceanogr., 45, 1735–1756, https://doi.org/10.1175/JPO-D-14-0238.1, 2015.

Rossby, T., Ozhigin, V., Ivshin, V., and Bacon, S.: An isopycnal view of the Nordic Seas hydrography with focus on properties of the Lofoten Basin, Deep-Sea Res. Pt. I, 56, 1955–1971, https://doi.org/10.1016/j.dsr.2009.07.005, 2009a.

Rossby, T., Prater, M. D., and Søiland, H.: Pathways of inflow and dispersion of warm waters in the Nordic seas, J. Geophys. Res., 114, C04011, https://doi.org/10.1029/2008JC005073, 2009b.

Seager, R., Battisti, D. S., Yin, J., Gordon, N., Naik, N., Clement, A. C., and Cane, M. A.: Is the Gulf Stream responsible for Europe's mild winters?, Q. J. Roy. Meteor. Soc., 128, 2563–2586, https://doi.org/10.1256/qj.01.128, 2002.

Shchepetkin, A. F. and McWilliams, J. C.: Correction and commentary for "Ocean forecasting in terrain-following coordinates: Formulation and skill assessment of the regional ocean modeling system" by Haidvogel et al., J. Comp. Phys. 227, pp. 3595–3624, J. Comput. Phys., 228, 8985–9000, https://doi.org/10.1016/j.jcp.2009.09.002, 2009.

Skagseth, Ø. and Orvik, K. A.: Identifying fluctuations in the Norwegian Atlantic Slope Current by means of empirical orthogonal functions, Cont. Shelf Res., 22, 547–563, https://doi.org/10.1016/S0278-4343(01)00086-3, 2002.

Søiland, H. and Rossby, T.: On the structure of the Lofoten Basin Eddy, J. Geophys. Res., 118, 4201–4212, https://doi.org/10.1002/jgrc.20301, 2013.

Spall, M. A.: Non-local topographic influences on deep convection: An idealized model for the Nordic Seas, Ocean Model., 32, 72–85, https://doi.org/10.1016/j.ocemod.2009.10.009, 2010.

Spall, M. A., Pickart, R. S., Fratantoni, P. S., and Plueddemann, A. J.: Western Arctic Shelfbreak Eddies: Formation and Transport, J. Phys. Oceanogr., 38, 1644–1668, https://doi.org/10.1175/2007jpo3829.1, 2008.

Sundby, S.: Recruitment of Atlantic cod stocks in relation to temperature and advectlon of copepod populations, Sarsia, 85, 277–298, https://doi.org/10.1080/00364827.2000.10414580, 2000.

Volkov, D. L., Kubryakov, A. A., and Lumpkin, R.: Formation and variability of the Lofoten basin vortex in a high-resolution ocean model, Deep-Sea Res. Pt. I, 105, 142–157, https://doi.org/10.1016/j.dsr.2015.09.001, 2015.

von Appen, W.-J., Schauer, U., Hattermann, T., and Beszczynska-Möller, A.: Seasonal Cycle of Mesoscale Instability of the West Spitsbergen Current, J. Phys. Oceanogr., 46, 1231–1254, https://doi.org/10.1175/jpo-d-15-0184.1, 2016.

Bibliography

Andersson, M., K. A. Orvik, J. H. Lacasce, I. Koszalka, and C. Mauritzen (2011), Variability of the Norwegian Atlantic Current and associated eddy field from surface drifters, *Journal of Geophysical Research: Oceans*, *116*(8), 1–16, doi:10.1029/2011JC007078. 1.1

Bashmachnikov, I. L., T. V. Belonenko, P. Kuibin, D. L. Volkov, and V. Foux (2018), Pattern of vertical velocity in the Lofoten vortex (the Norwegian Sea), *Ocean Dynamics*, *68*, 1711–1725, doi:https://doi.org/10.1007/s10236-018-1213-1. 3, 4.3

Benilov, E. (2005), Stability of a two-layer quasigeostrophic vortex over axisymmetric localized topography, *Journal of Physical Oceanography*, *35*, doi:10.1175/JPO-2660.1. 1.2

Bosse, A., and I. Fer (2019a), Mean Structure and Seasonality of the Norwegian Atlantic Front Current Along the Mohn Ridge From Repeated Glider Transects, *Geophysical Research Letters*, *46*(22), 13,170–13,179, doi:10.1029/2019GL084723. 1.1

Bosse, A., and I. Fer (2019b), Mean structure and seasonality of the norwegian atlantic front current along the mohn ridge from repeated glider transects, *Geophysical Research Letters*, *46*(22), 13,170–13,179, doi:10.1029/2019GL084723. 4.3

Bosse, A., I. Fer, H. Søiland, and T. Rossby (2018), Atlantic Water transformation along its poleward pathway across the Nordic Seas, *Journal of Geophysical Research: Oceans*, doi:10.1029/2018JC014147. 1.3, 1.3, 1.4, 2.2.1, 3

Bosse, A., I. Fer, J. Lilly, and H. Søiland (2019), Dynamical controls on the longevity of a non-linear vortex: The case of the Lofoten Basin Eddy, *Scientific Reports*, *9*(13448). 4.3

Bower, A., M. Lozier, and S. Gary (2011), Export of Labrador Sea Water from the subpolar North Atlantic: A Lagrangian perspective, *Deep Sea Research Part II: Topical Studies in Oceanography*, *58*, 1798–1818, doi:10.1016/j.dsr2.2010.10.060. 2.2.2

Broecker, W. S. (1991), The great ocean conveyor, *Oceanography*, *2*(4), 79–89. 1

Broomé, S., L. Chafik, and J. Nilsson (2020), Mechanisms of decadal changes in sea surface height and heat content in the eastern Nordic Seas, *Ocean Science*, *16*(3), 715–728, doi:10.5194/os-16-715-2020. 1.3

Chafik, L., J. Nilsson, Ø. Skagseth, and P. Lundberg (2015), On the flow of atlantic water and temperature anomalies in the nordic seas toward the arctic ocean, *Journal of Geophysical Research: Oceans*, *120*(12), 7897–7918, doi:10.1002/2015JC011012. 1.2

Chinn, B. S., and S. T. Gille (2007), Estimating Eddy Heat Flux from Float Data in the North Atlantic: The Impact of Temporal Sampling Interval, *Journal of Atmospheric and Oceanic Technology*, *24*(5), 923–934, doi:10.1175/JTECH2057.1. 2.2.2

Dagestad, K.-F., and J. Röhrs (2019), Prediction of ocean surface trajectories using satellite derived vs. modeled ocean currents, *Remote Sensing of Environment*, *223*, 130 – 142, doi: https://doi.org/10.1016/j.rse.2019.01.001. 2.2.2

Dagestad, K. F., J. Röhrs, O. Breivik, and B. Ådlandsvik (2018), OpenDrift v1.0: A generic framework for trajectory modelling, *Geoscientific Model Development*, *11*(4), 1405–1420, doi:10.5194/gmd-11-1405-2018. 2.2.2

Davis, R. E. (1991), Observing the general circulation with floats, *Deep Sea Research Part A. Oceanographic Research Papers*, *38*, S531–S571, doi:10.1016/S0198-0149(12)80023-9. 2.2.2

Dee, D. P., S. M. Uppala, A. J. Simmons, P. Berrisford, P. Poli, S. Kobayashi, U. Andrae, M. A. Balmaseda, G. Balsamo, P. Bauer, P. Bechtold, A. C. Beljaars, L. van de Berg, J. Bidlot, N. Bormann, C. Delsol, R. Dragani, M. Fuentes, A. J. Geer, L. Haimberger, S. B. Healy, H. Hersbach, E. V. Hólm, L. Isaksen, P. Kållberg, M. Köhler, M. Matricardi, A. P. Mcnally, B. M. Monge-Sanz, J. J. Morcrette, B. K. Park, C. Peubey, P. de Rosnay, C. Tavolato, J. N. Thépaut, and F. Vitart (2011), The ERA-Interim reanalysis: Configuration and performance of the data assimilation system, *Quarterly Journal of the Royal Meteorological Society*, *137*(656), 553–597, doi:10.1002/qj.828. 2.2.2

Eldevik, T., J. E. Nilsen, D. Iovino, K. A. Olsson, A. Sandø, and H. Drange (2009), Observed sources and variability of nordic seas overflow, *Nature Geoscience*, *2*, doi:10.1038/ngeo518. 1

Fer, I., A. Bosse, B. Ferron, and P. Bouruet-Aubertot (2018), The dissipation of kinetic energy in the Lofoten Basin Eddy, *Journal of Physical Oceanography*, pp. 1299–1316, doi:10.1175/JPO-D-17-0244.1. 1.2, 1.2

Gelderloos, R., T. W. N. Haine, I. Koszalka, and M. Magaldi (2017), Seasonal variability in warm-water inflow towards Kangerdlugssuaq Fjord, *Journal of Physical Oceanography*, *7*(47), 1685–1699, doi:https://doi.org/10.1175/JPO-D-16-0202.1. 2.2.2

Haidvogel, D. B., H. Arango, W. P. Budgell, B. D. Cornuelle, E. Curchitser, E. Di Lorenzo, K. Fennel, W. R. Geyer, A. J. Hermann, L. Lanerolle, J. Levin, J. C. McWilliams, A. J. Miller, A. M. Moore, T. M. Powell, A. F. Shchepetkin, C. R. Sherwood, R. P. Signell, J. C. Warner, and J. Wilkin (2008), Ocean forecasting in terrain-following coordinates: Formulation and skill assessment of the Regional Ocean Modeling System, *Journal of Computational Physics*, *227*(7), 3595–3624, doi:10.1016/j.jcp.2007.06.016. 2.2.2

Huang, J., R. Pickart, R. Huang, P. Lin, A. Brakstad, and F. Xu (2020), Sources and upstream pathways of the densest overflow water in the Nordic Seas, *Nature Communications*, *In review*. 1.1

Huang, R. (2015), Oceanographic topics | thermohaline circulation, in *Encyclopedia of Atmospheric Sciences (Second Edition)*, second edition ed., pp. 315 – 328, Academic Press, Oxford, doi:https://doi.org/10.1016/B978-0-12-382225-3.00281-4. 1.3, 4.2

Isachsen, P., C. Mauritzen, and H. Svendsen (2007), Dense water formation in the Nordic Seas diagnosed from sea surface buoyancy fluxes, *Deep Sea Research Part I: Oceanographic Research Papers*, *54*, 2241, doi:10.1016/j.dsr.2006.09.008. 1.3

Isachsen, P. E. (2015), Baroclinic instability and the mesoscale eddy field aorund the Lofoten Basin, *Journal of Geophysical Research: Oceans*, *120*, 2884–2903, doi:10.1002/2014JC010448-. 1, 1.1, 1.2, 2.2.2, 3

Isachsen, P. E., J. H. LaCasce, C. Mauritzen, and S. Häkkinen (2003), Wind-Driven Variability of the Large-Scale Recirculating Flow in the Nordic Seas and Arctic Ocean, *Journal of Physical Oceanography*, *33*(12), 2534–2550, doi:10.1175/1520-0485(2003)033<2534:WVOTLR>2.0.CO;2. 1.1

Isachsen, P. E., I. Koszalka, and J. H. Lacasce (2012), Observed and modeled surface eddy heat fluxes in the eastern Nordic Seas, *Journal of Geophysical Research: Oceans*, *117*(8), 1–10, doi:10.1029/2012JC007935. 1.2, 1.4, 3

Ivanov, V., and A. A. Korablev (1995), Formation and regeneration of the pycnocline lens in the Norwegian Sea, *Russ. Meteor. Hydrol.*, *9*(9), 62–69. 1.2, 3

Jones, C. E., K.-F. Dagestad, Ø. Breivik, B. Holt, J. Röhrs, K. H. Christensen, M. Espeseth, C. Brekke, and S. Skrunes (2016), Measurement and modeling of oil slick transport, *Journal of Geophysical Research: Oceans*, *121*(10), 7759–7775. 2.2.2

Köhl, A. (2007), Generation and Stability of a Quasi-Permanent Vortex in the Lofoten Basin, *Journal of Physical Oceanography*, *37*(11), 2637–2651, doi:10.1175/2007JPO3694.1. 1.1, 1.2, 1.2, 1.4, 3

Koszalka, I., J. H. LaCasce, and K. A. Orvik (2009), Relative dispersion in the Nordic Seas, *Journal of Marine Research*, *67*(4), 411–433, doi:10.1357/002224009790741102. 2.2.1

Koszalka, I., J. H. LaCasce, M. Andersson, K. A. Orvik, and C. Mauritzen (2011), Surface circulation in the Nordic Seas from clustered drifters, *Deep-Sea Research Part I: Oceanographic Research Papers*, *58*(4), 468–485, doi:10.1016/j.dsr.2011.01.007. 1, 3

Koszalka, I., J. H. LaCasce, and C. Mauritzen (2013), In pursuit of anomalies-Analyzing the poleward transport of Atlantic Water with surface drifters, *Deep-Sea Research Part II: Topical Studies in Oceanography*, *85*, 96–108, doi:10.1016/j.dsr2.2012.07.035. 1, 1.4, 3

Kvile, K. Ø., G. Romagnoni, K.-F. Dagestad, Ø. Langangen, and T. Kristiansen (2018), Sensitivity of modelled North Sea cod larvae transport to vertical behaviour, ocean model resolution and interannual variation in ocean dynamics, *ICES Journal of Marine Science*, *75*(7), 2413–2424, doi:10.1093/icesjms/fsy039. 2.2.2

Lilly, J. M., and S. C. Olhede (2009), Wavelet ridge estimation of jointly modulated multivariate oscillations, in *2009 Conference Record of the Forty-Third Asilomar Conference on Signals, Systems and Computers*, pp. 452–456, IEEE, doi:10.1109/ACSSC.2009.5469858. 3

Lilly, J. M., and S. C. Olhede (2012), Generalized morse wavelets as a superfamily of analytic wavelets, *IEEE Transactions on Signal Processing*, *60*(11), 6036–6041. 3

Lilly, J. M., R. K. Scott, and S. C. Olhede (2011), Extracting waves and vortices from Lagrangian trajectories, *Geophysical Research Letters*, *38*(23), 1–8, doi:10.1029/2011GL049727. 3

Lumpkin, R., and M. Pazos (2007), Measuring surface currents with Surface Velocity Program drifters: the instrument, its data, and some recent results, *Lagrangian Analysis and Prediction of Coastal and Ocean Dynamics*, pp. 39–67, doi:10.1017/CBO9780511535901.003. 2.2.1

Lumpkin, R., S. A. Grodsky, L. Centurioni, M.-H. Rio, J. A. Carton, and D. Lee (2013), Removing Spurious Low-Frequency Variability in Drifter Velocities, *Journal of Atmospheric and Oceanic Technology*, *30*(2), 353–360, doi:10.1175/JTECH-D-12-00139.1. 2.2.1

MacLachlan, C., A. Arribas, K. A. Peterson, A. Maidens, D. Fereday, A. A. Scaife, M. Gordon, M. Vellinga, A. Williams, R. E. Comer, J. Camp, P. Xavier, and G. Madec (2015), Global Seasonal forecast system version 5 (GloSea5): a high-resolution seasonal forecast system, *Quarterly Journal of the Royal Meteorological Society*, *141*(689), 1072–1084. 2.2.2

Mauritzen, C. (1996), Production of dense overflow waters feeding the North Atlantic across the Greenland-Scotland Ridge. Part 1: Evidence for a revised circulation scheme, *Deep Sea Research Part 1: Oceanographic Research Papers*, *43*(6), 769–806, doi:https://doi.org/10.1016/0967-0637(96)00037-4. 1, 1.3, 3

Nilsen, J. E. Ø., and E. Falck (2006), Progress in Oceanography Variations of mixed layer properties in the Norwegian Sea for the period 1948 1999, *Progress in Oceanography*, *70*, 58–90, doi:10.1016/j.pocean.2006.03.014. 1.3

Nøst, O. A., and P. Isachsen (2003), The large-scale time-mean ocean circulation in the Nordic Seas and Arctic Ocean estimated from simplified dynamics, *Journal of Marine Research*, *61*(2), 175–210, doi:10.1357/002224003322005069. 1

Onarheim, I. H., T. Eldevik, L. H. Smedsrud, and J. C. Stroeve (2018), Seasonal and Regional Manifestation of Arctic Sea Ice Loss, *Journal of Climate*, *31*(12), 4917–4932, doi:10.1175/JCLI-D-17-0427.1. 4.2

Orvik, K. A., and P. Niiler (2002), Major pathways of Atlantic water in the northern North Atlantic and Nordic Seas toward Arctic, *Geophysical Research Letters*, *29*(19), 2–1, doi:10.1029/2002GL015002. 1, 1.1, 4.3

Orvik, K. A., Øystein Skagseth, and M. Mork (2001), Atlantic inflow to the Nordic Seas: current structure and volume fluxes from moored current meters, VM-ADCP and SeaSoar-CTD observations, 19951999, *Deep Sea Research Part I: Oceanographic Research Papers*, *48*(4), 937 – 957, doi:https://doi.org/10.1016/S0967-0637(00)00038-8. 1.1, 3, 4.3

Orvik, K. A., and Øystein Skagseth (2003), Monitoring the Norwegian Atlantic Slope Current using a single moored current meter, *Continental Shelf Research*, *23*(2), 159 – 176, doi:https://doi.org/10.1016/S0278-4343(02)00172-3. 3

Poulain, P.-M., a. Warn-Varnas, and P. P. Niiler (1996), Near-surface circulation of the Nordic seas as measured by Lagrangian drifters, *Journal of Geophysical Research*, *101*, 18,237, doi:10.1029/96JC00506. 1.1, 1.4

Prater, M. D. (2002), Eddies in the Labrador Sea as Observed by Profiling RAFOS Floats and Remote Sensing, *Journal of Physical Oceanography*, *32*(2), 411–427, doi:10.1175/1520-0485(2002)032<0411:EITLSA>2.0.CO;2. 4.3

Raj, R., J. Johannesen, T. Eldevik, J. Nilsen, and I. Halo (2016), Quantifying mesoscale eddies in the Lofoten Basin, *Journal of Geophysical Research: Oceans*, pp. 4503–4521, doi:10.1002/2016JC011637. 1, 1.1, 1.2, 1.2, 1.4, 3

Raj, R. P., L. Chafik, J. E. Ø. Nilsen, T. Eldevik, and I. Halo (2015), The Lofoten Vortex of the Nordic Seas, *Deep-Sea Research Part I: Oceanographic Research Papers*, *96*, 1–14, doi:10.1016/j.dsr.2014.10.011. 1.1, 1.2, 1.2, 3

Rhines, P., S. Häkkinen, and S. A. Josey (2008), *Is Oceanic Heat Transport Significant in the Climate System?*, pp. 87–109, Springer Netherlands, Dordrecht, doi:10.1007/978-1-4020-6774-7_5. 1, 4.2

Richards, C. G., and F. Straneo (2015), Observations of water mass transformation and eddies in the lofoten basin of the nordic seas, *Journal of Physical Oceanography*, *45*(6), 1735–1756, doi:10.1175/JPO-D-14-0238.1. 1, 1.3, 4.2

Rossby, T., M. D. Prater, and H. Søiland (2009a), Pathways of inflow and dispersion of warm waters in the Nordic seas, *Journal of Geophysical Research: Oceans*, *114*(4), 1–17, doi:10.1029/2008JC005073. 1.3, 1.4

Rossby, T., V. Ozhigin, V. Ivshin, and S. Bacon (2009b), An isopycnal view of the Nordic Seas hydrography with focus on properties of the Lofoten Basin, *Deep-Sea Research Part I: Oceanographic Research Papers*, *56*(11), 1955–1971, doi:10.1016/j.dsr.2009.07.005. 1.3

Rühs, S., V. Zhurbas, I. Koszalka, J. Durgadoo, and A. Biastoch (2018), Eddy diffusivity estimates from Lagrangian trajectories simulated with ocean models and surface drifter data - a case study for the greater Agulhas system, *Journal of Physical Oceanography*, (48), 175–196, doi:https://doi.org/10.1175/JPO-D-17-0048.1. 2.2.2

Seager, R., D. S. Battisti, J. Yin, N. Gordon, N. Naik, A. C. Clement, and M. A. Cane (2002), Is the gulf stream responsible for europe's mild winters?, *Quarterly Journal of the Royal Meteorological Society*, *128*(586), 2563–2586, doi:10.1256/qj.01.128. 1, 4.2

Segtnan, O. H., T. Furevik, and A. D. Jenkins (2011), Heat and freshwater budgets of the Nordic seas computed from atmospheric reanalysis and ocean observations, *Journal of Geophysical Research: Oceans*, *116*(11), 1–17, doi:10.1029/2011JC006939. 1

Serreze, M. C., M. M. Holland, and J. Stroeve (2007), Perspectives on the Arctic's Shrinking Sea-Ice Cover, *Science*, *315*(5818), 1533–1536, doi:10.1126/science.1139426. 4.2

Shchepetkin, A. F., and J. C. McWilliams (2005), The regional oceanic modeling system (ROMS): A split-explicit, free-surface, topography-following-coordinate oceanic model, *Ocean Modelling*, *9*(4), 347–404, doi:10.1016/j.ocemod.2004.08.002. 2.2.2

Shchepetkin, A. F., and J. C. McWilliams (2009), Correction and commentary for "Ocean forecasting in terrain-following coordinates: Formulation and skill assessment of the regional ocean modeling system" by Haidvogel et al., J. Comp. Phys. 227, pp. 3595-3624, *Journal of Computational Physics*, *228*(24), 8985–9000, doi:10.1016/j.jcp.2009.09.002. 2.2.2

Søiland, H., and T. Rossby (2013), On the structure of the Lofoten Basin Eddy, *Journal of Geophysical Research: Oceans*, *118*, 4201–4212, doi:10.1002/jgrc.20301. 1.2

Spall, M. A. (2010), Dynamics of Downwelling in an Eddy-Resolving Convective Basin, *Journal of Physical Oceanography*, *40*(10), 2341–2347, doi:10.1175/2010JPO4465.1. 3

Strand, K. O., S. Sundby, J. Albretsen, and F. B. Vikebø (2017), The Northeast Greenland Shelf as a Potential Habitat for the Northeast Arctic Cod, *Frontiers in Marine Science*, *4*(September), 1–14, doi:10.3389/fmars.2017.00304. 4.2

Sundby, S. (2000), Recruitment of atlantic cod stocks in relation to temperature and advection of copepod populations, *Sarsia*, *85*(4), 277–298, doi:10.1080/00364827.2000.10414580. 1

Trodahl, M., and P. E. Isachsen (2018), Topographic Influence on Baroclinic Instability and the Mesoscale Eddy Field in the Northern North Atlantic Ocean and the Nordic Seas, *Journal of Physical Oceanography*, *48*(11), 2593–2607, doi:10.1175/JPO-D-17-0220.1. 2.2.2, 4.3

Umlauf, L., and H. Burchard (2003), A generic length-scale equation for geophysical turbulence models, *Journal of Marine Research*, *61*(2), 235–265. 2.2.2

van Sebille, E., S. M. Griffies, R. Abernathey, T. P. Adams, P. Berloff, A. Biastoch, B. Blanke, E. P. Chassignet, Y. Cheng, C. J. Cotter, E. Deleersnijder, K. Döös, H. F. Drake, S. Drijfhout, S. F. Gary, A. W. Heemink, J. Kjellsson, I. M. Koszalka, M. Lange, C. Lique, G. A. MacGilchrist, R. Marsh, C. G. Mayorga Adame, R. McAdam, F. Nencioli, C. B. Paris, M. D. Piggott, J. A. Polton, S. Rühs, S. H. Shah, M. D. Thomas, J. Wang, P. J. Wolfram, L. Zanna, and J. D. Zika (2018), Lagrangian ocean analysis: Fundamentals and practices, *Ocean Modelling*, *121*(October 2017), 49–71, doi:10.1016/j.ocemod.2017.11.008. 2.2.2

Voet, G., D. Quadfasel, K. A. Mork, and H. Søiland (2010), The mid-depth circulation of the Nordic Seas derived from profiling float observations, *Tellus A*, *62*(4), 516–529, doi:10.1111/j.1600-0870.2010.00444.x. 1

Volkov, D. L., T. V. Belonenko, and V. R. Foux (2013), Puzzling over the dynamics of the Lofoten Basin - a sub-Arctic hot spot of ocean variability, *Geophysical Research Letters*, *40*(December 2012), 738–743, doi:10.1002/grl.50126. 1.1, 1.3, 1.4

Volkov, D. L., A. A. Kubryakov, and R. Lumpkin (2015), Formation and variability of the Lofoten basin vortex in a high-resolution ocean model, *Deep-Sea Research Part I: Oceanographic Research Papers*, *105*, 142–157, doi:10.1016/j.dsr.2015.09.001. 1.1, 1.2, 1.4, 3, 4.3

Wagner, P., S. Rühs, F. U. Schwarzkopf, I. Koszalka, and A. Biastoch (2019), Can Lagrangian tracking simulate tracer spreading in a high-resolution Ocean General Circulation Model?, *Journal of Physical Oceanography*, *49*(5), 1141–1157, doi:https://journals.ametsoc.org/doi/pdf/10.1175/JPO-D-18-0152.1. 2.2.2

Warner, J. C., C. R. Sherwood, H. G. Arango, and R. P. Signell (2005), Performance of four turbulence closure models implemented using a generic length scale method, *Ocean Modelling*, *8*(12), 81–113. 2.2.2

Werner, F. E., J. A. Quinlan, B. O. Blanton, and R. A. Luettich (1997), The role of hydrodynamics in explaining variability in fish populations, *Journal of Sea Research*, *37*(3), 195 – 212, doi:https://doi.org/10.1016/S1385-1101(97)00024-5. 4.2

Ypma, S., S. Georgio, J. Dugstad, J. Pietrzak, and C. Katsman (2020), Pathways and water mass transformation along and across the Mohn-Knipovich Ridge in the Nordic Seas, *Journal of Geophysical Research: Oceans*, *Accepted August 2020*. 4.3

Yu, L. S., A. Bosse, I. Fer, K. A. Orvik, E. M. Bruvik, I. Hessevik, and K. Kvalsund (2017), The Lofoten Basin eddy: Three years of evolution as observed by Seagliders, *Journal of Geophysical Research: Oceans*, *122*(8), 6814–6834, doi:10.1002/2017JC012982. 4.3

Årthun, M., T. Eldevik, and L. H. Smedsrud (2019), The Role of Atlantic Heat Transport in Future Arctic Winter Sea Ice Loss, *Journal of Climate*, *32*(11), 3327–3341, doi:10.1175/JCLI-D-18-0750.1. 4.2

Graphic design: Communication Division, UiB / Print: Skipnes Kommunikasjon AS

uib.no

ISBN: 9788230851340 (print)
9788230865859 (PDF)